# A Generalized Method for Fissile Material Characterization Using Short-Lived Fission Product Gamma Spectroscopy

A Dissertation Presented for the

Doctor of Philosophy

Degree

The University of Tennessee, Knoxville

Justin Richard Knowles

August 2016

© by Justin Richard Knowles, 2016
All Rights Reserved.

*This work is dedicated to Marsha, who's love, patience, and kindness was critical to helping me through some of the toughest years of my life.*

# Acknowledgments

This work would not have been possible without the care and support of the people around me. I would like to thank Dr. Steven Skutnik, who was not only my advisor but also a good friend. He helped me develop professionally and ensured that I always put my best work forward. Additionally, I would like to thank David Glasgow, who served as an exceptional mentor at Oak Ridge National Laboratory. He provided me with the tools and valuable advising necessary to conduct effective research in a nuclear laboratory. I also greatly appreciate all of the engineering, operations, and radiological control workers at the High Flux Isotope Reactor for ensuring that my research was both efficient and safe.

The Bredesen Center and the University of Tennessee made the dream of achieving a PhD a reality by providing me with the means to do so. Dr. Lee Riedinger was was the one who got everything started by selecting me as a student in his program.

I would also like to thank my loving girlfriend Marsha for always being there for me in these challenging years. Lastly, I would be nothing without my family's hard work in raising me with the moral values and work ethic that have taken me this far.

*In science, it is not speed that is the most important. It is the dedication, the commitment, the interest, and the will to know something and to understand it — these are the things that come first.*

*- Eugene P. Wigner*

# Abstract

Characterizing the fissile content of nuclear materials is of particular interest to the safeguards and nuclear forensics communities. Short-lived fission product gamma spectroscopy offers a significant reduction in analysis time and detection limits when compared to traditional non-destructive assay measurements. Through this work, a fully generalizable method that can be applied to variations in fissile compositions and neutron spectra was developed for the modeling and measurement of short-lived fission product gamma-rays. This method uses a 238-group neutron flux that was characterized for two pneumatic tube positions in the High Flux Isotope Reactor using flux monitor irradiations. This flux spectrum was then used in determining theoretical fission product photopeak emission rates per unit fissile mass during measurement. From these theoretical values, a mathematical method for characterizing the fissile material within a sample was established and demonstrated in several cases. The Oak Ridge National Laboratory's High Flux Isotope Reactor and Neutron Activation Analysis Laboratory provided optimal conditions to conduct high-flux irradiations with short decay periods. Experiments with samples containing nanogram quantities of $^{235}$U, $^{233}$U, and $^{239}$Pu were accurately characterized through measurement of short-lived fission product photopeaks. These measured photopeaks were combined with the simulated theoretical production rates to construct an overdetermined system of linear equations. Once this overdetermined system was solved, it showed high accuracy in quantifying fissile content. These experiments resulted in errors less of

than 10% for quantification of fissile material in single element samples, two element mixed samples, and varying enrichments of uranium on IAEA swipes.

# Table of Contents

**1 Motivation** **1**

**2 Background** **5**

2.1 Underlying Physics . . . . . 5

2.2 Short-Lived Fission Products . . . . . 7

2.3 Gamma-Ray Spectroscopy of SLFPs . . . . . 8

2.4 Prior SLFP Work . . . . . 11

2.5 The High Flux Isotope Reactor and HFIR-NAA Laboratory . . . . . 15

**3 Theory** **19**

3.1 Fission Product Modeling and Simulation . . . . . 19

3.2 Neutron Flux Characterization . . . . . 22

3.3 The Generalized System of Equations . . . . . 26

3.4 Solving Overdetermined Systems and Error Propagation . . . . . 27

**4 Experimental** **30**

4.1 HPGe Detector System and Calibration . . . . . 30

4.2 Loss Free Counting . . . . . 33

4.3 Irradiation Setup . . . . . 34

4.4 PT-1 Benchmarking Fission Product Photopeak Simulations to Prior Work . . . . . 35

4.5 PT-2 Flux Characterization . . . . . 37

4.6 $^{239}$Pu and $^{235}$U Indicators Scoping Study . . . . . 42
4.7 Samples Evaluated . . . . . 44
4.8 Irradiation and Measurement Characteristics . . . . . 45

**5 Results** **48**
5.1 Photopeak Modeling Results . . . . . 48
5.2 Fission Product Recoveries . . . . . 51
5.3 System of Equations for Single Element Samples . . . . . 56
5.4 Binary Mixtures . . . . . 59
5.5 Matrices of Safeguards Interest . . . . . 62
5.6 Detection Limits . . . . . 65

**6 Conclusions** **67**
6.1 Research Outcomes . . . . . 67
6.2 Lessons Learned . . . . . 68
6.3 Opportunities for Future Work . . . . . 70

**Bibliography** **72**

**Appendix** **78**

**A SCALE 238-Group Structure** **79**

**B Flux Characterizations** **86**

**Vita** **93**

# List of Tables


1.1 Typical Fissile Isotope Analysis Methods . . . . . 3

2.1 Prior short-lived fission product gamma spectroscopy work . . . . . 12
2.2 Beddingfield et al. $^{235}$U fission product photopeak results [1] . . . . . 13
2.3 Andrews et al. $^{235}$U fission product photopeak results [2] . . . . . 15

3.1 PT-2 Au and Mn Flux Monitoring . . . . . 24

4.1 Sources Used in HPGe Detector Calibration . . . . . 32
4.2 SCALE simulation and HFIR-NAA benchmark to Beddingfield et al. [1] 37
4.3 SCALE simulation and HFIR-NAA benchmark to Andrews et al. [2] 38
4.4 Flux Characterization Measurement Monitors . . . . . 40
4.5 PT-2 Corrected/Uncorrected Spectra Comparison . . . . . 41
4.6 Listed info on FP Indicators for $^{239}$Pu and $^{235}$U . . . . . 45
4.7 Listed Sample Info for Solutions Containing $^{239}$Pu, $^{235}$U, and $^{233}$U . . 46
4.8 Irradiation and Measurement Characteristics . . . . . 46
4.9 Fission Product Isotopes and Photopeaks Evaluated . . . . . 47

5.1 Photopeak Modeling Results for PT-1 Single Elements Case . . . . . 49
5.2 Photopeak Modeling Results for PT-2 Single Elements Case . . . . . 50
5.3 Table of Fission Product Yield Uncertainties from ENDF/B-VII.1 for Energy=0.0253 eV [3] . . . . . 55
5.4 Sample Details for Binary Mixtures . . . . . 59
5.5 IAEA Swipe Activation Products . . . . . 63

5.6 IAEA Swipe Sample Measurement Details . . . . . 65

# List of Figures


2.1 $^{235}$U and $^{239}$Pu Cumulative Fission Yields [3] . . . . . 6
2.2 $^{60}$Co Decay Scheme [4] . . . . . 7
2.3 Temporal Distribution of $^{235}$U Fission Products [1] . . . . . 9
2.4 Comparison of various dead-time corrections with increasing amounts of activated Au [5] . . . . . 10
2.5 Beddingfield et al. Weighting Factor Results [1] . . . . . 14
2.6 HFIR Core Diagram [6] . . . . . 16
2.7 HFIR PT-1 and PT-2 Flux Spectra (data adopted from[7]) . . . . . 17
2.8 HFIR-NAA PT-1 Facility (PT-2 has nearly identical layout) . . . . . 18

3.1 Flow diagram for SCALE simulations . . . . . 21
3.2 $^{55}$Mn and $^{198}$Au Capture Cross Sections [3] . . . . . 23
3.3 Fission cross sections for $^{235}$U, $^{233}$U, and $^{239}$Pu along with neutron absorption cross section for $^{238}$U for low energy resonances [3] . . . . 25
3.4 Flow diagram for STAYSL-PNNL modeling . . . . . 26

4.1 HFIR-NAA Facility Graded Shield with HPGe Detector . . . . . 31
4.2 HPGe Calibrated Efficiency Plots for 100mm and 300mm measurement positions . . . . . 32
4.3 DLFC and PHA Comparison . . . . . 34
4.4 High-Density Polyethelene Rabbit with IAEA J-Swipe . . . . . 35
4.5 PT-1 Facility with Shielded Cubicle . . . . . 36

4.6 $^{113}$Cd Neutron Absorption Cross Section [3] . . . . . 39
4.7 STAYSL-PNNL Corrected PT-2 Spectrum compared to STAYSL-PNNL Input Spectrum . . . . . 41
4.8 STAYSL-PNNL Corrected PT-2 Spectrum Compared to MCNP Prediction . . . . . 42
4.9 Graph of Fission Product Indicators for $^{239}$Pu and $^{235}$U . . . . . 44

5.1 Fission product photopeak C/E (ORIGEN Calculated divided by Experimentally measured) values and counting uncertainties for 4 separate irradiations in PT-1 and 4 irradiations in PT-2 using corrected spectra . . . . . 52
5.2 SCALE predicted photopeak yields divided by the short-lived fission product photopeak measurements from $^{239}$Pu for 4 PT-1 and 4 PT-2 irradiations . . . . . 53
5.3 SCALE predicted photopeak yields divided by the short-lived fission product photopeak measurements from $^{233}$U for 4 PT-1 and 4 PT-2 irradiations . . . . . 54
5.4 SCALE predicted photopeak yields divided by the short-lived fission product photopeak measurements from $^{235}$U for 4 PT-1 and 4 PT-2 irradiations . . . . . 54
5.5 PT-1, PT-2 corrected, and PT-2 uncorrected calculated over certified values for nanogram quanitites of nuclides from single element irradiations of natural uranium, high-purity $^{233}$U, and plutonium solutions 57
5.6 Box and whisker plots showing the spread of PT-1 and PT-2 corrected C/E values . . . . . 58
5.7 Calculated over certified mass assay results for fissile mixtures irradiated in PT-2 . . . . . 60
5.8 Calculated over certified mass assay results for fissile mixtures irradiated in PT-1 . . . . . 61

5.9 C/E Recoveries for Uranium on IAEA Swipes . . . . . 64
5.10 Detection Limits for $^{235}$U Fission Products . . . . . 66

# Chapter 1

# Motivation

Quantifying the fissile content within trace amounts of nuclear material is of significant importance to safeguards and nuclear forensics communities. Traditionally, measurement methods have relied on destructive analysis (DA) measurements or passive detection of gamma/neutron signatures through nondestructive assay (NDA). These methods are highly accurate and employed globally as both a nuclear forensics capability and a material accountability measurement. However, common DA techniques rely on sample dissolution, a time-consuming process which can be particularly difficult for certain sample matrices, such as melt-glass formed from nuclear fallout. Likewise, trace quantities of nuclear materials prove difficult to measure using passive NDA techniques due to relatively low emission rates and potential interference from activated materials within the sample matrix. Additionally, the timeliness of fissile material assay is of concern for both treaty verification and post-nuclear detonation scenarios. Established DA methods, such as Thermal Ionization Mass Spectrometry (TIMS) and inductively coupled plasma mass spectrometry (ICP-MS) can effectively characterize uranium and plutonium isotopic content, but require complete sample dissolution. This sample preparation requirement challenges the timeliness goals provided by national and international agencies. Cooley et al. report that the International Atomic Energy Agency's

Safeguards Analytical Laboratory (SAL), which utilizes these DA methods, is capable of measuring environmental samples from a typical enrichment facility within approximately three weeks [8]. This timeline is recognized by many as a vulnerability in the international safeguards envelope and significant research has been conducted on reducing it [9].

One of the most important objectives of the International Atomic Agency (IAEA) is deterrence of material diversion through timely detection. This is accomplished by establishing the ability to detect all credible proliferation pathways, often by conducting material assays throughout the fuel cycle. Since the frequency of IAEA inspections at declared facilities is typically driven by timeliness goals, rapid analysis techniques are in some cases paramount. This is due to the fact that the analysis time of a technique must be comparable to the assayed material's conversion period for it to be effective. Assuming that the conversion of HEU metal into material usable in weapons is approximately 1 week, and that there are many facilities worldwide containing significant quantities of uranium requiring safeguards measurements, an assay timeline of less than 1 week is needed to best meet timeliness goals. [9]

Table 1.1 further illustrates the significant gap in fissile material analytical capabilities. This is a very small sampling of these capabilities, but it is used to describe the limitations of typical NDA and DA techniques. Most traditional NDA methods rely on the detection of radiation signatures emitted from the material, increasing the need for background discrimination, which impacts sensitivities at the lowest ranges of detection. For state of the art DA techniques, sample dissolution is necessary to obtain the lowest detection limits and can require a significant timeline increase. The work presented in this document aims at providing a technique that may not necessarily surpass DA detection limits, or NDA analysis time, but fills an important niche in fissile material characterization by providing high accuracy quantifications at nanogram detection limits without sample dissolution.

Within the NDA realm, dissolution of the sample is generally not necessary, and signatures such as gamma-rays or neutrons are received by a detector through either

**Table 1.1:** Typical Fissile Isotope Analysis Methods

| Technique | Detection Limit (g) | Analysis Time | Sample Dissolution | Information Provided |
|---|---|---|---|---|
| AWCC [10] | $10^{0}$ | Minutes | No | Fissile isotopes |
| Passive $(\gamma/n)$ [11] | $10^{-3}$ | Min-Hrs | No | $(\gamma/n)$ isotopes |
| Neutron Shuffler [12] | $10^{-3}$ | Minutes | No | Fissile isotopes |
| XRF/HKED [13] | $10^{-4}$ | Minutes | No | Elemental |
| Emission Spectrometry [14] | $10^{-9}$ | Days | Yes | Elemental |
| Mass Spectrometry [15] | $10^{-15}$ | Days | Yes | Isotopic |

passive or active interrogation means. Active Well Coincidence Counters (AWCC) are often used for the assay of fissile material within a large container through use of a small neutron source. Due to their active interrogation and ability to measure neutron multiplicities, AWCC systems can obtain lower detection limits than most well counters [10]. Passive neutron and gamma methods use radioactive signatures from the fissile isotopes, or their decay precursors, but are limited by background effects with detection limits on the order of milligrams [11]. A neutron shuffler is similar to the AWCC in that it has a large sample holding position with active interrogation, but differs in that it measures the delayed neutrons over several time bins to obtain a fissile material assay. Neutron shufflers can identify fissile isotope signatures and are relatively insensitive to background, but are limited to the strength of the $^{252}$Cf neutron source [12]. The combination of X-Ray Fluorescence (XRF) and K-Edge Densitometry (KED) methods (known as Hybrid K-Edge Densitometry or HKED) touts some of the lowest detection limits in NDA, but is generally only capable of characterizing elemental U or Pu. Additionally, HKED is generally only applicable to optically transparent samples (e.g., solutions, salts, and other less-dense materials, as KED is a transmission-based measurement) [13].

There are a vast number of DA methods that can be used to characterize samples containing fissile material. Emission and mass spectrometry cover several of the most accurate and widely used DA methods. Emission spectrometry often utilizes an Inductively Coupled Plasma (ICP), which is commonly used as a source for mass spectrometry. Due to emission spectrometry's use of atomic emissions from collisional excitation, it is only capable of measuring elemental concentrations at nanogram levels [14]. Mass spectrometry goes even further with accelerating the charged ions through a magnetic field and quantifying their charge and mass for an isotopic determination. This method is often seen as the gold standard in isotopic analysis due to its high-fidelity and detection limits within the femtogram range [15]. The greatest challenge in employing these DA methods is the necessity to conduct a thorough sample dissolution. Unlike NDA methods, the DA analysis routine requires significant time and user interaction.

Developing an analysis technique that has low detection limits, isotopic specificity, and rapid characterization periods is of significant interest. One method that has been proposed to address this need is the use of short-lived fission product gamma spectroscopy measurements. This has been the subject of several publications containing methods that have been developed to identify fissile materials and in some cases quantify their masses [1, 16, 2]. These methods have been developed for a select few irradiation facilities, and have experienced challenges in accurate comparison to predictions from nuclear data. This work presents a generalized approach to characterizing fissile isotope containing materials using Neutron Activation Analysis (NAA) and advanced modeling and simulation techniques.

# Chapter 2

# Background

## 2.1 Underlying Physics

The basis of this method is focused on using differences in fission product yields to characterize the fissile content of samples. Through application of Neutron Activation Analysis (NAA), short-lived fission products can be created and measured for the calculation of fissile content. Figure 2.1 shows the vast array of cumulative fission product yields for $^{235}$U and $^{239}$Pu [3]. Although there are a large number of fission products produced in thermal neutron irradiation, only a fraction of them are detectable by traditional gamma-ray spectroscopy. Most of these fission products are neutron-rich and undergo beta-delayed gamma emissions. This process involves the conversion of a neutron to a proton, emission of an antineutrino, and the creation of an unstable daughter nucleus (Equation 2.1) [4].

$$ {}^{A}_{Z}X^{*} \rightarrow {}^{A}_{Z+1}X' + e^{-} + \bar{\nu_e} \tag{2.1} $$

The unstable nucleus quickly undergoes a gamma-ray emission with energy and rate respective to its unique decay scheme and half-life ($^{60}$Co example shown in Figure 2.2). These gamma-ray emissions can be measured and the emitting nuclide can be identified using standard gamma spectroscopy instrumentation such as a

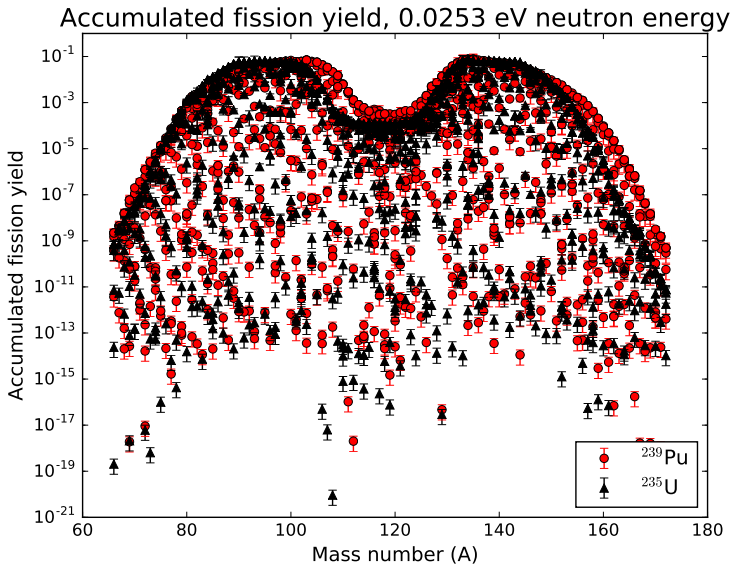



**Figure 2.1:** $^{235}$U and $^{239}$Pu Cumulative Fission Yields [3]

High-Purity Germanium (HPGe) detector and Multi-Channel Analyzer (MCA) [17]. Traditional gamma spectroscopy allows for the radioactive atoms within the sample to be quantified using a photopeak integral divided by decay and efficiency correction factors. Using this measured activity, the number of target atoms can be calculated through application of the activation equation (Equation 2.2). For this version of the activation equation, the activated material can be used to quantify the parent element's concentration using the measured activity (A), reaction cross section ($\sigma$), total neutron flux ($\phi$), decay constant ($\lambda$), and irradiation time ($t_{irr}$), thus providing an analytical method for quantification of trace elements (Equation 2.2).

$$N_{target} = \frac{A}{\sigma\phi(1 - e^{-\lambda t_{irr}})} \tag{2.2}$$

It is important to note that the cross-section value in Equation 2.2 is most accurately represented by a 1-group flux-weighted cross-section. This allows for the reaction rate to be representative of the entire energy spectrum of the interrogating neutron source. Cross-section processing codes are often used in the calculation of

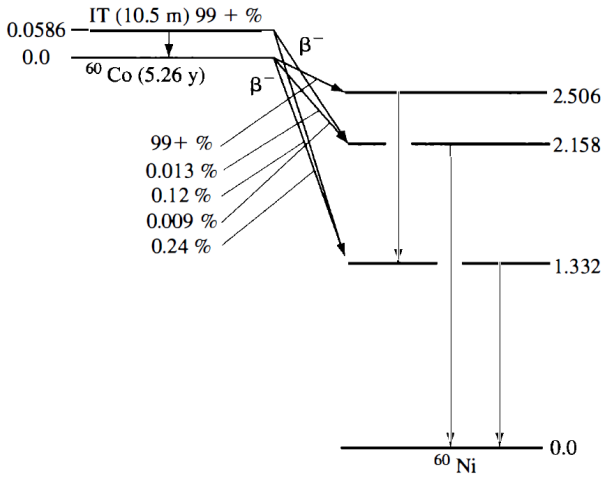



**Figure 2.2:** $^{60}$Co Decay Scheme [4]

this value, but the fundamental principle of a cross-section collapse from a multi-group flux can be represented with Equation 2.3. This is a guiding principle in the development of this characterization method, and will be revisited in the modeling and simulation section [18].

$$\langle\sigma\rangle_g = \frac{\int_{E_{g+1}}^{E_g} \sigma(E)\phi(E)dE}{\int_{E_{g+1}}^{E_g} \sigma(E)dE} \tag{2.3}$$

## 2.2 Short-Lived Fission Products

The physical basis in using Short-Lived Fission Product (SLFP) measurements for fissile mass characterization has been established over decades of spent fuel assay experience. Gamma spectroscopy is routinely conducted on spent nuclear fuel and other forms of high-level waste for the quantification of burnup or cooling time. This is accomplished through passively measuring the gamma-ray emissions of specific fission product indicators and comparing to correlations in modeled or experimental data (such as $^{154}$Eu, $^{137}$Cs, or $^{134}$Cs). In spent nuclear fuel the most commonly measured gamma emissions originate from medium or long-lived ($\tau_{1/2} > 1$ yr) fission products

residing within the fuel matrix. Although these passive measurements can reveal the burnup experienced within a fuel matrix, fissile composition cannot be determined without considerable prior knowledge [19, 20].

To address the need for fissile composition measurements, methods have been developed to employ active interrogation with integrated gamma-ray spectroscopy [21]. Active interrogation enables for a known neutron spectrum to be used on samples containing fissile material, producing predictable fission product yields. With this additional information, active interrogation methods are capable of obtaining ratios of fissile materials within the matrix and are often more rapid than their passive counterparts. Therefore, for a method focused on safeguards, forensics, or Material Control & Accountability (MC&A), active interrogation methods are more applicable. Beddingfield et el. [1] showed through evaluation of nuclear data that the majority of fission products have half-lives less of under an hour and therefore need more rapid measurements than traditional passive spent fuel gamma spectroscopy (Figure 2.3).

The variety and number of SLFPs within a sample that has been interrogated by neutrons opens the door for many possibilities for measurements of fissile mass and isotopic composition. Additionally, the high signal-to-noise ratio makes this active interrogation technique capable of measuring samples that are radioactive or contain materials within its matrix that activate. This brings better peak statistics for more accurate determinations and lower detection limits, opening the door for use in technical nuclear forensics applications. Lastly, SLFP measurements allow measurements to be made in rapid succession in time intervals that are shorter than both passive Non-Destructive Assay (NDA) and destructive chemical assay.

## 2.3 Gamma-Ray Spectroscopy of SLFPs

Although there are advantages to short-lived fission product gamma spectroscopy, conducting accurate and reliable measurements is a challenge. The use of digital MCAs, high-resolution HPGe detectors, and nuclear modeling and simulation

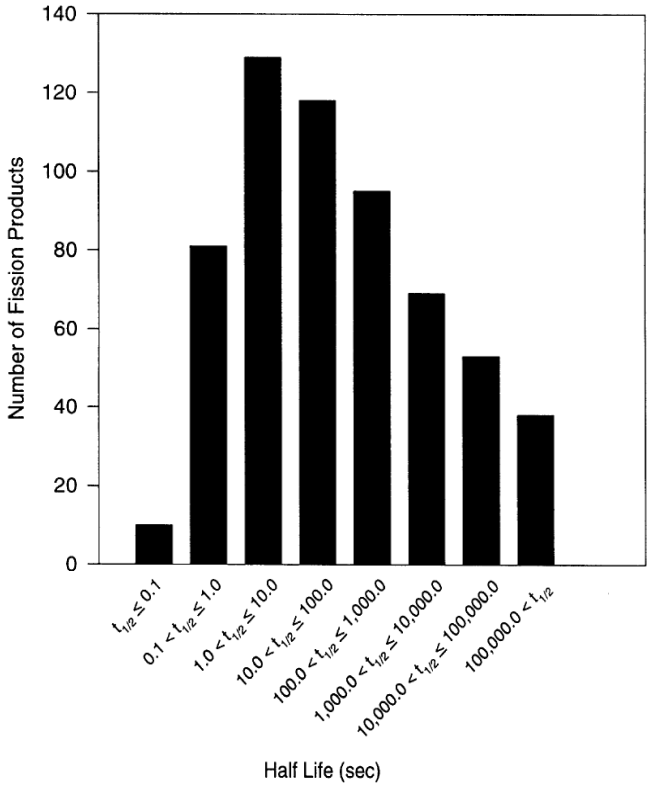



**Figure 2.3:** Temporal Distribution of $^{235}$U Fission Products [1]

provides significant advantage over prior work. Combining these modern tools with a new methodology of unfolding gamma-ray spectra enable the methods described herein to be high-fidelity and generalizable to any reactor facility.

One common challenge in gamma spectroscopy is accounting for large activities through dead-time corrections. Dead-time ($\tau$) represents the fraction of gamma-ray counts lost due to the short periods of time required for signal processing and charge collection . This effect is due to the combined delays from charge collection and detector electronic processing and is often managed through a traditional nonparalyzable dead-time correction (Equation 2.4) where $n$ is the true interaction rate and $m$ is the recorded count rate [17]. As a rule-of-thumb, this correction is often adequate for isotopes containing half-lives greater than the measurement period and

dead times of less than 30%.

$$n = \frac{m}{1 - m\tau} \tag{2.4}$$

The issue of dead-time is significantly more complex for quickly decaying isotopes and large dead-times. Several publications have shown that the activity of a rapidly decaying isotope is poorly calculated using a traditional nonparalyzable dead-time correction [17, 5, 22]. Figure 2.4 shows an experiment conducted by Wiernik to determine the accuracy of various dead-time corrections. In this set of experiments, varying masses of Au were irradiated in a reactor and measured at a HPGe detector. The larger Au masses induced larger dead-times and induced increasing errors in the calculations of real counts in the short-lived $^{197m}$Au.

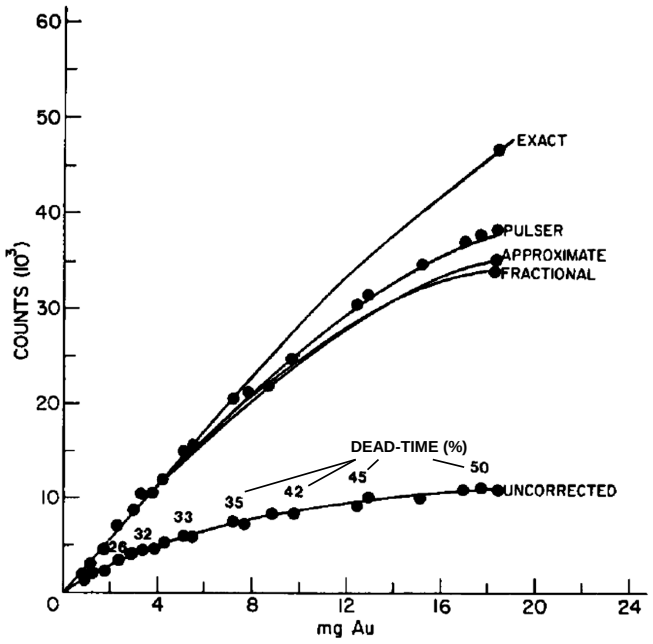



**Figure 2.4:** Comparison of various dead-time corrections with increasing amounts of activated Au [5]

Since there are many rapidly decaying isotopes in a SLFP gamma spectrum, the dead-time is expected to change considerably during the acquisition period. A correction factor that treats spectra in a homogenized fashion is not appropriate, and

many of the correction methods tested in Wiernik's work are not adequate. To address this issue, Loss Free Counting (LFC) can be applied to the detector acquisition. The LFC method adds pulses for period of time when the system is not acquiring, which provides near real time dead-time corrections. Blaauw et al. [23] studied the effects of LFC on peak width, count rate, and peak position for count rates up to $1 \cdot 10^5$ counts per second using a digital MCA. It was shown through this work that LFC can accurately measure activity within 2% error at 80% dead time. Further validation of these methods will be discussed in the experimental section.

## 2.4 Prior SLFP Work

Within presently established methods of non-destructive gamma-ray analysis, obtaining fissile isotopic information is a significant challenge. The generally accepted methods for quantification of plutonium and uranium isotopic measurements involve comparative measurements of their low energy gamma-ray emissions. These methods have established detection limits in the range of hundreds of milligrams to kilograms of fissile isotopic mass for an analysis time between 15 minutes and 2 hours [11, 24, 25]. Due to the low emission rates and low energies of fissile isotope signatures, detection limits suffer from any amount of background and matrix activity. Additionally, significant geometry corrections must be made for low-energy gamma-ray attenuation in the large sample sizes analyzed. To address these concerns, SLFPs have been studied by prior work to identify signatures that can provide a high-fidelity and rapid characterization.

The method being developed at the High Flux Isotope Reactor (HFIR) builds upon prior Non-Destructive Assay (NDA) active interrogation research and proposes a more generalized method of fissile mass quantification using only short-lived fission product gamma spectroscopy. Previous work conducted by Marrs et al. [16], Beddingfield et al. [1], and Andrews et al. [2] significantly advanced the state of the art by

incorporating increasingly accurate methods of short-lived fission product gamma-ray measurements and modeling. A simple comparison of the experimental setup in these publications can be seen in Table 2.1.

**Table 2.1:** Prior short-lived fission product gamma spectroscopy work

| Author | Fissile Mass | Analysis Time | Neutron Spectrum | Isotopes |
|---|---|---|---|---|
| Marrs et al. | 0.19 - 0.57 g | 10 - 840 min | 14 MeV+Thermal | 1 |
| Beddingfield et al. | 40 g | 26 min | Moderated $^{252}$Cf | 1 |
| Andrews et al. | 1.3 $\mu$g - 4.3 $\mu$g | <5 min | Thermal | 1 |
| Knowles et al. | 12 ng - 160 ng | <10 min | Thermal | 2+ |

Marrs et al. [16] developed a study on $^{239}$Pu and $^{235}$U fission product gamma-ray lines of interest for fissile isotope identification by comparing published Evaluated Nuclear Data File (ENDF) fission cross sections and yield compilations to measurements from monoenergetic neutron beam interrogation. The neutron beam consisted of a 88-in. cyclotron at Lawrence Berkeley National Laboratory that collided 16-MeV deuteron beam at 1.0-3.3 $\mu$A with a beryllium target. The neutrons were thermalized through steel and polyethelene to produce deuteron neutron beams centered at 14-MeV and thermal energies. Marrs et al. used HPGe detectors to identify 18 fission product ratios that could be used to distinguish $^{239}$Pu from $^{235}$U fission and compared them to fission product yield compilations prepared by Los Alamos National Laboratory [26]. This study helped guide preliminary investigations at HFIR and gave promise to investigating fission product isotopes that are indicators of different fissile isotopes. The majority of gamma lines explored in the study by Marrs et al. exceeded the time regime of interest for the current research at HFIR, and was therefore not used as a benchmark for the methods discussed later.

Research conducted by Beddingfield et al. prompted evolutionary changes to active interrogation by developing a method for the identification of fissile species

from short-lived fission product gamma ray emissions. In Beddingfield's methodology, weighting factors are developed to distinguish between $^{239}$Pu and $^{235}$U (Equations 2.5 and 2.6). In these calculations, theoretical photopeak ratios were determined using ENDF/B-IV fission product yields and decay data for $^{235}$U and $^{239}$Pu ($r_U$ and $r_{Pu}$). These ratios were incorporated with measured data from interrogation of a sample ($r_{obs}$). A calculated $^{235}$U weighting factor ($W_U$) that is near 100 will show a match for $^{235}$U, while a $^{239}$Pu weighting factor ($W_{Pu}$) near 100 indicates a match for $^{239}$Pu.

$$W_U = \left(1 - \left|\frac{r_{obs} - r_U}{r_{Pu} - r_U}\right|\right) 100\% \tag{2.5}$$

$$W_{Pu} = \left(1 - \left|\frac{r_{obs} - r_{Pu}}{r_{Pu} - r_U}\right|\right) 100\% \tag{2.6}$$

In their experiments, Beddingfield et al. irradiated 40 g High Enriched Uranium (HEU) samples for 100 s using a moderated $^{252}$Cf interrogation source. Samples were decayed for 1100 s, and subsequent HPGe gamma spectroscopy measurements were conducted over an interval of 350 s. Photopeak ratios were then calculated with the numerator and denominators given in Table 2.2.

**Table 2.2:** Beddingfield et al. $^{235}$U fission product photopeak results [1]

| Numerator Isotope | Energy (keV) | Denominator Isotope | Energy (keV) | $r_{Pu}$ | $r_U$ | $r_{obs}$ | Uncert. | Bias |
|---|---|---|---|---|---|---|---|---|
| $^{89}$Rb | 1031.9 | $^{130}$Sb/$^{130*}$Sb | 839.4 | 0.95 | 2.65 | 2.05 | 2.4% | -22.6% |
| $^{89}$Rb | 1031.9 | $^{142}$Ba | 1000.9 | 4.38 | 9.07 | 10.88 | 6.0% | -20.0% |
| $^{94}$Y | 918.8 | $^{131}$Sb | 933.1 | 7.11 | 10.84 | 14.01 | 18.4% | 29.2% |
| $^{90}$Rb/$^{90*}$Rb | 831.7 | $^{130}$Sb/$^{130*}$Sb | 839.4 | 0.15 | 0.38 | 0.78 | 3.8% | 105.3% |
| $^{90}$Rb/$^{90*}$Rb | 831.7 | $^{133m}$Te | 912.7 | 1.32 | 3.04 | 3.85 | 6.8% | 26.6% |

Despite the significant biases in the observed to theoretical $^{235}$U fission product photopeak ratios ($r_U$ to $r_{obs}$) , Beddingfield et al. still conducted successful

identification of the fissile species through application of the weighting factors (Equations 2.5 and 2.6). Figure 2.5 shows the results for all of the fission product ratios considered by Beddingfield et al. in their identification of $^{235}$U.

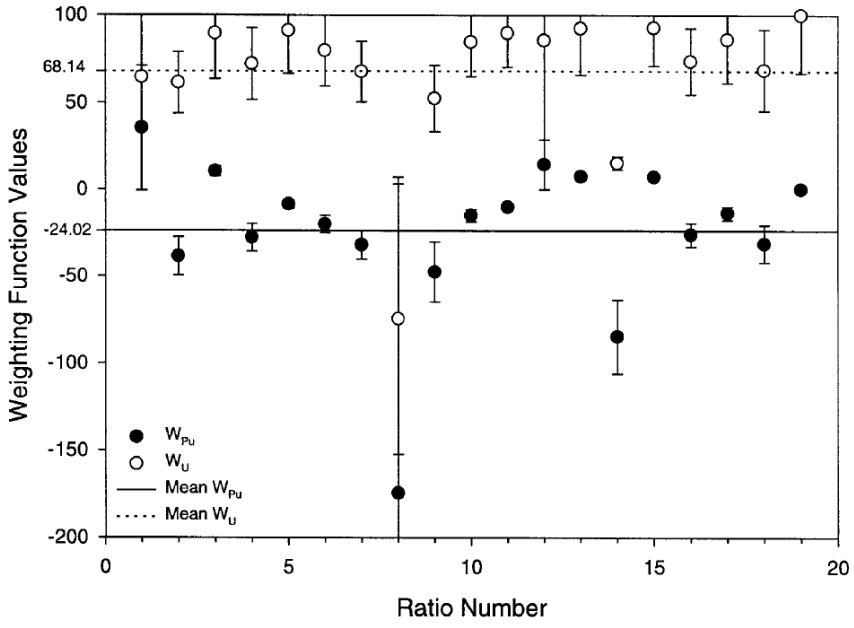



**Figure 2.5:** Beddingfield et al. Weighting Factor Results [1]

Although this method could effectively identify $^{235}$U as the parent fissioning species, the large biases from theoretical to observed ratios would make it impossible to conduct a fissile mass quantification. These biases may be due to not accounting for a number of factors, including calculation of appropriate flux-weighted cross sections, corrections for detector intrinsic efficiency related to photopeak energies, and activity changes during measurement resulting from fission product decay. Some of the most challenging isotope ratios were selected from the work of Beddingfield et al. for benchmarking with the more generalized method proposed in this work.

Andrews et al. advanced the accuracy of fission product photopeak estimations significantly by applying state of the art modeling and simulation techniques to the prediction of photopeak production rates. Irradiations of microgram quantities of

fissile material were conducted at the SLOWPOKE 2 reactor at the Royal Military College of Canada with a thermal neutron flux of $2.6 \cdot 10^{11} \frac{\text{n}}{\text{cm}^2 \cdot \text{s}}$. After a 60 s irradiation and 15 s of decay, gamma spectroscopy was conducted for 180 s and compared to simulations conducted using MCNP v6.1.1 (public beta) [2]. (MCNP 6.1, used in Andrews' work, contained many updates to MCNP6, including updated delayed particle time bin structure.) Although these comparisons were of $^{235}$U, $^{233}$U, and $^{239}$Pu samples, only $^{235}$U was used for benchmarking purposes. Through advancements in modeling and simulation, the ratios of modeled to measured counts exhibit higher accuracies than fission product ratios in Beddingfield's prior work.

**Table 2.3:** Andrews et al. $^{235}$U fission product photopeak results [2]

| Fission Product | Photopeak Energy (keV) | C/E | Uncertainty |
|---|---|---|---|
| $^{140}$Cs | 602.2 | 0.81 | 14.8% |
| $^{132}$Sb/$^{132m}$Sb | 696.9 | 1.03 | 15.5% |
| $^{93}$Sr | 710.3 | 0.70 | 15.7% |
| $^{145}$Ce | 724.3 | 0.59 | 15.3% |
| $^{90}$Rb/$^{90m}$Rb | 831.7 | 1.03 | 15.5% |
| $^{132}$Sb/$^{132m}$Sb | 973.8 | 0.93 | 15.1% |
| $^{94}$Sr | 427.7 | 0.62 | 14.5% |

## 2.5 The High Flux Isotope Reactor and HFIR-NAA Laboratory

The High Flux Isotope Reactor (HFIR) is an 85 MWth pressurized light water reactor located at Oak Ridge National Laboratory. The core consists two concentric cylinders of Highly Enriched Uranium (HEU) fuel plates surrounded by layers of beryllium

metal (Figure 2.6). A target basket exists in the center of the fuel which reaches neutron fluxes of over $3 \cdot 10^{15}$ $\frac{\text{n}}{\text{cm}^2 \cdot \text{s}}$ and several irradiation positions exist in the beryllium. Additionally, HFIR possesses four horizontal beam ports that are used for thermal and cold neutron scattering research. Each fuel cycle lasts approximately 26 days and 6-7 cycles are run annually.

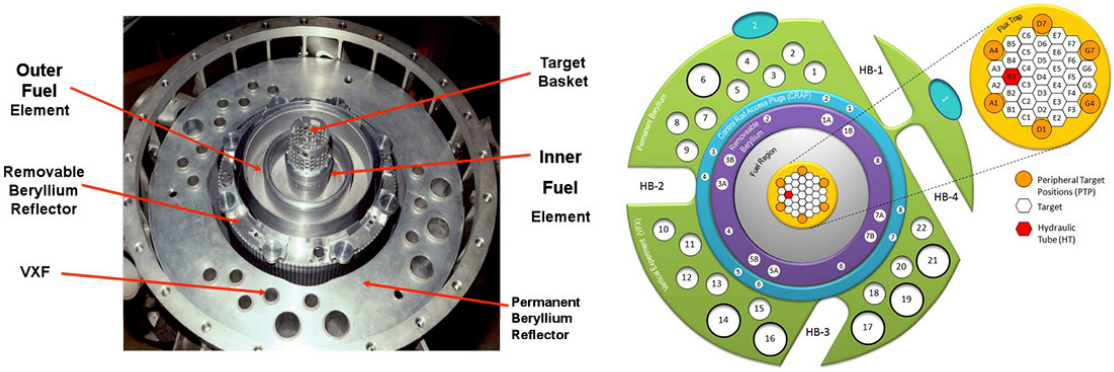



**Figure 2.6:** HFIR Core Diagram [6]

The Neutron Activation Analysis (NAA) laboratory at HFIR was used to conduct irradiations and short-lived fission product measurements to investigate this generalized method. The two pneumatic tubes (PT-1 and 2) at the NAA laboratory enter the core at the VXF-7 position in the outer beryllium and the EF-2 position which is peripheral to the outer beryllium. PT-1 and 2 achieve thermal neutron fluxes of about $4 \cdot 10^{14}$ and $4 \cdot 10^{13}$ $\frac{\text{n}}{\text{cm}^2 \cdot \text{s}}$, with a thermal-to-epithermal ratio of about 45 and 250, respectively (see Figure 2.7). These neutron fluxes are monitored daily using activated Au and Mn diluted in aluminum foil. For samples containing uranium, the highly thermalized flux in these irradiation positions is advantageous for simplifying the fissile mass characterization. While neutron-induced fission is the dominant reaction in $^{235}$U, neutron absorption dominates for $^{238}$U. This allows for a simple quantification of $^{238}$U mass through neutron activation analysis via $^{239}$U gamma-ray measurements (at 74 keV). In addition, the NAA laboratory contains a hot cell, fume hoods, delayed neutron counting station, and multiple HPGe detectors

for sample preparation and measurement. This combination of high neutron flux and nearby counting equipment allows for rapid irradiations and measurements of trace quantities of fissile isotopes. (Figure 2.8) At the NAA facility's current configuration, samples must be transferred from PT exit to HPGe counting equipment by laboratory personnel. This limiting factor necessitates the need for 2 to 5 min of decay for minimizing radiation exposure.

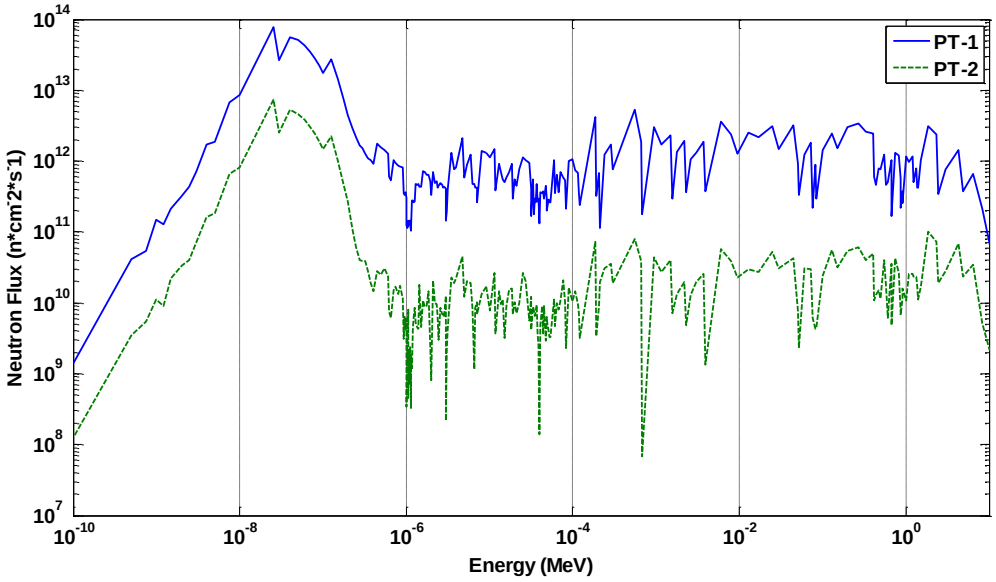



**Figure 2.7:** HFIR PT-1 and PT-2 Flux Spectra (data adopted from[7])

In summary, the HFIR-NAA facility contains an excellent array of capabilities to test the creation and subsequent measurement of short-lived fission product gamma-rays. The combination of a high thermal flux and fast-transfer pneumatic tube access allows for some of the lowest NDA detection limits on fissile isotopes to be obtained. Although the methods described here are developed for HFIR, it is intended to be fully generalizable to any irradiation facility with rapid irradiation and measurement capabilities.

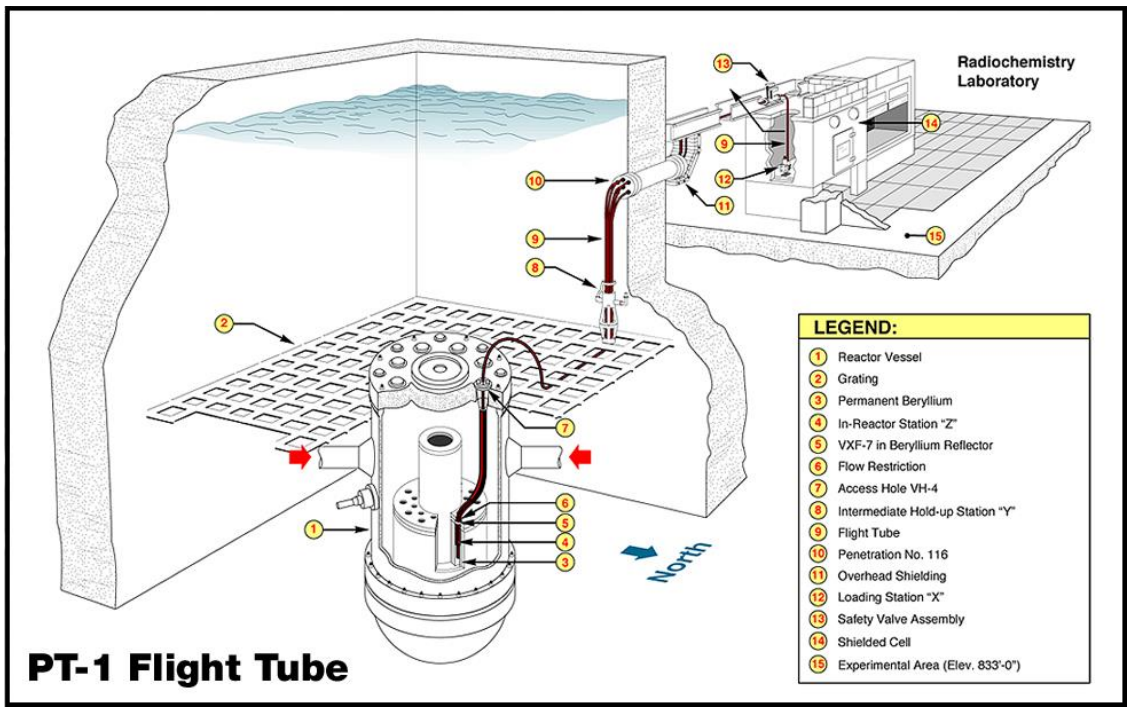



**Figure 2.8:** HFIR-NAA PT-1 Facility (PT-2 has nearly identical layout)

# Chapter 3

# Theory

## 3.1 Fission Product Modeling and Simulation

Traditionally, NAA facilities have used 2-group cross sections consisting of thermal (0.0253 eV) and epithermal (>0.5 eV weighted average) values to represent regions of an interrogating nuclear reactor neutron spectrum [27]. These cross sections are useful for approximations of reaction rates, but generally experience error due to their narrow representation of the interrogating flux spectrum's shape. In the 1970s, the $K_0$ method was developed in order to closer estimate reaction rates for non-1/v isotopes in a general nuclear reactor flux spectrum [28]. This method has been highly touted as an accurate method of Instrumental Neutron Activation Analysis (INAA) [29], and has been implemented at several facilities around the world. Recent research at the National Institute of Standards and Technology (NIST) reactor has shown that limitations exist with this methodology when considering a highly thermalized reactor spectrum [30]. Additionally, similar experiments were conducted at the HFIR-NAA facility to confirm the NIST findings. Due to the low energy resonances in many non-1/v isotopes, the $K_0$ method yields incorrect reaction rates for highly thermalized fluxes. Since HFIR exhibits this highly-thermalized quality, a more comprehensive

cross section development method was implemented using a fully weighted 1-group flux spectrum (Equation 2.3) developed through modeling and simulation.

The bulk of nuclear modeling and simulation was conducted with the SCALE6.1 code suite. SCALE is a modular code system that is globally known for its authority on safety analysis. It contains modules in cross section processing, criticality safety, sensitivity/uncertainty, spent nuclear fuel characterization, radiation source terms, reactor lattice physics, radiation shielding, and nuclear safeguards [31]. SCALE is developed and maintained by Oak Ridge National Laboratory and is one of the most widely used nuclear modeling and simulation packages in the world.

For this work, one-group cross sections and fission yields were developed using the COUPLE module [18] using a multi-group neutron energy spectrum based on the irradiation positions at the HFIR-NAA laboratory (applying equation 2.3). These collapsed cross sections were used with ORIGEN [18] to calculate the fission, transmutation, and decay reactions within the sample to produce calculated fission product inventories. These fission product inventories were then converted, using ENDF gamma-ray libraries, to photopeak emission rates and then integrated over 360 linearly interpolated time intervals to produce a gross photopeak recovery. A visual representation of this process flow is shown in Figure3.1.

In ORIGEN, the production of fission products created after irradiation can be represented by Equation 3.1. This equates the number of fission product atoms after irradiation ($N_{fp}$) as a function of the collapsed one-group total fission cross section ($\sigma_f$), the number of target fissile atoms ($N$), total neutron flux ($\phi$), irradiation time ($t_{irr}$), and individual fission yield ($\gamma_{fy}$) [29]. Due to differences in neutron spectrum shape, the total one-group fission cross section and individual fission yields are unique to each irradiation facility. In this generalized method, this is accounted for by developing the collapsed one-group cross sections (using COUPLE), which can be applied to any facility with a known neutron flux profile.

$$N_{fp} = N\sigma_f\phi\gamma_{fy}\left(\frac{1-e^{-\lambda t_{irr}}}{\lambda}\right) \tag{3.1}$$

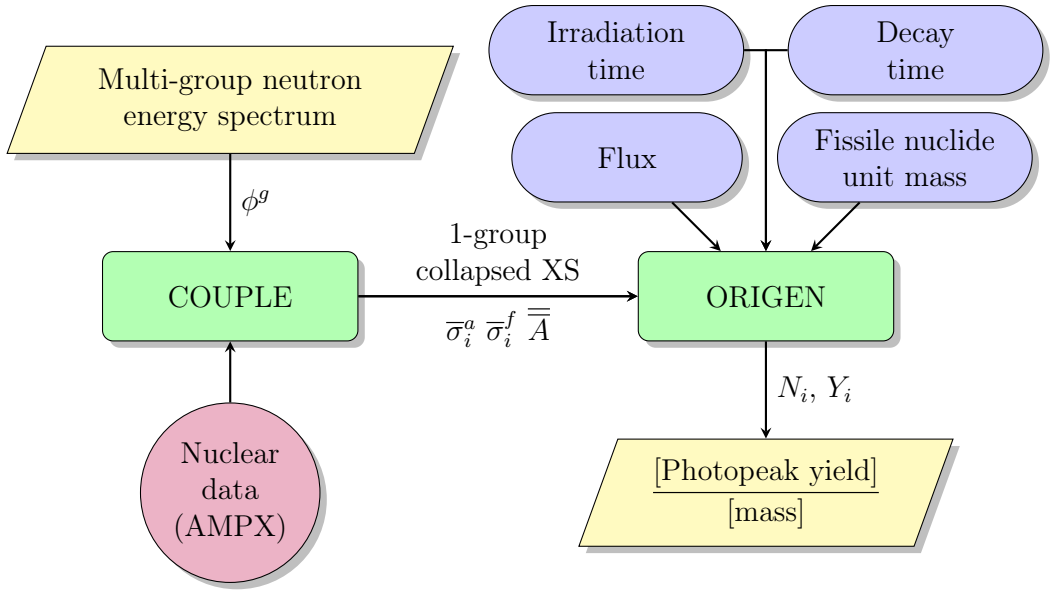



**Figure 3.1:** Flow diagram for SCALE simulations

Once the fission product inventories ($N_{fp}$) are obtained from ORIGEN simulations (Figure 3.1), the relative number of photopeak counts per unit mass ($Y$) can be approximated using Equation 3.2. Since $N_{fp}$ can fluctuate due to decay into or out of the evaluated isotope, changes over the period of measurement are accounted for through ORIGEN simulations. The integrated average of $N_{fp}$ over the measurement period is then used in Equation 3.2. In this relationship, $N_{fp}$ is multiplied by the fission product's decay constant ($\lambda$), measurement time ($t_m$), emission intensity ($\gamma_i$), detector efficiency ($\epsilon$), and a decay correction considering decay time ($t_d$). The detector efficiency value is dependent on detector type, geometry, attenuating material between the source and detector, and energy of the incoming photon [29]. To achieve an accurate approximation of fission product decay during count, Equation 3.2 is calculated using ORIGEN decay simulations over many short time steps. These photopeak yields can then be integrated over the detector measurement time to approximate total photopeak emissions during count. Once calculated, the solution to Equation 3.2 can be used in solving for original fissile mass by entering photopeak

counts per unit mass into Equation 3.3 for each photopeak of interest.

$$Y = N_{fp}\lambda t_m \gamma_i \epsilon (e^{-\lambda t_d}) \tag{3.2}$$

## 3.2 Neutron Flux Characterization

The previously described SCALE modeling and simulation method uses a 238-group neutron flux for input into COUPLE. An accurate understanding of the neutron flux shape is paramount for obtaining reliable fission product generation results. A poor understanding of this shape can cause significant changes in the final photopeak yields, which affects fissile isotope characterizations (evidence of this described in results section). To further generalize these methods, a fully described neutron flux characterization method was conducted on the PT-2 facility. The software package STAYSL-PNNL [32] was used to conduct a neutron flux characterization to demonstrate the generalizability of this method, and develop a high-fidelity model for PT-2. The SCALE 238-group structure (Appendix A) was used consistently in both neutron flux characterization and fission product modeling and simulation[33] .

Historically, neutron flux measurements at the HFIR-NAA facility were conducted using dilute Gold and Manganese monitors in Aluminum foil. Typical masses and concentrations for these samples can be seen in Table 3.1. The 411 keV and 846 keV photopeaks from Au and Mn activation products ($^{198}$Au and $^{56}$Mn) are easily measured and can be used to infer on the interrogating neutron flux. Figure 3.2 shows the ENDF/B-VII.1 capture cross sections for $^{55}$Mn and $^{197}$Au. As can be seen in this figure, the Au capture cross section contains a large resonance in the 1-10 eV region, which makes it a suitable monitor for this epithermal region. This combination of a strong 1/v absorber (meaning that it has a decreasing logrithmic relationship between cross section and energy) and an epithermal monitor has been used at the HFIR-NAA facility to approximate the thermal and epithermal interrogating neutron flux.

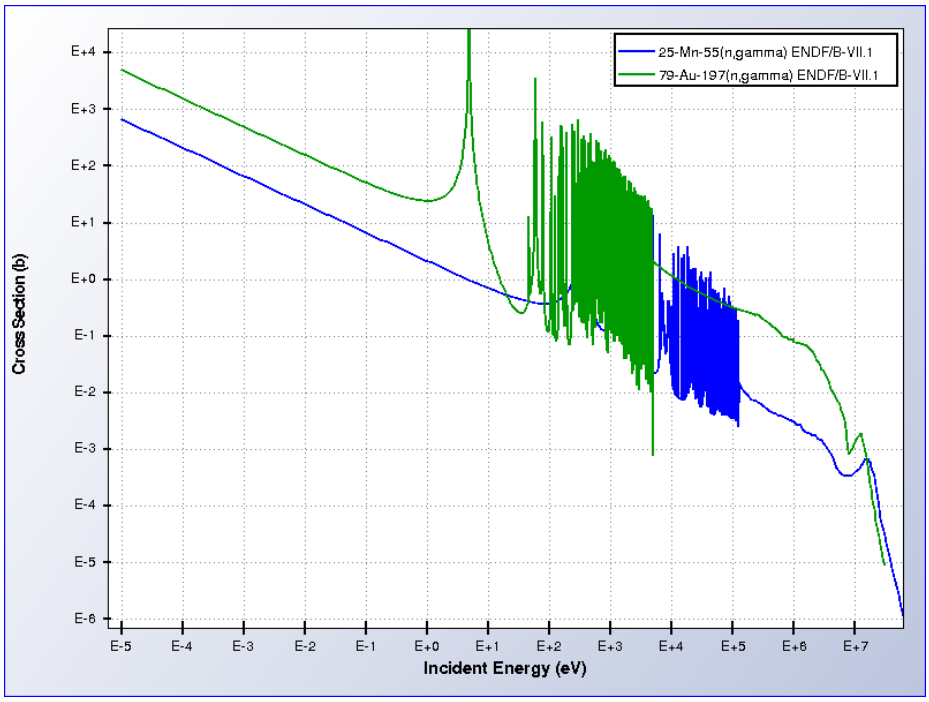



**Figure 3.2:** $^{55}$Mn and $^{198}$Au Capture Cross Sections [3]

Although there is an MCNP model [7] of the HFIR PT-1 and 2 neutron spectra, there has been a history of indications that the calculated PT-2 238-group neutron spectrum may not be accurate. These inaccuracies were discovered by using the SCALE photopeak simulation method (Figure 3.1) for comparison of calculated verses experimental (C/E) activity comparisons of routine Mn and Au irradiation and measurements. When calculating these values over numerous experiments, PT-2 has $^{56}$Mn C/E recoveries that were approximately 20% different than the $^{198}$Au C/E (Table 3.1). This inaccuracy indicates an error in the neutron flux spectrum shape, especially in the epithermal region. The nuclides evaluated in this work add additional importance to understanding this neutron spectrum shape. Figure 3.3 shows that $^{238}$U, $^{239}$Pu, and $^{233}$U contain large resonances in the 0.1-10 eV region, reinforcing the importance of conducting an accurate characterization. Therefore, this work proceeded forward by conducting a complete characterization of the PT-2 neutron flux using the STAYSL-PNNL simulation suite. Detailed parameters of this characterization will be described in the Experimental chapter.

**Table 3.1:** PT-2 Au and Mn Flux Monitoring

| Monitor | Typical Monitor Mass (mg) | Concentration in Al (%) | C/E Observed (%) | After Characterization (%) |
|---|---|---|---|---|
| Au | 70 | 0.1 | 100* | 100* |
| Mn | 20 | 0.0879 | $\approx 80$ | $\approx 98$ |

*The Au monitor was used in determining flux magnitude in SCALE simulations, therefore its C/E recovery is consistently 100%

STAYSL-PNNL is a software suite that contains tools for characterizing an interrogating neutron flux through gamma spectroscopy measurements of activated materials. Cross sections of these irradiated materials can be used in combination with their activation rates in a generalized least-squares approach to calculate a neutron flux with user-defined bin structure (the ENDF 238-group structure was used for this work). STAYSL-PNNL originates from the STAY'SL code developed at Oak Ridge National Laboratory in the late 1970s, and was updated in the 2000s to be more user-friendly for its current version. STAYSL-PNNL contains several modules for calculating the interrogating neutron flux including: NJOY99, NJpp, SHIELD, BCF, SigPhi, and STAYSL-PNNL.

The only third-party software of the suite, NJOY99 is used to take raw data from the Internal Reactor Dosimetry File of 2002 and compile it into neutron reaction cross sections and covariances in the user defined bin structure. The output from NJOY99 is processed using NJpp to format the text file so that it is readable by STAYSL-PNNL and the SHIELD code. SHIELD uses resonance integrals for the calculation of resonance self-shielding correction factors that can affect reaction rates during irradiation. BCF takes irradiation characteristics from the activation foil measurements to generate flux history correction factors. These factors along with the resultant activities from foil irradiations are entered into the SigPhi calculator to develop reaction rate estimate. Finally, STAYSL-PNNL takes both the cross section and covariance data along with the reaction rate estimates to use a system of linear

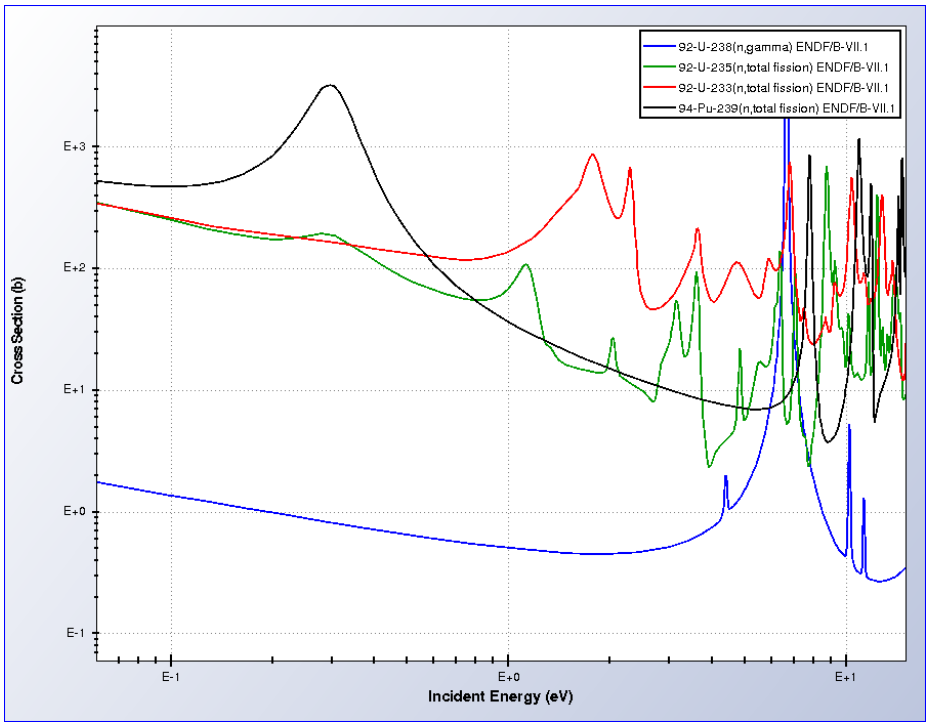



**Figure 3.3:** Fission cross sections for $^{235}$U, $^{233}$U, and $^{239}$Pu along with neutron absorption cross section for $^{238}$U for low energy resonances [3]

equations to estimate the multi-group neutron energy spectrum for a user defined energy structure. Figure 3.4 show a simple flow diagram of these modules. The red colored boxes are modules that are not regularly run, except for when building neutron cross section libraries. SHIELD may not be needed in every flux characterization run if the sample types were analyzed previously for another irradiation.

By applying this neutron flux characterization, the methods described herein can be applied to a reactor facility with unknown flux spectrum. If employed properly, these methods will enable the development of collapsed cross sections, fission product production rates, and gamma source terms for use with experimental data. In the sections following, this modeling and simulation will be put to use in mathematically solving for a sample's fissile constituents in a generalizable manner.

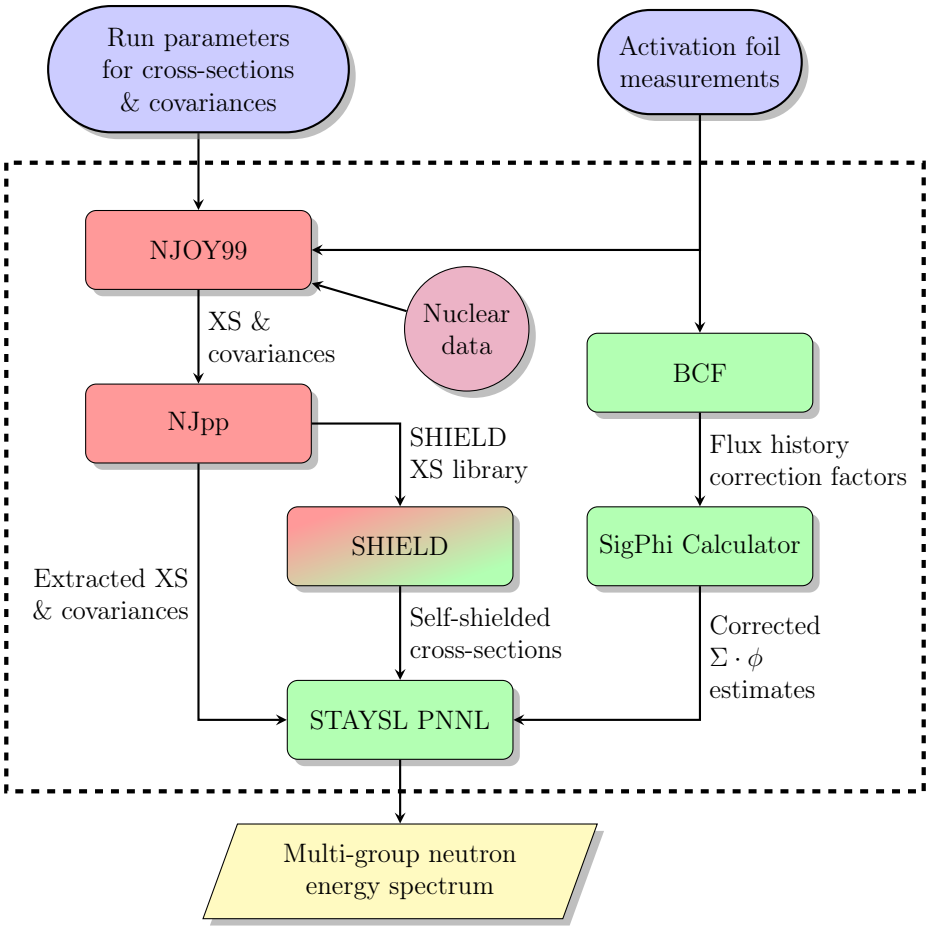



**Figure 3.4:** Flow diagram for STAYSL-PNNL modeling

## 3.3 The Generalized System of Equations

A generalized method to characterize fissile mass through short-lived fission product gamma spectroscopy was developed in this work. This section will describe the mathematical basis behind solving for fissile isotope mass using short-lived fission product gamma spectroscopy. This method is generalized to be applicable to variations in fissile isotopic composition and neutron spectrum by relying on the prediction of fission product yields upon irradiation and using their yield differences to simultaneously solve for original fissile isotope concentration. By exploiting differences in the fission product yields for identifiable short-lived fission products,

the observed fission product activity for each indicator isotope can be directly related to the parent fissile masses.

For this approach, fission product photopeak yields are used to construct an overdetermined system of linear equations and solve for each originating fissile isotope mass (Equation 3.3). The assumption of a linear system can be made since individual fissile isotopes will contribute fission products proportionally to the amount of fluence received given short irradiation periods and minimal burnup (i.e., it is assumed that the target fissile species does not appreciably deplete given the short irradiation time). This system of linear equations uses simulated photopeak total counts ($Y_j$) from a given fission product per unit mass of the parent fissile species, fissile parent isotope mass ($m_j$), and measured photopeak area ($A_p$). Since theoretical photopeak yields will be compared to measured data, SCALE simulation results are used to ensure that the photopeak of interest is without interferences. A version of this equation will exist for every fission product photopeak evaluated in the spectrum, thereby creating an overdetermined system where the fissile mass can be solved for using a linear least-squares matrix regression.

$$\begin{array}{rcccccccc} A_p^1 & = & m_1 Y_1^1 & + & m_2 Y_2^1 & + & \cdots & + & m_j Y_j^1 \\ A_p^2 & = & m_1 Y_1^2 & + & m_2 Y_2^2 & + & \cdots & + & m_j Y_j^2 \\ \vdots & & \vdots & & \vdots & & & & \vdots \\ A_p^n & = & m_1 Y_1^n & + & m_2 Y_2^n & + & \cdots & + & m_j Y_j^n \end{array} \tag{3.3}$$

## 3.4 Solving Overdetermined Systems and Error Propagation

Solving large systems of equations using basic algebraic methods can be tedious and require considerable computational power. Additionally, in an overdetermined system it is not possible to solve for the solution directly [34]. The systems

experienced in this work contain between 1-2 dependent variables and 10-15 separate equations. Therefore, a matrix solution method is what was used for this work. The first step towards solving this system is to convert Equation 3.3 into three separate matrices representing the measured photopeaks ($A_p$), the SCALE calculated theoretical photopeak emissions ($Y_j$) and the unknown fissile isotope masses ($m_j$) (Equation 3.4).

$$\begin{pmatrix} Y_1^1 & Y_2^1 & \cdots & Y_j^1 \\ Y_1^2 & Y_2^2 & \cdots & Y_j^2 \\ \vdots & \vdots & & \vdots \\ Y_1^n & Y_2^n & \cdots & Y_j^n \end{pmatrix} \begin{pmatrix} m_1 \\ m_2 \\ \vdots \\ m_j \end{pmatrix} = \begin{pmatrix} A_p^1 \\ A_p^2 \\ \vdots \\ A_p^n \end{pmatrix} \tag{3.4}$$

These matrices are then simplified into the form seen in Equation 3.5 where [**A**] is the measured peak areas, [**Y**] is the SCALE calculated photopeak yields, and [**M**] is the unknown fissile isotope masses.

$$[\mathbf{Y}][\mathbf{M}] = [\mathbf{A}] \tag{3.5}$$

In order to solve this system using linear least-squares minimization, the matrices are developed into the normal equations [34].

$$[\mathbf{Y}]'[\mathbf{Y}][\mathbf{M}] = [\mathbf{Y}]'[\mathbf{A}] \tag{3.6}$$

The matrix $[\alpha]$ is often referenced as the curvature matrix because each element is twice the curvature of $\sigma^2$ plotted against the corresponding product of variables. This matrix will be useful in calculating out the standard deviation of the mass variables.

$$[\alpha] = [\mathbf{Y}]'[\mathbf{Y}] \tag{3.7}$$

Substituting $[\alpha]$ into Equation 3.6.

$$[\alpha][\mathbf{M}] = [\mathbf{Y}]'[\mathbf{A}] \tag{3.8}$$

Multiplying both sides by $[\alpha]^{-1}$ gives a easily computed solution for the unknown fissile mass matrix [**M**].

$$[\mathbf{M}] = [\alpha]^{-1}[\mathbf{Y}]'[\mathbf{A}] \tag{3.9}$$

In order to calculate the statistical standard deviation for the fissile mass variables in matrix [**M**], the residuals must first be calculated. This is done by multiplying [**Y**] and [**M**] matrices to obtain the calculated values for photopeak area, and then subtract these values from the measured photopeak areas [**A**].

$$[\mathbf{R}] = [\mathbf{A}] - [\mathbf{Y}][\mathbf{M}] \tag{3.10}$$

The calculation of standard deviation for the solved values in [**M**] is then determined by the following equation (Equation 3.11), where degrees of freedom $n$ and $j$ are dimensions of the [**Y**] matrix and $diag\{[\alpha]^{-1}\}$ represents only the diagonal elements of the inverse alpha matrix.

$$s_M^2 = \left(\frac{[\mathbf{R}'][\mathbf{R}]}{n-j}\right) diag\{[\alpha]^{-1}\} \tag{3.11}$$

These calculations were conducted using the computational software MATLAB$^{TM}$ with basic matrix manipulation methods. All of these manipulations took less than 5 seconds of processing time for even the largest of fission product photopeak matrices.

# Chapter 4

# Experimental

## 4.1 HPGe Detector System and Calibration

For this series of experiments, an Integrated Cryocooling System (ICS) with high-purity germanium (HPGe) detector was purchased from ORTEC [35]. This p-type mechanically-cooled coaxial detector is rated at 44% efficiency when compared to a 3x3 NaI detector's detection efficiency of a $^{60}$Co 1332 keV photopeak. Although this detector is also rated for a full-width at half-maximum (FWHM) of 1.8 keV for the 1332 keV peak, the HFIR-NAA lab experienced consistent results at approximately 2.1 keV, indicating that vibrational noise from the cryocooler may have been causing peak broadening. The shaping time of this detector was set considerably high at 12 $\mu s$ in order keep FWHM at its minimum value. This detector was placed inside of a graded shield consisting of about 2 inches of lead covered on the inside with 2 mm of cadmium and 2 mm of copper (Figure 4.1). This graded shield was a significant benefit to the measurements not only because it reduces signal from gamma background in the laboratory, but also because it shields a majority of the $K_\alpha$ x-rays that are emitted from high energy gamma-bombardment on lead.

The gamma spectroscopy collection software used for all of these experiments was Canberra's Genie 2000 [36]. Genie 2000 has been used by research and industry for



**Figure 4.1:** HFIR-NAA Facility Graded Shield with HPGe Detector

well over a decade with an easy to use interface for operation and setup of a digital multi-channel analyzer (MCA). The MCA used in these experiments was a Canberra Lynx digital MCA [37]. This MCA contains over 32,000 channels and is capable of operating in Pulse-Hight Analysis (PHA), Multi-Channel Scalar (MCS), and Dual Loss-Free Counting (DLFC) modes.

Energy and efficiency calibrations were conducted on this detector in order to identify fission products and approximate actual photopeak emission rates. A series of single isotope sealed sources, certified by Amersham in October 1st of 1987, were used to construct these calibrations. Details on these sources can be found in Table 4.1. These sources were used to calibrate energy (Equation 4.1) and efficiencies at 100 mm and 300 mm positions above the detector endcap (Equations 4.2 and 4.3). Figure 4.2 shows both efficiency calibrations graphically.

$$E = 0.2133 \cdot (\text{Channel}) - 0.042 \tag{4.1}$$

$$log(\epsilon) = -2.606 \cdot 10^{-4} E - 2.368 + \frac{1.012 \cdot 10^{2}}{E} - \frac{6.11 \cdot 10^{3}}{E^{2}} \tag{4.2}$$

$$log(\epsilon) = -1.407 \cdot 10^{-4} E - 3.358 + \frac{1.851 \cdot 10^{2}}{E} - \frac{1.603 \cdot 10^{4}}{E^{2}} + \frac{3.238 \cdot 10^{5}}{E^{3}} \qquad (4.3)$$

**Table 4.1:** Sources Used in HPGe Detector Calibration

| Source | Half-Life | Photopeaks Evaluated (keV) |
|---|---|---|
| $^{241}$Am | 432.6 y | 59.5 |
| $^{133}$Ba | 10.55 y | 80.0, 302.9, 276.4, 356.0, 383.9 |
| $^{137}$Cs | 30.08 y | 661.7 |
| $^{22}$Na | 2.602 y | 1274.5 |
| $^{60}$Co | 5.271 y | 1173.2, 1332.5 |

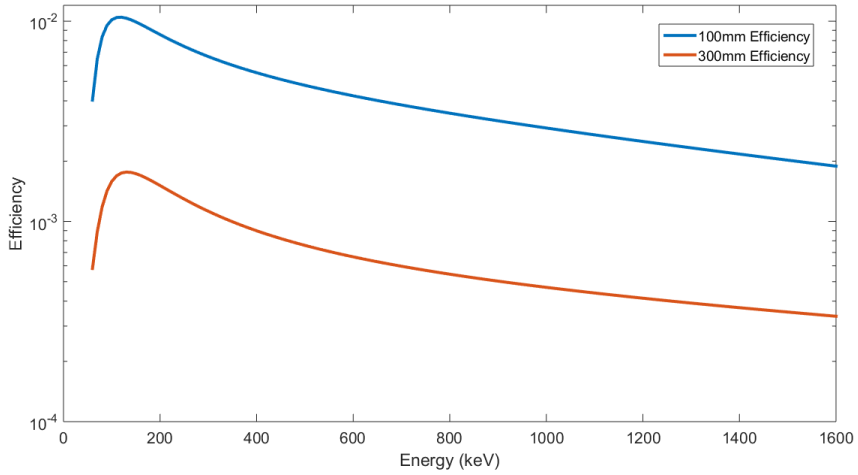



**Figure 4.2:** HPGe Calibrated Efficiency Plots for 100mm and 300mm measurement positions

Post-processing of gamma spectra was conducted using PeakEasy software [38]. PeakEasy was developed by Los Alamos National Laboratory and Sandia National Laboratories in 2006 for rapid nuclide identification and analysis of gamma-ray spectra. PeakEasy was used in this work due to its high accuracy in producing

Gaussian fits to measured photopeaks, and precise replication of those fits over a batch processing routine.

## 4.2 Loss Free Counting

As mentioned in the Background section, Dual Loss-Free Counting (LFC) methods are useful for gamma spectroscopy at high detector dead-times and rapidly decaying isotopes. The Lynx MCA allows for the use of an LFC mode called Dual Loss Free Counting (DLFC). In this mode, DLFC allows for the real-time acquisition of events, and will produce two spectra. One spectrum contains live time corrected counts, and the other produces the normal uncorrected counts. This allows for uncertainty to be derived from the uncorrected spectrum, due to the non-Poisson nature of the corrected spectrum [37]. For the experiments described in this work, the majority of fission product isotopes measured experience at least one half-life over the period of measurement and dead-times range between 10% and 35%. These conditions make DLFC mode of unique utility in making an accurate measurement of a decaying fission product's activity during count. Efforts were taken at the HFIR-NAA facility to validate the accuracy of DLFC mode with known sources in conditions that mimic the experiments described herein.

Using the same $^{241}$Am source from Table 4.1 to steadily increase dead time, the HPGe detector was operated in both Pulse Height Analysis (PHA) and DLFC modes while measuring a $^{137}$Cs source. Dead-time was increased by steadily bringing the $^{241}$Am closer to the detector endcap and these positions were recorded in PHA mode and replicated for DLFC measurements. From this set of experiments, DLFC mode shows a steady count rate throughout the variations in dead time within the uncertainty bounds. As can be seen in Figure 4.3, increasing dead-times result in a reduction of count rate in PHA mode when the $^{137}$Cs 662 keV photopeak integral counts are divided by real time. This is regularly corrected for by using the MCA calculated live-time (Equation 2.4), but this cannot be done for these experiments

for two main reasons. First, the SCALE modeling and simulations must be an exact representation of detector acquisition time, without variations due to sample activity. If PHA mode were to be used, detector live-time would constantly be changing and making it appear that isotopes were not decaying at their usual rates, thus yielding unreliable results. Secondly, a changing dead-time causes a continual changes in the dead-time correction factor, and causes activities to be poorly represented for rapidly decaying isotopes (shown in Figure 2.4).

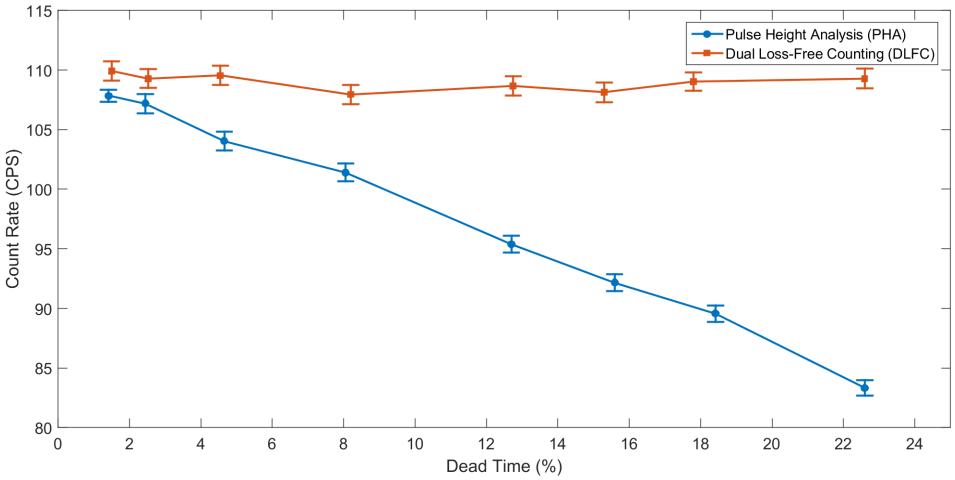



**Figure 4.3:** DLFC and PHA Comparison

Through this set of experiments, it was shown that DLFC mode accurately replicates a known source's activity through a wide range of dead times. Likely the main advantage of this capability is to have detector live time equate to real time. This allows for theoretical production and decay of short-lived fission product isotopes to be compared to measured spectra side-by-side.

## 4.3 Irradiation Setup

The High Flux Isotope Reactor Neutron Activation Analysis (HFIR-NAA) facility was used for the experiments conducted in this work. As mentioned earlier, this facility consists of two pneumatic tubes (PT-1 and 2) that were each used in the following

irradiation experiments. For the fissile isotope irradiations, high density polyethylene sample containers ("rabbits") were used to transport each sample into the reactor for an irradiation of 60 seconds or less. Figure 4.4 shows an example polyethelene rabbit along with an International Atomic Energy Agency (IAEA) "J-swipe" that is used in some measurement cases described in this work. Upon exiting the reactor, the samples are brought back to either a shielded cubicle (Figure 4.5) or a fume hood (PT-2) for unpackaging. Once unpackaged, each sample is carried by hand into an adjacent room that contains the HPGe detector described previously (Figure 4.1).

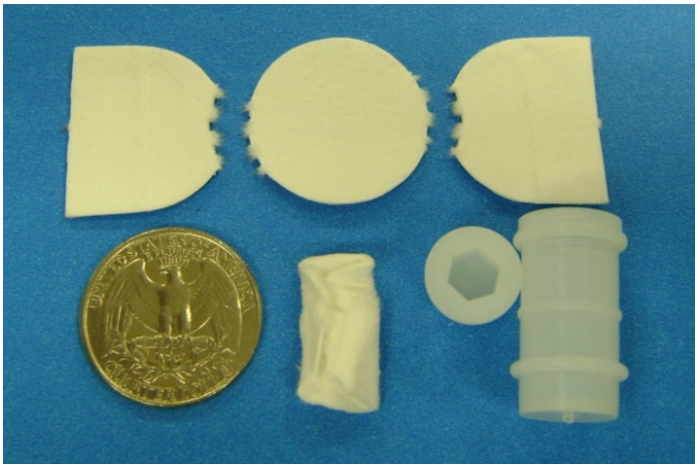


**Figure 4.4:** High-Density Polyethelene Rabbit with IAEA J-Swipe

## 4.4 PT-1 Benchmarking Fission Product Photopeak Simulations to Prior Work

Irradiations and subsequent measurements were conducted at the HFIR-NAA laboratory to benchmark the SCALE6.1 modeling and simulation scheme (Figure 3.1) to the aforementioned prior work. A comparison to results presented in Table 2.2 was made using similar irradiation and measurement conditions at the HFIR-NAA laboratory (Table 4.2). This irradiation was conducted using 7 $\mu$g of natural uranium (49.7 ng $^{235}$U) from an ICP-MS certified standard with 20 s of irradiation time in




**Figure 4.5:** PT-1 Facility with Shielded Cubicle

a PT-1 thermal flux of approximately $4 \cdot 10^{14}$ $\frac{\text{n}}{\text{cm}^2 \cdot \text{s}}$. The sample was then allowed 875 s of decay before 600 s of measurement with a HPGe detector. These results exhibit a strong identification of $^{235}$U and close the significant gap between biases in observed to theoretical ratios experienced in Table 2.2, validating the approach proposed by Beddingfield and thereby suggesting that a more generalized approach based on short-lived fission product measurements can lead to the quantification of fissile U and Pu.

Additionally, a comparison to the results in Table 2.3 was made using the HFIR-NAA laboratory. This irradiation was conducted using the same 7 $\mu$g natural uranium sample and irradiation conditions from the Beddingfield benchmark, but was a prior 600 s measurement that only had 275 s of decay. This shorter decay period more closely represents the rapid irradiation and decay periods used by Andrews et al. [2]. The comparison of SCALE simulations to HFIR-NAA irradiation and measurements exhibited comparable accuracy to the work conducted by Andrews et al. (Table 4.3).

**Table 4.2:** SCALE simulation and HFIR-NAA benchmark to Beddingfield et al. [1]

| Numerator Isotope | Energy (keV) | Denominator Isotope | Energy (keV) | $r_{Pu}$ | $r_U$ | $r_{obs}$ | Uncert. | Bias |
|---|---|---|---|---|---|---|---|---|
| $^{89}$Rb | 1031.9 | $^{130}$Sb/$^{130*}$Sb | 839.4 | 0.64 | 1.96 | 1.87 | 11.5% | -4.38% |
| $^{89}$Rb | 1031.9 | $^{142}$Ba | 1000.9 | 2.28 | 5.27 | 4.99 | 12.3% | -5.34% |
| $^{94}$Y | 918.8 | $^{131}$Sb | 933.1 | 0.20 | 0.37 | 0.36 | 9.5% | 2.28% |
| $^{90}$Rb/$^{90*}$Rb | 831.7 | $^{130}$Sb/$^{130*}$Sb | 839.4 | 0.41 | 0.62 | 0.59 | 38.8% | 4.84% |
| $^{90}$Rb/$^{90*}$Rb | 831.7 | $^{133m}$Te | 912.7 | 3.78 | 5.66 | 5.25 | 9.5% | 7.14% |

Comparisons to these two state of the art short-lived fission product measurement methodologies show that the SCALE modeling and simulation scheme presented here performs far above expectations. It is hypothesized that this high accuracy is due to the application of a 238-group collapsed cross section, DLFC counting mode, iterative simulations for the detector acquisition period, and careful detector calibration. Making these accurate determinations of fission product production rates is paramount to conducting a high-fidelity fissile sample characterization since small variations in the modeled values for some fission products can cause the system of equations (Equation 3.3) to yield inaccurate results.

## 4.5 PT-2 Flux Characterization

As described in the Neutron Flux Characterization section, the MCNP model developed for PT-2 has shown significant error in routine flux monitor measurements (Table 3.1). Therefore, it was soon realized that a full flux characterization of the PT-2 irradiation position had to be conducted. The code package STAYSL-PNNL was used for this characterization, enabling a full 238-group characterization using a set of flux monitors. Since the thermal flux of the PT-2 irradiation position is very high,

**Table 4.3:** SCALE simulation and HFIR-NAA benchmark to Andrews et al. [2]

| Fission Product | Photopeak Energy (keV) | C/E | Uncertainty |
|---|---|---|---|
| $^{140}$Cs | 602.2 | 0.98 | 11.1% |
| $^{132}$Sb/$^{132m}$Sb | 696.9 | 1.05 | 4.5% |
| $^{93}$Sr | 710.3 | 0.88 | 7.2% |
| $^{145}$Ce | 724.3 | 0.93 | 4.1% |
| $^{90}$Rb/$^{90m}$Rb | 831.7 | 1.29 | 2.5% |
| $^{132}$Sb/$^{132m}$Sb | 973.8 | 0.98 | 4.2% |
| $^{94}$Sr | 427.7 | 0.93 | 2.9% |

characterization of any reactions above the thermal region is a significant challenge. Therefore, a cadmium-shielded graphite rabbit was used for this irradiation. The $^{113}$Cd isotope has a significant thermal absorption cross section until approximately 0.5 eV (Figure 4.6), meaning that it is capable of blocking a majority of the thermal neutrons experienced in PT-2. Therefore, a characterization of the epithermal and fast regions of the neutron energy spectrum can be adequately characterized.

A closed cadmium cylinder of 2 mm wall thickness was inserted into a graphite rabbit for irradiation in PT-2. A graphite rabbit was used for the purpose of heat dissipation. Since there is an enormous number of thermal neutron reactions with the $^{113}$Cd, it is expected that a polyethylene rabbit may melt. A series of monitors was prepared and inserted into an aluminum packet, which was then inserted within the Cd cylinder. Some of these monitors utilized threshold reactions of (n,$\alpha$) and (n,p) to sample the flux in epithermal and fast regions, while others maintained thermal reactions to sample within the lower energy regions of the neutron spectrum. Table 4.4 lists the samples prepared and their weights. The column labeled 95% of Reactions Range (MeV) is an optional output of STAYSL-PNNL that shows the

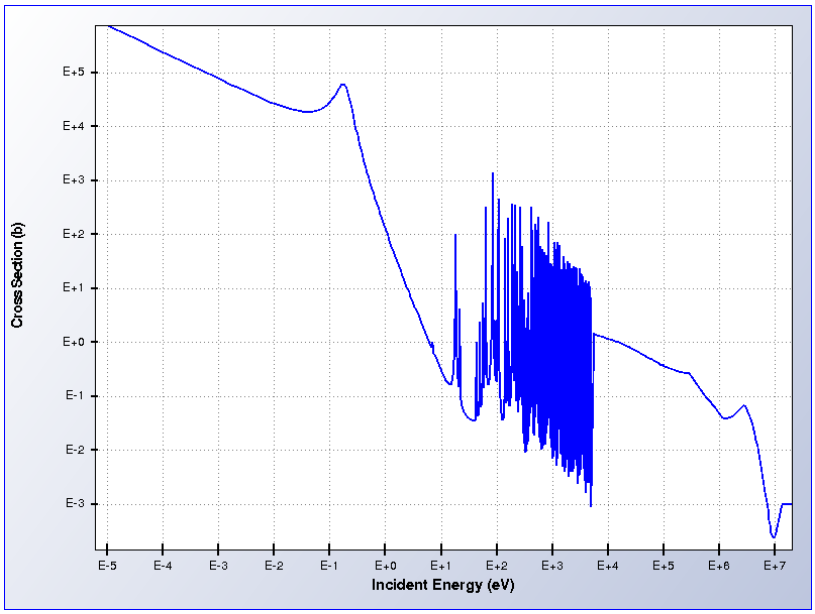



**Figure 4.6:** $^{113}$Cd Neutron Absorption Cross Section [3]

neutron energy region of the interrogating spectrum. This was produced after these experiments were conducted, but serve as a useful guide to understanding the main characterization regions of each monitor.

This packet of flux monitors was irradiated in the PT-2 facility for 30 minutes at full reactor power (total flux of $4.1 \cdot 10^{13}$ $\frac{\text{n}}{\text{cm}^2 \cdot \text{s}}$). After irradiation, the graphite rabbit sat in a decay station for approximately 12 hours to allow for the short-lived $^{117}$Cd and $^{28}$Al to decay, which can pose a considerable radiation hazard. These flux monitors were then removed from the Cd sheath and Al packet to be measured individually on the described HPGe detector at a height of 300 mm (efficiency defined as Eq. 4.3).

These activities along with irradiation and measurement characteristics were then entered into the STAYSL-PNNL code suite. In order to perform the spectral adjustment, a spectrum "guess" must be defined. This was designed to mimic the HFIR flux spectrum, but in a generalized manner. This was done by taking a 4 group moving average for the PT-2 MCNP predicted spectrum, up until a neutron energy of 1 eV. From 1 eV, a flat neutron spectrum at a flux of $1 \cdot 10^{10}$ $\frac{\text{n}}{\text{cm}^2 \cdot \text{s}}$ was given.

**Table 4.4:** Flux Characterization Measurement Monitors

| Reaction | 90% of Reactions Range (MeV) | Sample Type | Sample Mass (g) | Product Half-Life |
|---|---|---|---|---|
| $^{27}Al(n,\alpha)^{24}Na$ | 6.43 to 17.3 | Al Foil | 0.0872 | 15.0 h |
| $^{46}Ti(n,p)^{46}Sc$ | 4.30 to 15.7 | Ti Foil | 0.0285 | 83.8 d |
| $^{47}Ti(n,p)^{47}Sc$ | 2.48 to 15.7 | Ti Foil | 0.0285 | 3.35 d |
| $^{48}Ti(n,p)^{48}Sc$ | 6.43 to 17.3 | Ti Foil | 0.0285 | 43.7 h |
| $^{54}Fe(n,p)^{54}Mn$ | 3.00 to 14.6 | Fe Wire | 0.0293 | 312 d |
| $^{58}Fe(n,\gamma)^{59}Fe$ | $9.25\cdot10^{-7}$ to $6.00\cdot10^{-3}$ | Fe Wire | 0.0293 | 44.5 d |
| $^{59}Co(n,\gamma)^{60}Co$ | $3.73\cdot10^{-6}$ to $1.22\cdot10^{-4}$ | Co-Al Wire (0.116%) | 0.0203 | 5.27 y |
| $^{58}Ni(n,p)^{58}Co$ | 2.48 to 13.8 | Ni Wire | 0.0185 | 70.9 d |
| $^{197}Au(n,\gamma)^{198}Au$ | $5\cdot10^{-9}$ to $4.75\cdot10^{-6}$ | Au-Al Foil (0.1%) | 0.0219 | 2.70 d |

Figure 4.7 shows the adjustment that STAYSL-PNNL conducted on the spectrum after entering in activities from neutron reactions described in Table 4.4.

One important measure of the effect and success of this methodology is to see how the STAYSL-PNNL output compares with the MCNP generated 238-group neutron spectrum. Figure 4.8 shows the two generated spectra side-by-side. There are many similarities in the features between the two spectra, though with a few key differences. From simple observation, it was noticed that the thermal flux was slightly higher and the epithermal and fast flux is significantly depressed. A more quantitative way of displaying this information is through use of Equation 4.4. In this equation, the thermal flux at 0.0253 eV is multiplied by the reciprocal of an energy-weighted flux from 0.5 eV to 20 MeV (grouping structure listed in Appendix A). This value, along with an integrated thermal flux (sum of all bins from 0–0.5 eV) are reported in Table 4.5.

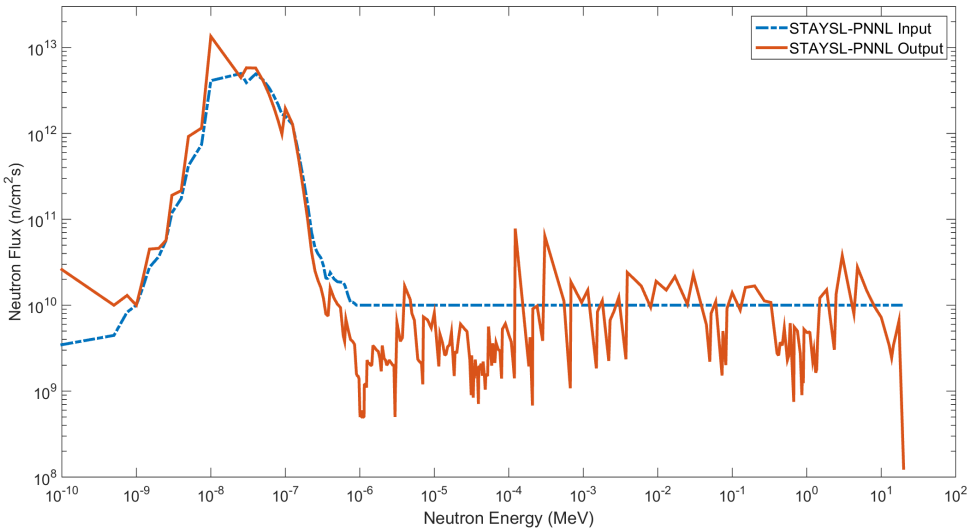



**Figure 4.7:** STAYSL-PNNL Corrected PT-2 Spectrum compared to STAYSL-PNNL Input Spectrum

$$\frac{\text{Th}}{\text{Epi}} = \frac{\phi_{th} \cdot \sum_{g=37}^{238} \Delta E_g}{\sum_{g=37}^{238} \phi_g} \tag{4.4}$$

**Table 4.5:** PT-2 Corrected/Uncorrected Spectra Comparison

| | Total Thermal Flux $(n/cm^2s)$ | Th/Epi |
|---|---|---|
| MCNP Spectrum | $3.8977 \cdot 10^{13}$ | 133.7 |
| STAYSL-PNNL Correction | $4.7850 \cdot 10^{13}$ | 625.9 |

The significant increase in Th/Epi ratio means that a change to reaction rates for the fissile nuclides can occur. As shown in Figure 3.3, the nuclides measured in this work have substantial resonances in the epithermal region. The 238-group spectrum

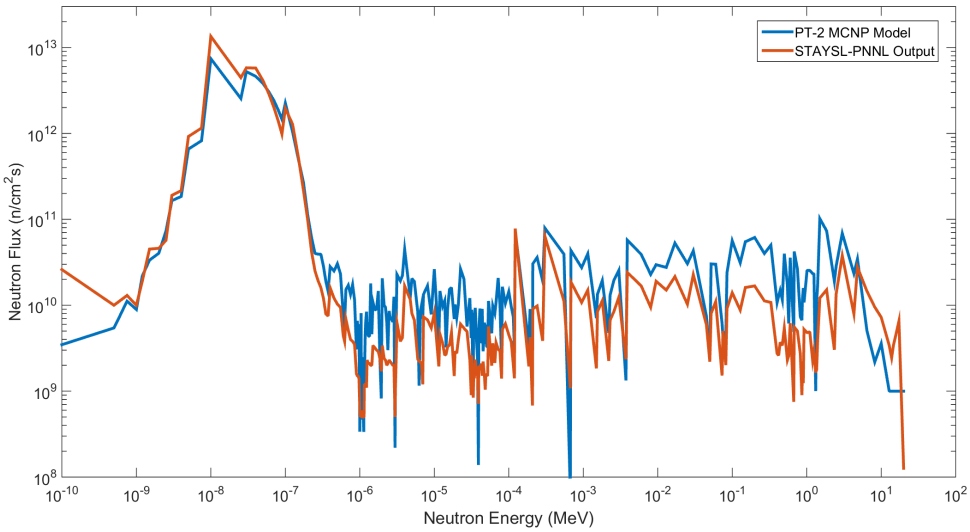



**Figure 4.8:** STAYSL-PNNL Corrected PT-2 Spectrum Compared to MCNP Prediction

directly affects the 1-group cross-section collapse conducted in the SCALE modeling scheme (3.1), altering the final photopeak yields predicted by nuclear data. The full effect of this characterization will be described further in the Results section.

With the characterization conducted with STAYSL-PNNL, a 238-group neutron flux spectrum was able to be made with little prior knowledge of the flux shape. This gives significant confidence in applying these methods to other reactor facilities that may not have a fully explicit MCNP model of their irradiation position.

## 4.6 $^{239}$Pu and $^{235}$U Indicators Scoping Study

Since a binary mixture measurement is more complex, a careful selection of photopeaks used for analysis was conducted to guide the irradiation and measurement routine. This selection process involved SCALE simulations of PT-2 irradiations and post-processing of output in MATLAB to simulate a hypothetical detector response over the measurement period ($T_{start}$ to $T_{stop}$). As explained previously, SCALE simulations were used to generate the expected photopeak counts for each

fission product nuclide resulting from each fissile parent over many time intervals (Figure 3.1). Using MATLAB, these gamma-line spectra were then integrated over hypothetical measurement periods and multiplied by efficiency, which generated an expected number of counts ($n$) at a given energy. The outputs of this MATLAB script were the fractional standard deviation ($\sigma$) (Equation 4.5) and indicator photopeak ratio (Equations 4.6 and 4.7). For this scoping study, only $^{235}$U and $^{239}$Pu were evaluated due to the interest in distinguishing these two isotopes.

$$\sigma = \frac{\sqrt{n}}{n} \tag{4.5}$$

$$^{235}\text{U Indicator Ratio} = \frac{\text{Photopeak Counts}/^{235}\text{U Fission}}{\text{Photopeak Counts}/^{239}\text{Pu Fission}} \tag{4.6}$$

$$^{239}\text{Pu Indicator Ratio} = \frac{\text{Photopeak Counts}/^{239}\text{Pu Fission}}{\text{Photopeak Counts}/^{235}\text{U Fission}} \tag{4.7}$$

The ORIGEN simulations represented 60 s irradiations of 10 ng quantities of $^{235}$U and $^{239}$Pu at the PT-2 facility with many variations of measurement intervals from 10 to 1200 s of decay. Additionally, detector characteristics were of a p-type HPGe of 44% relative efficiency with samples measured at 25 cm from the endcap. Decay times and source-to-detector distance were determined in anticipation of a new system configuration in the NAA laboratory where the HPGe detector is significantly closer to the PT 2 system, and an experimenter does not need to remove a sample from the system before measurement. The MATLAB script written to evaluate these ORIGEN simulations rejected $^{235}$U and $^{239}$Pu indicators that contained photopeak ratios of less than 1.5 and also required the fractional standard deviation for the photopeak to be less than 10.0%. Results of this study are displayed graphically in Figure 4.9. The strongest indicators for $^{235}$U and $^{239}$Pu are labeled, and the nuclides with the lowest fractional standard deviations are highlighted and detailed in Table 4.6.

It was soon realized that not all fissile isotope indicators could be collected in the HFIR-NAA facility with its current configuration. The samples being ejected to a

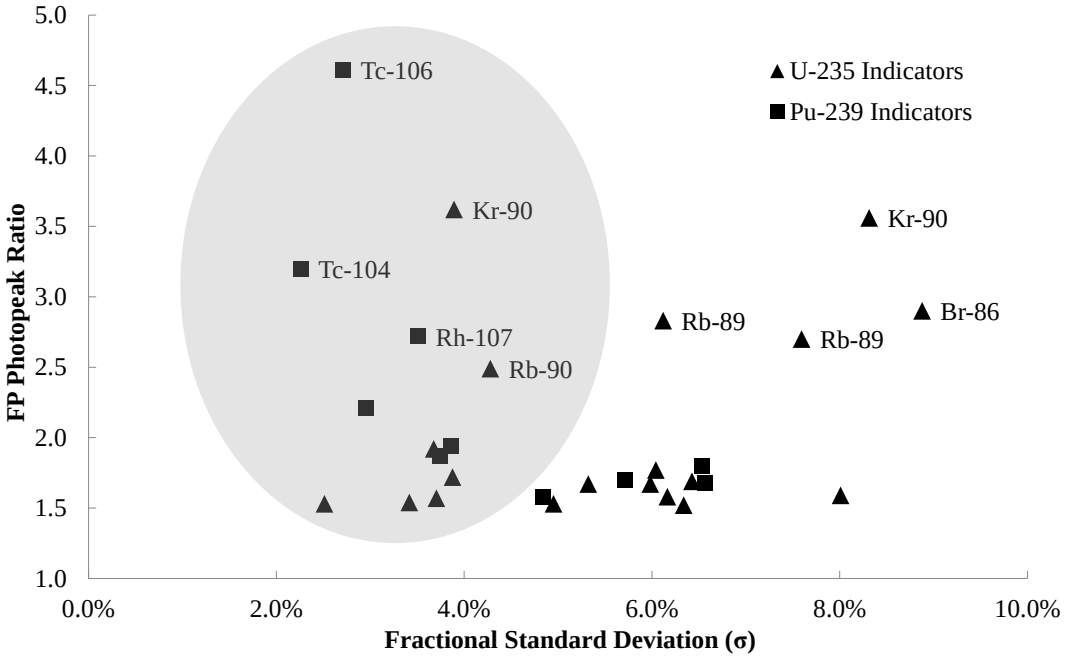



**Figure 4.9:** Graph of Fission Product Indicators for $^{239}$Pu and $^{235}$U

fume hood or shielded cubicle requires some experimenter manipulation in order to get the sample to a detector. Therefore, isotopes of $T_{stop}$ periods of 300 seconds or less were not expected to be reliably measured. Nevertheless, this set of modeling scenarios does help inform for future work in the area of fission product indicators, in which earlier time intervals are expected to be expanded on.

## 4.7 Samples Evaluated

Table 4.7 lists the standards used in all of the experiments for this work. Each began with an ICP-MS certified standard and was diluted in 5% $HNO_3$ to the specified concentration using solution weights. These standards were later verified with delayed neutron counting methods commonly practiced in the HFIR-NAA facility [39]. Since these samples are thoroughly dissolved in an acid solution, aliquots were added to polythene inserts by using a standard micro-liter scale pipette. In order to maintain the highest accuracy in measurement, inserts were weighed with a mass balance

**Table 4.6:** Listed info on FP Indicators for $^{239}$Pu and $^{235}$U

| Parent Fissile Isotope | $T_{start}(s)$ | $T_{stop}(s)$ | Photopeak Energy (keV) | FP Isotope | Fraction Std Dev | Photopeak Ratio |
|---|---|---|---|---|---|---|
| $^{235}$U | 10 | 100 | 121.8 | $^{90}$Kr | 3.89% | 3.62 |
| | 10 | 300 | 397.4 | $^{144}$La | 2.51% | 1.53 |
| | 10 | 300 | 541.2 | $^{144}$La | 3.67% | 1.92 |
| | 10 | 300 | 602.3 | $^{140}$Cs | 3.70% | 1.57 |
| | 10 | 600 | 1427.7 | $^{94}$Sr | 3.88% | 1.72 |
| | 40 | 600 | 590.2 | $^{93}$Sr | 3.42% | 1.54 |
| | 40 | 600 | 831.7 | $^{90}$Rb | 4.28% | 2.49 |
| $^{239}$Pu | 10 | 300 | 270.1 | $^{106}$Tc | 2.71% | 4.61 |
| | 10 | 600 | 424.0 | $^{84}$Br | 3.75% | 1.87 |
| | 40 | 300 | 135.4 | $^{117}$Ag | 2.95% | 2.21 |
| | 40 | 300 | 348.7 | $^{112}$Rh | 3.86% | 1.94 |
| | 100 | 1200 | 358.0 | $^{104}$Tc | 2.26% | 3.20 |
| | 300 | 1200 | 302.8 | $^{107}$Rh | 3.51% | 2.72 |

sensitive to $10^{-4}$ g which was tared from the gross weight, measured immediately after aliquoting the solution to the insert. After this, samples were placed in a drying oven overnight in order to evaporate all of the acid solution from within the insert. Following this, inserts were placed within a high density polyethylene rabbit (Figure 4.4) in which the lid was heat-sealed with a soldering iron in preparation for irradiation in one of the two pneumatic tubes at the HFIR-NAA facility.

## 4.8 Irradiation and Measurement Characteristics

Table 4.8 shows the irradiation and measurement characteristics for this set of experiments. These configurations were determined by SCALE modeling and

**Table 4.7:** Listed Sample Info for Solutions Containing $^{239}$Pu, $^{235}$U, and $^{233}$U

| Solution | Concentration ($\mu g/g$) Elemental | Fissile |
|---|---|---|
| Natural Uranium in 5% $HNO_3$ | 1000 | 7.200 |
| Depleted Uranium in 5% $HNO_3$ | 1000 | 3.384 |
| High Purity $^{233}$U in 5% $HNO_3$ | 7.851 | 7.831 |
| Plutonium in 5% $HNO_3$ | 1.677 | 1.300 |

simulation described in the indicators scoping study section. Also prior experiments conducted with small fissile samples were used to understand the capabilities for sample removal, processing, and detector response. The objectives of these configurations were to obtain photopeak statistics of less than 10% uncertainty, maintain dead times to less than 30%, and keep the total analysis shorter than ten minutes per sample.

**Table 4.8:** Irradiation and Measurement Characteristics

| Sample Set | Irradiation Time (s) | Decay Time (s) | Measurement Time (s) | Measurement Height (mm) |
|---|---|---|---|---|
| PT-1 Single Elements | 20 | 120 | 360 | 300 |
| PT-2 Single Elements | 25 | 120 | 360 | 100 |
| PT-2 Binaries | 25 | 120 | 360 | 100 |
| PT-2 IAEA Swipes | 60 | 120 | 360 | 300 |

The fission product isotopes evaluated in these experiments are displayed in Table 4.9. These isotopes were evaluated in previous experiments and modeling to verify their identities in short-lived fission product gamma spectra, and also verify that they do not contain interferences with other photopeaks that may be overlapping or causing the peaks to not be baseline resolved. Additionally, higher energy photopeak

were preferentially chosen due to the higher predictability in detection efficiency, and limited spectral effects.

**Table 4.9:** Fission Product Isotopes and Photopeaks Evaluated

| Fission Product | Photopeak (keV) | Half-Life (m) |
|---|---|---|
| $^{94}$Sr | 1427.7 | 1.25 |
| $^{132}$Sb | 973.9 | 3.50 |
| $^{94}$Y | 918.7 | 18.7 |
| $^{93}$Sr | 875.9 | 7.41 |
| $^{90}$Rb | 831.7 | 3.40 |
| $^{145}$Ce | 724.3 | 3.00 |
| $^{132}$Sb | 697.4 | 3.50 |
| $^{140}$Cs | 602.3 | 1.06 |
| $^{93}$Sr | 590.2 | 7.41 |
| $^{108}$Rh | 434.2 | 6.0 |
| $^{133}$Te | 407.6 | 12.4 |
| $^{144}$La | 397.4 | 0.68 |
| $^{104}$Tc | 358.0 | 18.2 |

# Chapter 5

# Results

## 5.1 Photopeak Modeling Results

Before solving the overdetermined system of equations (Equation 3.3), the theoretical fission product photopeak yields had to be calculated. This was computed with the SCALE modeling and simulation scheme described previously (Figure 3.1) using an input deck with the adjusted PT-2 and PT-1 238-group neutron fluxes. The irradiation and decay characteristics input to match each experimental process displayed in Table 4.8. The gamma source term output was calculated over 450 energy bins (from 70 keV to 1450 keV) and over 360 time iterations (1 per second of measurement), providing a substantially large matrix. Each gamma source term (measured in photons per second) was summed for all time iterations then divided by the time bin width, giving a total photopeak emission value for the period of measurement. The reason for this time binning and integration was to capture the effects of isotope ingrowth and decay during measurement. This value was then multiplied by detection efficiency for a direct comparison to HPGe output. For each nuclide irradiation case, the computational time on a desktop PC was approximately 10 minutes. Since there were 4 separate experiments conducted, each with its unique irradiation and decay characteristics, 16 input decks were run in a batch routine

with a total computational time of greater than 160 minutes. Even though it was somewhat time-consuming, this process is not expected to be replicated often for a facility that has relatively constant flux in the irradiation position used. Since the photopeak emission rate is normalized to mass, and applied in a generalized manner using the system of equations, it can be repeated for numerous simple sets containing varying amounts of fissile mass and combinations of mixtures.

This data processing reduced each SCALE output down to efficiency corrected photopeak counts per nanogram of fissile material irradiated in either PT-1 or PT-2. Two tables of data representing this final output are displayed in Table 5.1 and Table 5.2. These values can then be entered in as $Y_i$ values in the overdetermined system of equations (Equation 3.3). It should be noted that more several more of these tables of data were generated in the analysis of short-lived fission product signatures, but these are provided as representative of the typical output used.

**Table 5.1:** Photopeak Modeling Results for PT-1 Single Elements Case

| Isotope | Photopeak (keV) | $(^{counts}/_{ng})$ $^{239}$Pu | $^{233}$U | $^{235}$U |
|---|---|---|---|---|
| $^{94}$Sr | 1427.7 | 58.25 | 56.62 | 65.62 |
| $^{132}$Sb | 973.9 | 102.70 | 28.15 | 68.26 |
| $^{94}$Y | 918.7 | 35.95 | 36.04 | 35.69 |
| $^{93}$Sr | 875.9 | 32.01 | 33.18 | 33.82 |
| $^{90}$Rb | 831.7 | 49.71 | 98.58 | 82.92 |
| $^{145}$Ce | 724.3 | 87.22 | 64.31 | 77.62 |
| $^{132}$Sb | 697.4 | 126.02 | 35.41 | 82.26 |
| $^{140}$Cs | 602.3 | 61.29 | 46.61 | 64.38 |
| $^{93}$Sr | 590.2 | 121.07 | 115.96 | 122.81 |
| $^{108}$Rh | 434.2 | 109.09 | 33.00 | 46.17 |
| $^{133}$Te | 407.6 | 57.35 | 77.67 | 63.26 |
| $^{144}$La | 397.4 | 72.51 | 58.24 | 73.37 |
| $^{104}$Tc | 358.0 | 172.92 | 18.06 | 35.11 |

**Table 5.2:** Photopeak Modeling Results for PT-2 Single Elements Case

| Isotope | Photopeak (keV) | $(^{counts}/_{ng})$ $^{239}$Pu | $^{233}$U | $^{235}$U |
|---|---|---|---|---|
| $^{94}$Sr | 1427.7 | 37.96 | 38.90 | 47.46 |
| $^{132}$Sb | 973.9 | 73.07 | 21.12 | 53.66 |
| $^{94}$Y | 918.7 | 25.97 | 27.45 | 28.41 |
| $^{93}$Sr | 875.9 | 23.14 | 25.28 | 26.96 |
| $^{90}$Rb | 831.7 | 35.88 | 75.03 | 66.08 |
| $^{145}$Ce | 724.3 | 63.25 | 49.17 | 62.16 |
| $^{132}$Sb | 697.4 | 91.39 | 27.08 | 65.92 |
| $^{140}$Cs | 602.3 | 43.61 | 34.96 | 50.89 |
| $^{93}$Sr | 590.2 | 87.97 | 88.82 | 98.42 |
| $^{108}$Rh | 434.2 | 77.27 | 24.68 | 36.13 |
| $^{133}$Te | 407.6 | 40.28 | 57.42 | 49.01 |
| $^{144}$La | 397.4 | 49.13 | 41.59 | 55.54 |
| $^{104}$Tc | 358.0 | 120.04 | 13.22 | 26.87 |

Although the fluxes of PT-1 and PT-2 are just over an order of magnitude in difference, the photopeak counts per nanogram were maintained generally within a factor of two between experiments conducted with both systems. This was done by altering the measuring height from 300mm for PT-1 irradiations to 100mm for PT-2 irradiations and increasing the irradiation time slightly (from 20 to 25 seconds). In both Table 5.1 and Table 5.2, certain indicators can be spotted visually. $^{104}$Tc exhibits a strong signature from $^{239}$Pu, while it is considerably weaker from $^{233}$U and $^{235}$U. $^{90}$Rb is quite the opposite, with exhibiting strong signatures from both $^{233}$U and $^{235}$U while showing a relatively weak signature from $^{239}$Pu. Also, of note is the disparity between $^{132}$Sb photopeak yields in $^{233}$U and $^{235}$U irradiations. All of these trends will become useful in creating a robust solution to the overdetermined system of equations, thus providing a fissile sample characterization with low uncertainty.

## 5.2 Fission Product Recoveries

A necessary step in this methodology to compare the fission product photopeak modeling methods against measured data. This is done by conducting calculated over experimental (C/E) comparisons for each fission product photopeak. Figure 5.1 shows C/E values for the average for sample measurements conducted at both PT-1 and PT-2 for $^{239}$Pu, $^{233}$U, and $^{235}$U. Four separate measurements were conducted for each facility, totaling 8 averaged measurements for fission products resulting from irradiation of a fissile isotope. The error bars presented in Figure 5.1 represent the average photopeak area uncertainty calculated from PeakEasy post-processing. Sample masses were prepared within a narrow range in order to minimize the effects of confounding factors to fission product measurement precision. $^{239}$Pu was kept between 30 and 32 ng, $^{233}$U was between 46 and 48 ng, and $^{235}$U was between 40 and 43 ng. Even though the samples were irradiated in different pneumatic tubes for different amounts of time, this was taken account for in developing the theoretical photopeak yields (see Photopeak Modeling Results section). The error bars included on Figure 5.1 are the average photopeak uncertainty experienced between all eight measurements. This helps show the consistency in obtaining peak statistics an also the average peak recovery when compared to theoretically calculated values.

As seen in Figure 5.1, photopeaks generally had less than $\pm$10% uncertainty in counting statistics. As a whole, they were centered around a C/E of 1.0 with a margin of error less than 20%. Since an overdetermined system is to be used in this method, slight deviations of individual fission product photopeaks is less of a concern than an overall trend in the average. It was noticed that $^{233}$U has a slight negative bias for most fission products, which indicates that there may be an issue with the total collapsed fission cross section. This is likely due to either a bias in the neutron flux or the fission cross section. It is hypothesized that a more comprehensive characterization of neutron flux in the epithermal region between 1 and 10 eV to allow

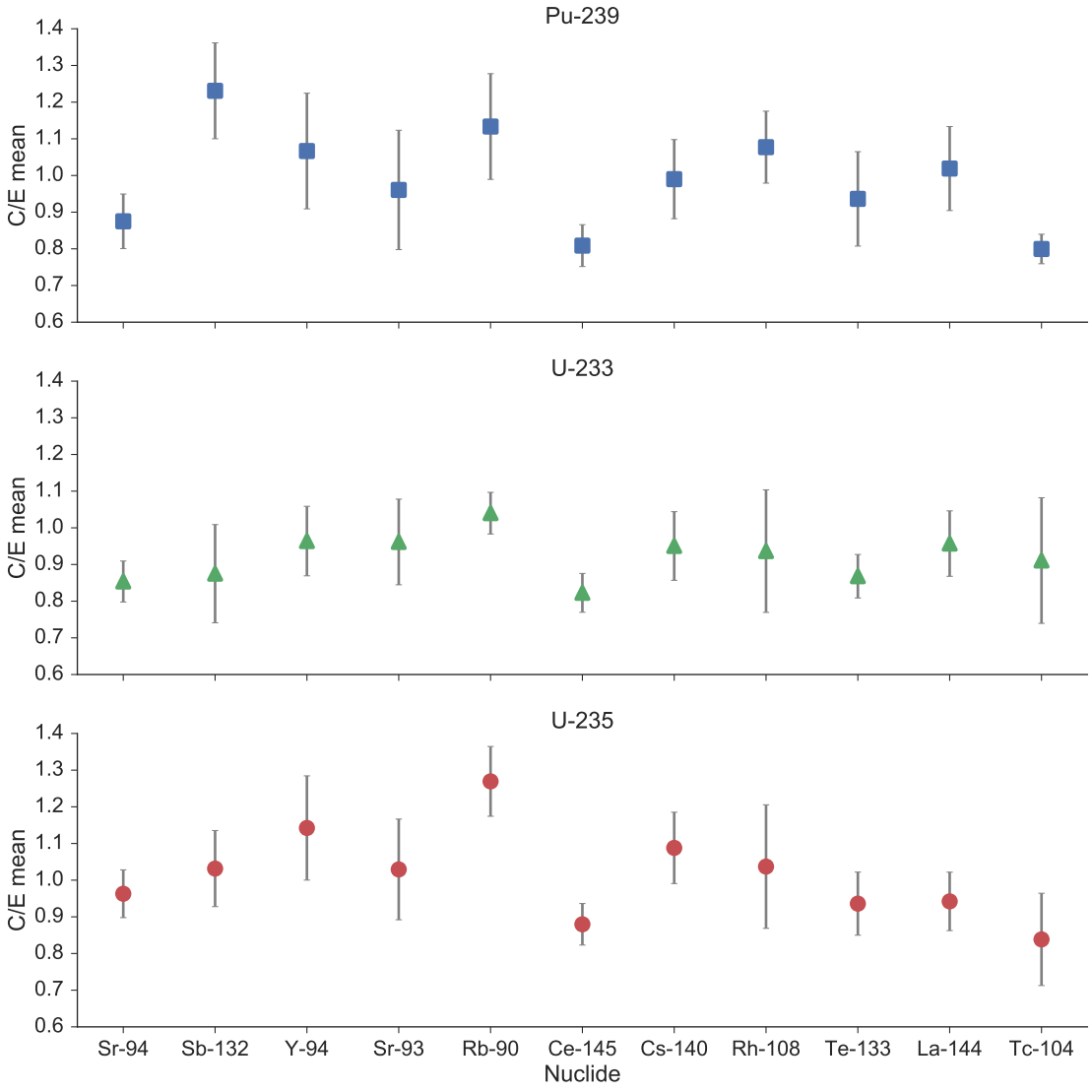



**Figure 5.1:** Fission product photopeak C/E (ORIGEN Calculated divided by Experimentally measured) values and counting uncertainties for 4 separate irradiations in PT-1 and 4 irradiations in PT-2 using corrected spectra

for better approximation of reactions happening with the large resonance integral seen in Figure 3.3.

Figures 5.2, 5.3, and 5.4 show the C/E recoveries for all measurements with box-and-whisker plot diagrams. The center line of each box represents the data median, ends of the box represent 2nd and 3rd quartiles, and the lines extend out to maximum

and minimum points as long as they are within 1.5 times the inner quartile range. Points that are outside these lines can be considered as statistical outliers, but have been kept in each plot in order to maintain data transparency. These plots are useful in showing both the precision and accuracy of this SCALE modeling and simulation scheme for predicting photopeak yields between PT-1 and PT-2 irradiations.

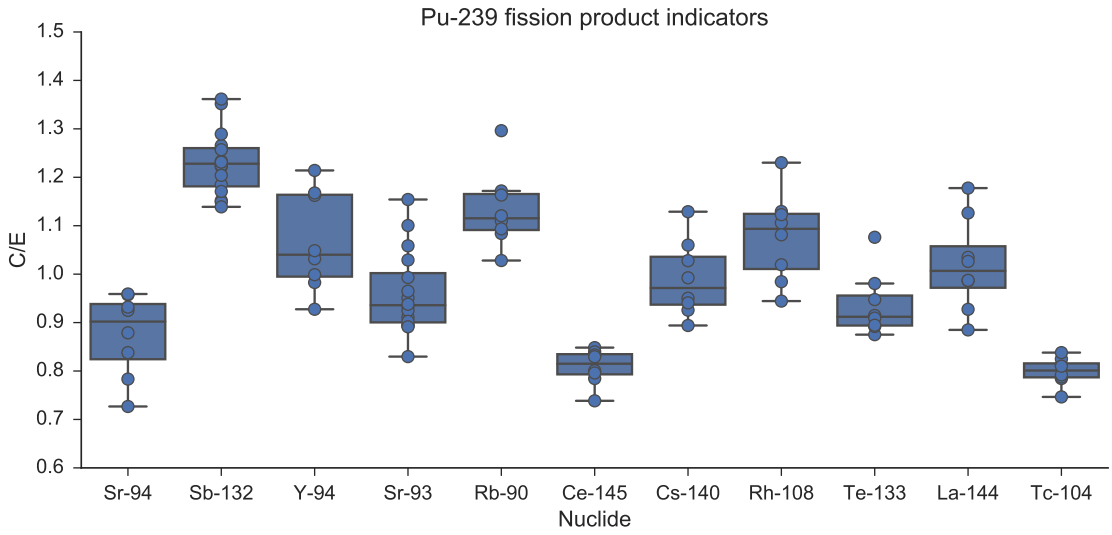



**Figure 5.2:** SCALE predicted photopeak yields divided by the short-lived fission product photopeak measurements from $^{239}$Pu for 4 PT-1 and 4 PT-2 irradiations

Additional insights on the precision of fission product photopeak modeling can be gained from looking at these figures. It was realized that $^{90}$Rb was recovering on the high side for most measurements. This is likely due to the fact that $^{90}$Rb is the beta-delayed decay product of $^{90}$Kr, which is a gas at room temperature. Although samples are kept within a sealed container, there is a possibility for some gas to escape during the irradiation process. In addition, significant inconsistency in the $^{104}$Tc C/E values was noticed for $^{233}$U irradiations. This is potentially due to the fact that there are very few photon emissions from $^{104}$Tc during the measurement period (see $^{104}$Tc photopeak yields in Tables 5.1 and 5.2) and the photopeak is the lowest energy of the evaluated signatures, meaning that it will suffer from spectral effects the most. Additionally, $^{239}$Pu irradiations showed consistent under predictions

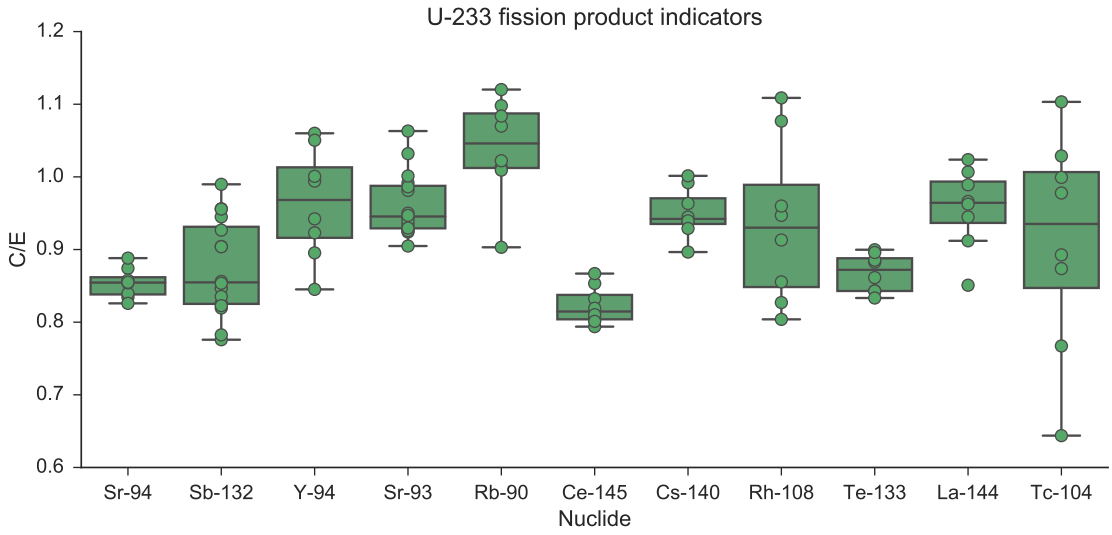



**Figure 5.3:** SCALE predicted photopeak yields divided by the short-lived fission product photopeak measurements from $^{233}$U for 4 PT-1 and 4 PT-2 irradiations

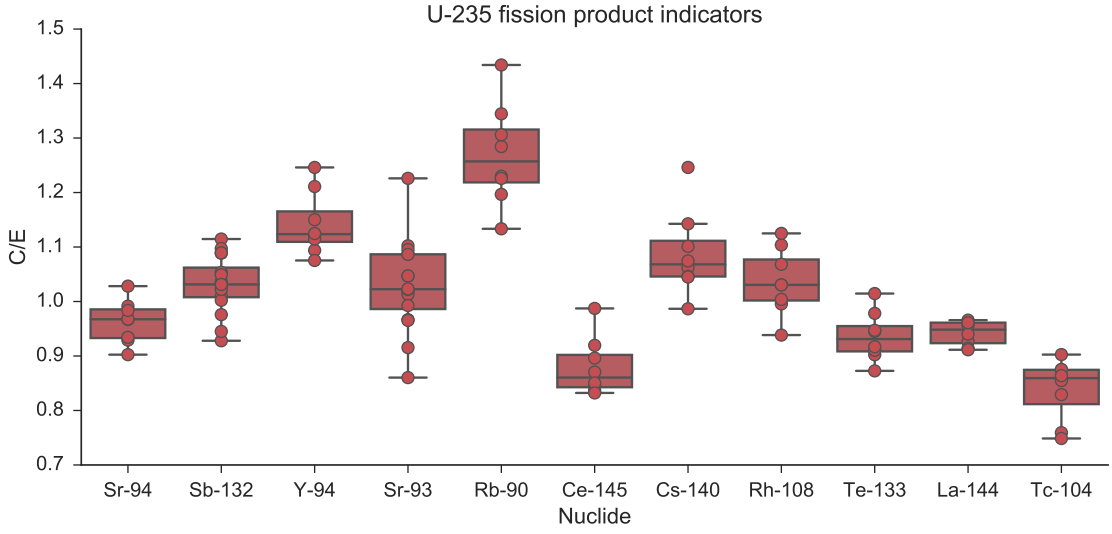



**Figure 5.4:** SCALE predicted photopeak yields divided by the short-lived fission product photopeak measurements from $^{235}$U for 4 PT-1 and 4 PT-2 irradiations

of $^{104}$Tc compared to what was measured in the lab. Even though $^{104}$Tc had high precision, its C/E was consistently around 80% . This gives a strong indication that the accumulated fission yield may be in error for $^{239}$Pu fission into $^{104}$Tc. Also $^{145}$Ce has consistently low C/E values across all nuclides. Since $^{145}$Ce has relatively low peak

uncertainty in Figure 5.1 and high measurement precision in Figures 5.2, 5.3, and 5.4, it may indicate that the fission product branching ratio with all fissile nuclides may be in error.

In order to gain insight on the accuracy of fission product yield data, a table of uncertainties from ENDF/B-VII.1 is listed in Table 5.3. As can be seen by this table, there is very little consistency in the uncertainties for these yields. $^{233}$U has considerably higher uncertainties for almost all fission product yields, with $^{239}$Pu and $^{235}$U containing less uncertainty for most of the listed fission products. This may explain the biases seen uniquely in $^{233}$U. Although these experiments show some of the most accurate short-lived fission product recoveries to be published, improvements in nuclear data could could bring additional accuracy to these methods.

**Table 5.3:** Table of Fission Product Yield Uncertainties from ENDF/B-VII.1 for Energy=0.0253 eV [3]

| Isotope | Thermal Cumulative Fission Yield Uncertainty (%) | | |
|---|---|---|---|
| | $^{239}$Pu | $^{233}$U | $^{235}$U |
| $^{94}$Sr | 4.0 | 32 | 1.4 |
| $^{132}$Sb | 8.0 | 64 | 6.0 |
| $^{94}$Y | 2.0 | 32 | 1.0 |
| $^{93}$Sr | 2.8 | 32 | 1.0 |
| $^{90}$Rb | 16 | 11 | 1.4 |
| $^{145}$Ce | 1.4 | 4.0 | 6.0 |
| $^{140}$Cs | 8.0 | 16 | 1.4 |
| $^{108}$Rh | 8.0 | 6.0 | 6.0 |
| $^{133}$Te | 6.0 | 23 | 2.8 |
| $^{144}$La | 8.0 | 4.0 | 1.4 |
| $^{104}$Tc | 6.0 | 64 | 2.0 |

## 5.3 System of Equations for Single Element Samples

Using the modeled fission product photopeak yields (Tables 5.1 and 5.2), the overdetermined system of equations (Equation 3.3) can easily be constructed for a single isotope. Figure 5.5 shows the C/E recovery results for fissile isotope samples of $^{239}$Pu, $^{233}$U, and $^{235}$U along with calculated $^{238}$U. $^{238}$U mass was calculated simply by dividing the efficiency corrected theoretical photopeak counts per nanogram by the measured photopeak area. Both PT-1 and PT-2 irradiations are shown in this figure in addition to PT-2 data points for the MCNP calculated uncorrected spectrum. This data uses the 238-group flux prior to the STAYSL-PNNL correction. Error bars indicated on Figure 5.5 represent the uncertainty at one standard deviation calculated by Equation 3.11.

Through developing this overdetermined system, highly accurate fissile sample characterizations could be made with corrected values within 10% of their true value. A major improvement between the PT-2 uncorrected spectrum and the PT-2 corrected and PT-1 spectra can be seen in all evaluated nuclides. The observed 20% improvement towards a C/E of nearly 1.0 occurred when using SCALE data from the corrected PT-2 spectrum. This was expected because of the 20% biases seen in prior flux monitor measurements (Table 3.1). These results give strong evidence towards an effective flux characterization on PT-2. One interesting trend that was noticed is the consistent replicability of small measurement biases between the two different neutron spectra (PT-1 and PT-2) and experimental conditions. This is likely due to the small uncertainties experienced in the measured fissile mass in each sample, and is an indicator of the high sensitivity of methods presented here. These uncertainties are in the ranges of 0.8-0.9% for $^{239}$Pu, 3.2-3.4% for $^{233}$U, and 3.4-3.5% for $^{235}$U and $^{238}$U.

Figure 5.6 shows box and whisker plots for these same single-element measurements for all four nuclides. For these plots, the uncorrected data was removed. This spread shows that the single-isotope quantifications were highly precise, and

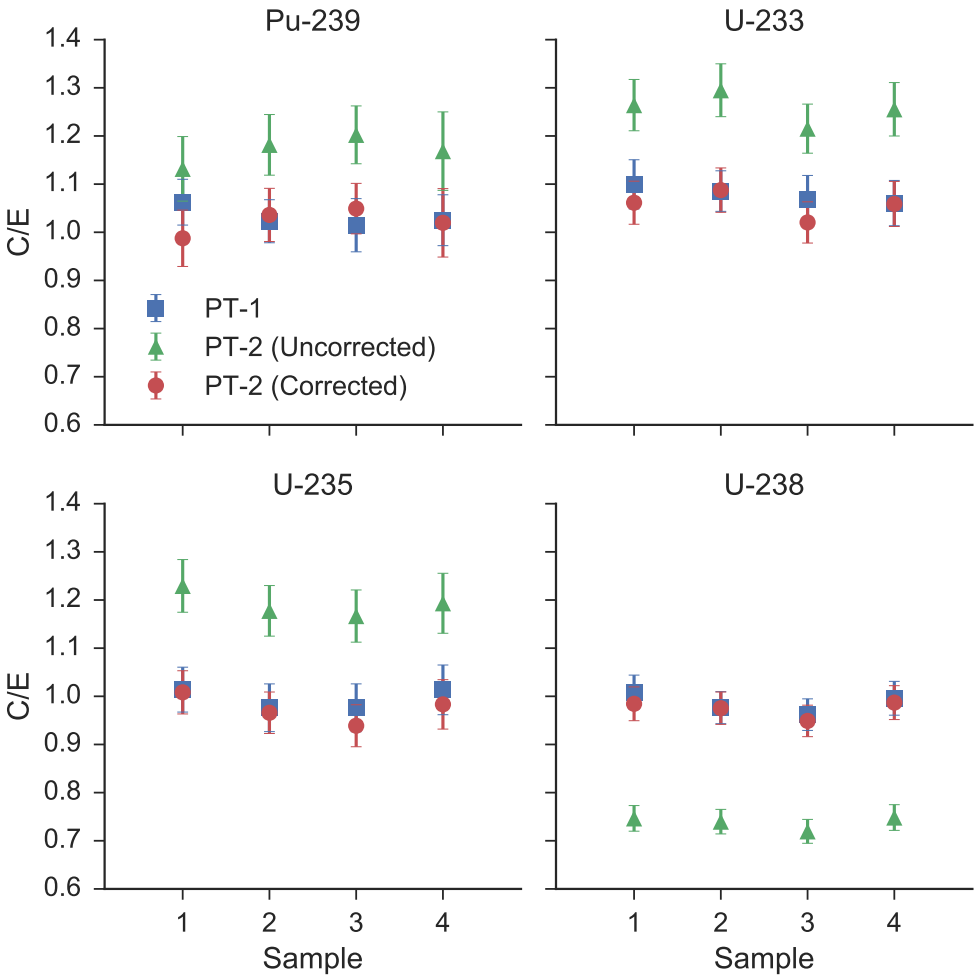



**Figure 5.5:** PT-1, PT-2 corrected, and PT-2 uncorrected calculated over certified values for nanogram quanitites of nuclides from single element irradiations of natural uranium, high-purity $^{233}$U, and plutonium solutions

accurate within 10% of the certified values. The lack of an overdetermined system for $^{238}$U quantification (due to using only one photopeak to make a quantification) is a main reason for its low variability in C/E determination. Although slightly larger than $^{238}$U, the three fissile isotopes analyzed showed high precision between two different interrogating neutron spectra. This displays the effectiveness of generating appropriate gamma sources through the SCALE modeling and simulation methods. Similarly to Figure 5.5, the C/E values for $^{233}$U was observed to be consistently

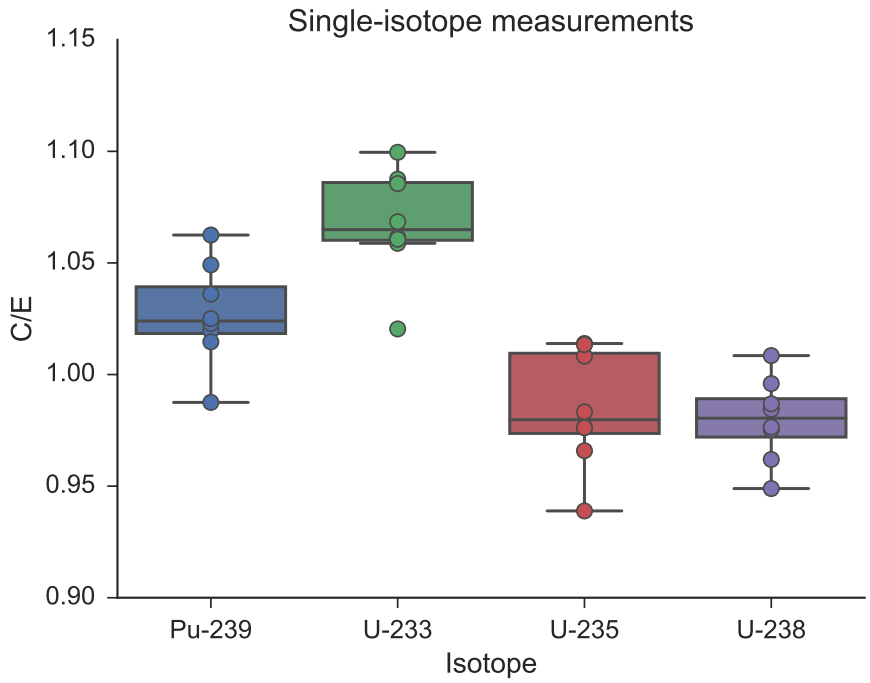



**Figure 5.6:** Box and whisker plots showing the spread of PT-1 and PT-2 corrected C/E values

biased higher than the other nuclides shown in Figure 5.6. This bias is likely due to the 238-group collapse's effect on $^{233}$U fission rate, which could be corrected through an adjustment in the cross section data or a more detailed flux characterization of the 1-10 eV neutron energies. This effect was discussed previously in the Fission Product Recoveries section.

Another phenomena that has been noticed in these measurements is the tendancy for $^{238}$U C/E values to recover lower than 1.0. This indicates that SCALE modeling is consistently under-predicting the amount of gamma-rays that are received by the detector during acquisition. This effect has been seen in the past at the NAA laboratory because of the $K_\alpha$ gamma-rays that are emitted from lead that is being bombarded by higher energy gamma rays during measurement. These gamma rays are emitted at an energy of 72.8 and 74.9 keV, the second of which can pile up underneath the very large 74.7 keV photopeak from $^{239}$U. Even though a graded shield was used

in all of these experiments, some $K_\alpha$ gamma-rays are expected because of the high gamma energies and count rates experienced from short-lived fission products.

## 5.4 Binary Mixtures

To take this analysis a step further, binary mixtures were prepared and analyzed using the same overdetermined system of equations as before with the single element samples. These samples were prepared by aliquoting quantities of two solutions from Table 4.7 and evaporating the solution in a single polyethelene insert using a drying oven. Figure 5.7 shows the results from running the overdetermined system of equations for these binary samples after irradiation in PT-2 and using the experimental procedure described in Table 4.8. The mixtures contained varying amount of fissile mass and mixtures of $^{233}$U in $^{235}$U and $^{239}$Pu in $^{235}$U. The total fissile mass and fissile ratios are listed Table 5.4.

**Table 5.4:** Sample Details for Binary Mixtures

| Sample Identifier | Total Fissile Mass (ng) | $^{239}Pu/^{235}U$ | $^{233}U/^{235}U$ |
|---|---|---|---|
| J22 | 85.28 | 0.52 | – |
| J26 | 81.72 | 1.03 | – |
| J11 | 104.41 | – | 1.50 |
| J14 | 88.49 | – | 0.98 |

Figure 5.7 shows high accuracy in characterizing $^{239}$Pu, $^{233}$U, $^{235}$U, and $^{238}$U, yielding the correct results within a 10% bias. It was noted that $^{233}$U possessed the largest uncertainty, which was likely due to the large variability in fission product C/E results seen the fission product box and whisker plots (Figure 5.3). This set of experiments was then repeated with the same fissile mixture samples in the PT-1 spectrum. With over a magnitude of difference in flux in addition to the lower thermal

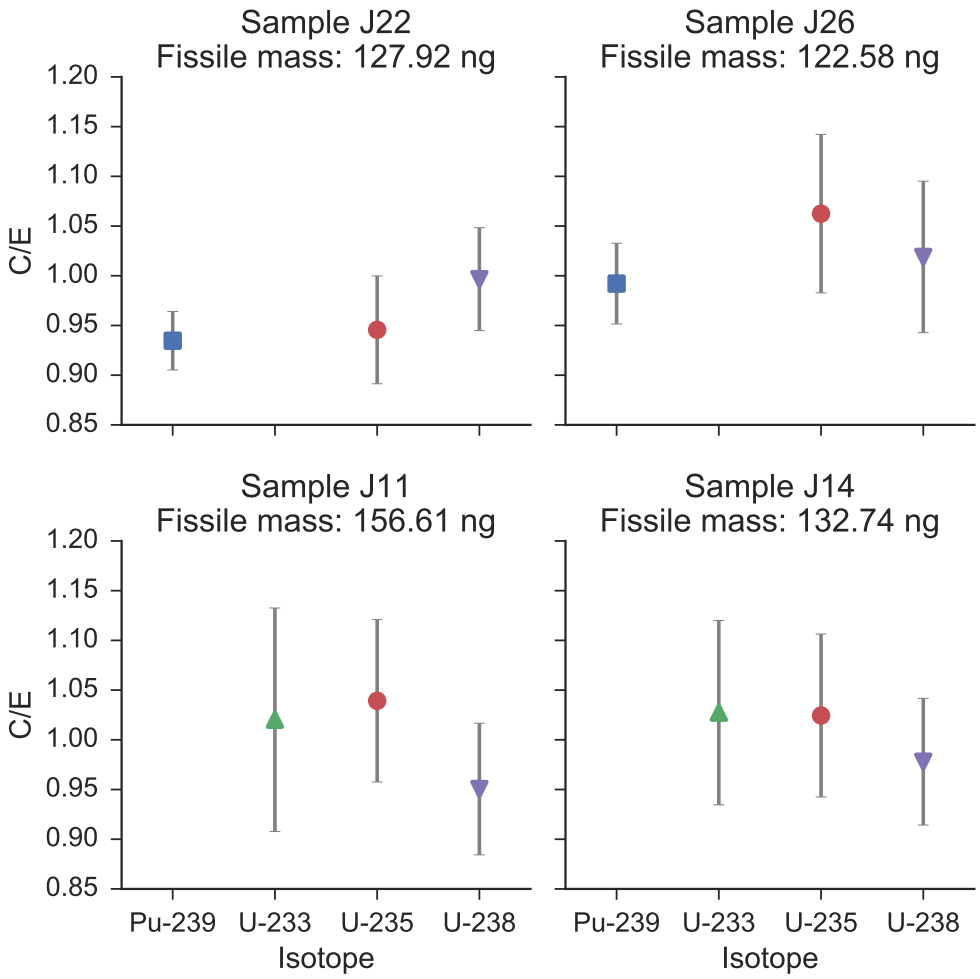



**Figure 5.7:** Calculated over certified mass assay results for fissile mixtures irradiated in PT-2

to epithermal ratio experienced in PT-1, this was a true test of the capabilities of this generalized overdetermined system. Figure 5.8 shows that this method exhibited high accuracy for each sample, and provided results within a 10% bias.

The uncertainties for these binary fissile mixture experiments are considerably higher than the singe fissile isotope assays, but have little loss in accuracy. This is likely due to a larger contribution of residuals from the linear fit. Rather than having to establish a fit that satisfies one nuclide, the binary mixture has to satisfy two; almost always making residuals larger. According to Equation 3.11 this uncertainty

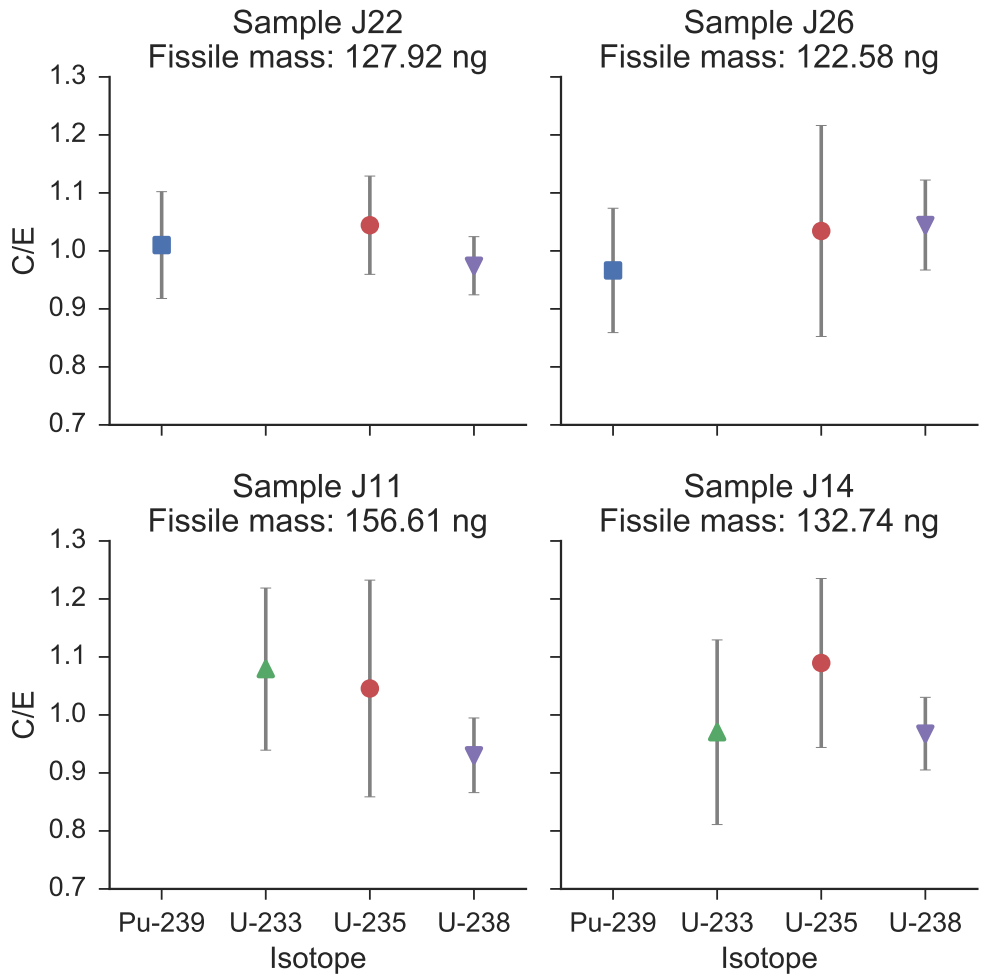



**Figure 5.8:** Calculated over certified mass assay results for fissile mixtures irradiated in PT-1

at one sigma could be alleviated by obtaining a larger number of reliably modeled signatures. The C/E results between PT-1 and PT-2 irradiations do have variability in their characterizations, but are well within the measurement uncertainty. This indicates that will a slightly less overdetermined system, there can have some small variability in the assay results if conducted over multiple trials.

By conducting experiments with binary mixtures containing three different fissile nuclides, this work has shown the advantage of applying an overdetermined system of short-lived fission products. The C/E values for fissile mixtures were within 10%

of their true value, with uncertainties less that 15%. This was also demonstrated for different fissile ratios, and expected to be applicable over a wide range of concentrations. It is hypothesized that by adding additional short-lived fission product isotope photopeaks to this analysis, uncertainties can be lowered and additional nuclides could be evaluated.

## 5.5 Matrices of Safeguards Interest

Another level of complexity was added by evaluating fissile material in matrices of safeguards interest. The IAEA J-Swipe and TeX Swipe were used for this next set of experiments. Both of the swipe versions are cellulosic swipes actively used in typical IAEA nuclear facility inspection processes. The HFIR-NAA facility has considerable experience in measuring trace uranium on IAEA J-Swipes using delayed neutron activation analysis methods [39]. One of the challenges expected to be encountered in these measurements is the activation products present in the irradiated swipe. Therefore, a short irradiation and gamma spectroscopy measurement for each swipe matrix was conducted in order to identify ingrowth of gamma lines that are not present in the short-lived fission product spectrum. The activation products $^{24}$Na, $^{49}$Ca, and $^{108}$Ag were found with the J-swipe and $^{24}$Na, $^{49}$Ca, and $^{27}$Mg were found for the TeX swipe. Additionally, to mimic what is already done with delayed neutron methods at the HFIR-NAA facility, the samples were measured in-rabbit. This added additional complexity since activation products were created from within the polyethylene rabbit and radioactive contamination from the pneumatic tube was present on the rabbit's outer walls. The activation products identified after an empty rabbit irradiation in PT-2 were: $^{56}$Mn, $^{28}$Al, $^{38}$Cl, $^{41}$Ar, and $^{51}$Cr. It is known that the $^{56}$Mn, $^{28}$Al, and $^{38}$Cl are activation products made from within the high-density polyethylene (HDP) matrix, while $^{41}$Ar is created from activation of elemental Argon in air, and $^{51}$Cr is created from activated Chromium acquired from the stainless steel pneumatic tube. As can be seen in Table 5.5, the major photopeaks of these activation product do not

give interferences to the short-lived fission product photopeaks used in this analysis. The high energies of these fission products does cause a significant Compton shelf in the gamma spectrum, and does raise the baseline for an increase in detection limits. This effect is investigated further in the Detection Limits section.

**Table 5.5:** IAEA Swipe Activation Products

| Isotope | Origin | Half-Life | Major Photopeaks (keV) |
|---|---|---|---|
| $^{24}$Na | IAEA J-Swipe/TeX Swipe | 14 h | 1368, 2754 |
| $^{49}$Ca | IAEA J-Swipe/TeX Swipe | 8.7 m | 3084 |
| $^{108}$Ag | IAEA J-Swipe | 2.4 m | 633.0 |
| $^{27}$Mg | IAEA TeX Swipe | 9.5 m | 843.8, 1014 |
| $^{28}$Al | HDP Rabbit | 2.2 m | 1779 |
| $^{56}$Mn | HDP Rabbit | 2.6 h | 846.8 |
| $^{41}$Ar | Air inside Rabbit | 110 m | 1294 |
| $^{51}$Cr | Activated Cr in Steel PT | 27.7 d | 320.1 |

The IAEA swipes were tightly folded and placed inside of the polyethylene rabbit with $\mu L$ quantities of natural and depleted uranium solution (from Table 4.7) pipetted onto each swipe. These samples were then placed in a drying oven before being heat sealed shut within the rabbit using a soldering iron. $^{235}$U enrichments are listed in Table 5.6 and sample masses are indicated in Figure 5.9. These samples were irradiated for 60 seconds each, given 120 seconds of decay, and measured for 360 seconds at 300mm above the detector endcap. After irradiation, measurement, and post-processing using PeakEasy, the $^{235}$U short-lived fission product photopeak areas were entered into the system of equations after SCALE modeling developed the photopeak yield factors. Figure 5.9 shows the recoveries for $^{235}$U and $^{238}$U in each sample, with uncertainty calculated to one standard deviation using Equation 3.11.

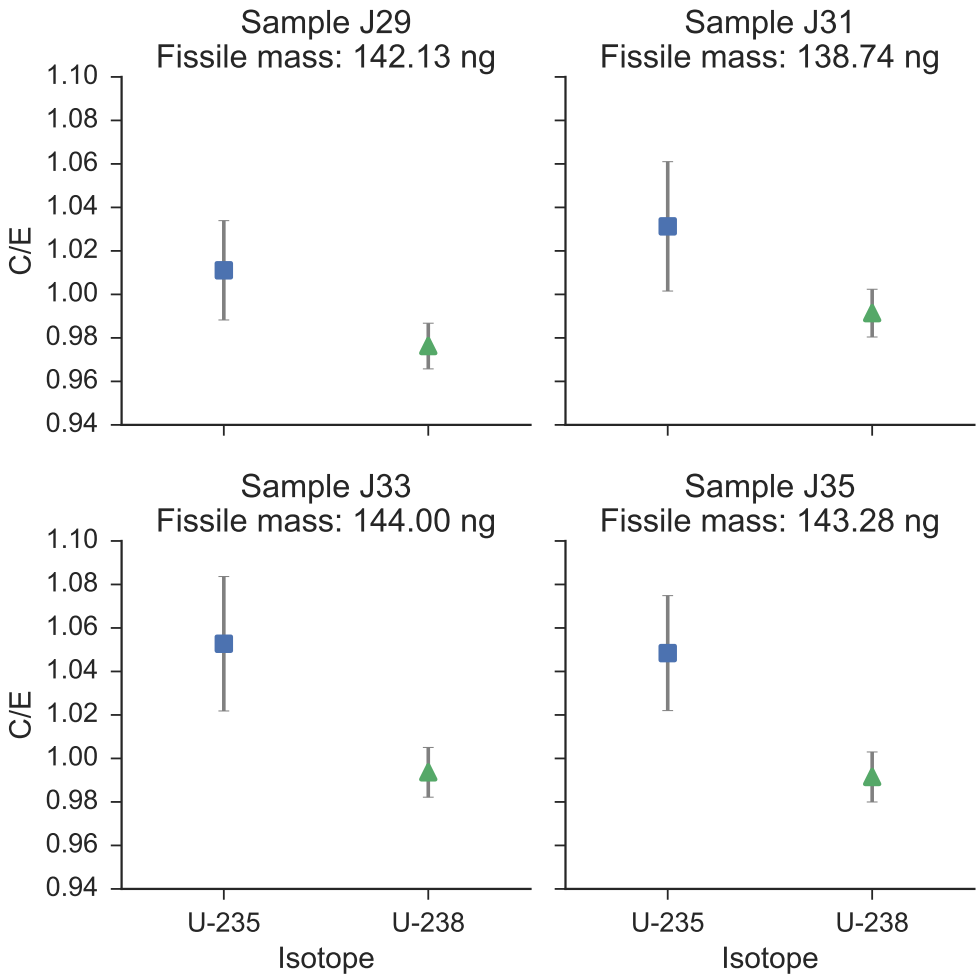



**Figure 5.9:** C/E Recoveries for Uranium on IAEA Swipes

Table 5.6 shows the $^{235}$U enrichment results to greater detail. These listed results gives great confidence in this method being able to perform well with an activated matrix. This method performed to exceptional accuracy with identifying $^{235}$U concentration within 5% error. It is anticipated that matrices with increasing complexity could be measured in this manner, and is a subject of interest in future work. Additionally, a larger range of uranium enrichments could be measured in order to find the accuracy of response for higher enriched uranium.

**Table 5.6:** IAEA Swipe Sample Measurement Details

| Sample Identifier | Swipe Material | Certified Uranium Enrichment | Calculated Uranium Enrichment | Uncertainty |
|---|---|---|---|---|
| J29 | J-Swipe | 0.341% | 0.352% | 2.0% |
| J31 | TeX Swipe | 0.341% | 0.354% | 2.7% |
| J33 | J-Swipe | 0.725% | 0.768% | 2.8% |
| J35 | TeX Swipe | 0.725% | 0.767% | 2.4% |

## 5.6 Detection Limits

In addition to these series of measurements, detection limits were evaluated with the previously described irradiation and measurement conditions (Table 4.8) using the Currie detection limit equation. This equation, when applied to gamma-ray spectrometry, identifies the 95% confidence limit for photopeak detection above the continuum counts ($N_B$) by considering emission intensity ($\gamma_i$), detector efficiency ($\epsilon$), and measurement time ($t_m$) [40]. $N_B$ was determined from the continuum achieved by separate irradiations of similarly massive $^{235}$U and $^{239}$Pu samples. This detection limit is referred to as the Minimum Detectable Activity (MDA) and was determined using Equation 5.1.

$$MDA = \frac{4.65\sqrt{N_B} + 2.71}{t_m \gamma_i \epsilon} \tag{5.1}$$

From this MDA, the collapsed one-group fission cross section multiplied by accumulated fission yield ($\sigma_f \gamma_{fy}$) was used with irradiation and measurement conditions to find the mass of target material required to produce the MDA. Incorporating Avogadro's number ($N_A$) and atomic mass of the target nuclide ($M_A$) will cause Equation 5.2 to result in a minimum target mass for fission product

detection ($L_T$) in nanograms.

$$L_T = \frac{MDA}{\phi\sigma e^{-\lambda t_d}(1 - e^{-\lambda t_{irr}})N_A M_A 10^9} \tag{5.2}$$

It was soon found that irradiation time, measurement height, and decay time had large effect on these simulated detection limits. Therefore, a limitation of 60 seconds of irradiation, 30mm of measurement height, and 120 seconds of decay was placed on the measurements. A comparison between the PT-1 samples irradiated for a shorter amount of time and measured at 300mm and the PT-2 irradiated IAEA swipes measured at 30mm can be seen in Figure 5.10. Based on these optimized irradiation and measurement conditions experienced in the single fissile isotope characterization for the IAEA J-swipe, detection limits for most analyzed fission product isotopes were found to be less than 1 nanogram. This indicates that fissile sample quantifications could be made at sub-nanogram levels without making significant changes to the described fissile sample characterization processes.

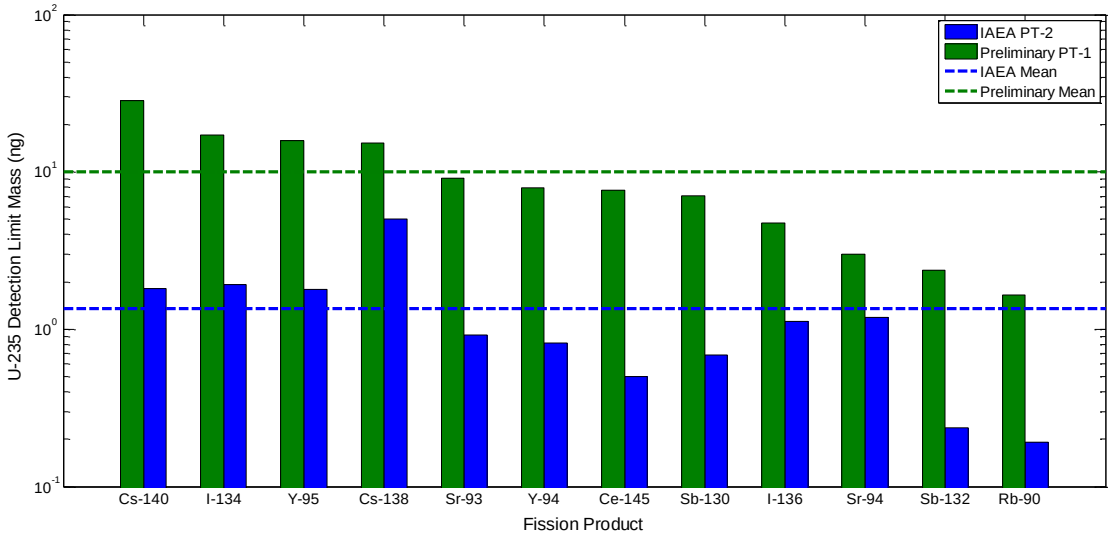



**Figure 5.10:** Detection Limits for $^{235}$U Fission Products

# Chapter 6

# Conclusions

## 6.1 Research Outcomes

This research has shown several successful fissile sample characterizations using a methodology that is generalizable to variations in the interrogating neutron spectrum and a sample's fissile composition. This has been accomplished by incorporating modern modeling and simulation tools such as SCALE and STAYSL-PNNL with a multivariate analysis of several fission product photopeaks, ultimately creating an overdetermined system of equations. An unparalleled accuracy of short-lived fission product photopeak yield predictions was possible using a thorough flux characterization, COUPLE 238-group cross section collapse, and ORIGEN's transmutation and gamma decay source output. The benchmarking comparison between Tables 2.2 and 2.3 and Tables 4.2 and 4.3 illustrate this significant improvement in accuracy. These photopeak simulations were used with measurements conducted with an HPGe detector and digital MCA operated in dual loss-free counting to obtain a true dead-time corrected spectrum. Once this overdetermined system was developed, solving for fissile constituents was relatively simple. The unique capabilities of the HFIR-NAA facility has enabled these measurements to reach fissile

mass detection limits never seen before in non-destructive analysis measurements (see Tables 1.1 and 2.1).

The speed, accuracy, and low detection limits of this method illustrate its applicability to the safeguards and nuclear forensics technical communities. This methodology could potentially reduce the time needed to conduct safeguards and nuclear forensics measurement for samples containing special nuclear materials. In addition, the high signal-to-noise ratio provides a non-destructive measurement method that can be less dependent on matrix interferences from the sample matrix or background than current state of the art.

The generalizability of this method gives great promise towards its implementation at other reactor-based irradiation facilities. STAYSL-PNNL is a powerful tool for characterizing an irradiation facility's neutron spectrum, and can provide an output applicable to COUPLE cross-section generation. Additionally, these methods are generalizable to assay other fissile materials. With the necessary computational tools in place, accurate photopeak yields for other fissile materials interrogated in a neutron beam can be calculated and used to characterize samples.

## 6.2 Lessons Learned

Short-lived fission product measurements are both a challenge to measure and to model. Therefore, a significant portion of this effort went into creating highly reliable models of fission product photopeak yields. It was found early on that prior work on short-lived fission product gamma spectroscopy had typically used a simplistic view of a fission cross sections by not conducting a weighted spectrum collapse. Since significant errors were present in these research efforts, a full 238-group spectrum collapse (using COUPLE from the SCALE modeling and simulation suite) was established. This method used an MCNP model output for each pneumatic tube irradiation position in HFIR. This approach was very effective at producing accurate photopeak yields for PT-1, which was used to benchmark against other short-lived

fission product spectroscopy methods. Although the MCNP modeled spectrum was satisfactory for PT-1, additional flux characterization efforts had to be undertaken for PT-2.

When routine PT-2 flux monitor measurements were compared with SCALE model outputs, there was approximately a 20% difference in the modeled activation rates and what was actually measured in the lab. This gave significant doubts in the accuracy of the PT-2 MCNP model. It was soon realized that an experimental characterization had to be conducted if fissile sample characterizations were to be completed in the PT-2 NAA facility. This flux characterization utilized several monitors that possessed thermal, epithermal, and fast neutron reactions that could be quantified through gamma spectroscopy. By covering these monitors in cadmium, a better sampling of the epithermal and fast neutron energies (>0.5 eV) was made. This flux characterization not only gave great improvements in the daily flux monitor activation modeling, but also for the irradiation of fissile isotopes evaluated in this method.

Another lesson learned in this research was regarding the appropriate methods for collecting gamma-ray spectroscopy data for short-lived fission products. Having a high-resolution HPGe with digital MCA and over 10,000 bins was certainly needed, but accounting for rapidly decaying and ingrowth of some nuclides had to be accounted for with specialized software. Traditional neutron activation analysis uses simple linear dead-time corrections to account for the electronic lag caused high count rate samples. Since short-lived fission products have very high activities, decay in short periods of time, and can have ingrowth of some isotopes, an accurate representation of the fission product activities must be calculated using real-time dead-time corrections. This is done through the Canberra Lynx MCA through a mode called Dual Loss-Free Counting. This method was discussed in the Background section, and shown by other researchers to be accurate at characterizing radioactive nuclide activities at dead-times as high as 80% [23].

## 6.3 Opportunities for Future Work

In order to further prove the generalizability of this method, there are several other experiments that could be conducted. Although two different irradiation positions were used in HFIR, their spectra shapes are somewhat similar (see Figure 2.7). It would be a logical step to move these experiments to a more hardened spectrum within HFIR, possibly within the flux-trap region (Figure 2.6). Additionally, characterizing the flux spectra at other reactor-based facilities could lead to developing this same fissile sample characterization method for other neutron spectrum shapes. Lastly, testing these methods in a non-reactor neutron spectrum could potentially open pathways for developing this technique in a more portable manner. These non-reactor based sources could be $^{252}$Cf or Deuterium-Tritium (DT) fusion based generators.

One potential area of further investigation is the bias that was observed in the $^{233}$U fission product modeling. For nearly all fission products evaluated in this work, the photopeak yields were modeled consistently smaller than their measured counterparts (see Figure 5.6). This was hypothesized to be an effect created from the total $^{233}$U cross-section collapse. This collapse could be altered because of an error in the 238-group cross section or the continuous fission cross section of $^{233}$U obtained from nuclear data. Further characterization of the HFIR-NAA laboratory's pneumatic tube spectra would have to be conducted in order to narrow down the cause of this discrepancy. If this bias were to be corrected, there is a possibility for more accurate fissile isotope characterizations to be made.

Another opporutnity for future work could be to study the sensitivity of irradiation, decay, and detector acquisition time on the accuracy of a fissile sample characterization. There may be more methods to optimize detection limits, or guard against high dead-times. Additionally, there may be more fission product indicators at longer decay intervals. The methods developed in this work were to optimize a full characterization scheme taking less than 10 min, but additional time could gain some accuracy.

Due to sample handling requirements, there was no capability to characterize samples with less than two minutes of decay, although alterations to the currently installed measurement system are currently being made to reduce this decay period and allow for more signatures to be collected. Additionally, the coupling of Delayed Neutron Activation Analysis (DNAA) as an orthogonal total fissile mass measurement could be investigated. It is anticipated that this form of nondestructive fissile mass characterization will be of interest for nuclear forensics and safeguards measurements containing trace amounts of fissile material. To serve a broader application and display further generalizability of this method, more complex sample matrices and additional fissile nuclides are being looked into for further experimentation.

# Bibliography

[1] D. Beddingfield and F. Cecil, "Identification of fissile materials from fission product gamma-ray spectra," *Nuclear Instruments and Methods in Physics Research Section A: Accelerators, Spectrometers, Detectors and Associated Equipment*, vol. 417, no. 2-3, pp. 405–412, 1998. x, xii, 4, 8, 9, 11, 13, 14, 37

[2] M. Andrews, J. Goorley, E. Corcoran, and D. Kelly, "MCNP6 simulations of gamma line emissions from fission products and their comparisons to plutonium and uranium measurements," *Progress in Nuclear Energy*, vol. 79, pp. 87–95, 2015. x, 4, 11, 15, 36, 38

[3] M. Chadwick, M. Herman, P. Obložinský, M. Dunn, Y. Danon, A. Kahler, D. Smith, B. Pritychenko, G. Arbanas, R. Arcilla, R. Brewer, D. Brown, R. Capote, A. Carlson, Y. Cho, H. Derrien, K. Guber, G. Hale, S. Hoblit, S. Holloway, T. Johnson, T. Kawano, B. Kiedrowski, H. Kim, S. Kunieda, N. Larson, L. Leal, J. Lestone, R. Little, E. McCutchan, R. MacFarlane, M. MacInnes, C. Mattoon, R. McKnight, S. Mughabghab, G. Nobre, G. Palmiotti, A. Palumbo, M. Pigni, V. Pronyaev, R. Sayer, A. Sonzogni, N. Summers, P. Talou, I. Thompson, A. Trkov, R. Vogt, S. van der Marck, A. Wallner, M. White, D. Wiarda, and P. Young, "ENDF/B-VII.1 Nuclear Data for Science and Technology: Cross Sections, Covariances, Fission Product Yields and Decay Data," *Nuclear Data Sheets*, vol. 112, no. 12, pp. 2887–2996, 2011. x, xii, xiii, 5, 6, 23, 25, 39, 55

[4] J. R. Lamarsh and A. J. Baratta, *Introduction to Nuclear Engineering*, 1955, vol. 23, no. 1. xii, 5, 7

[5] M. Wiernik, "Comparison of several methods proposed for correction of dead-time losses in the gamma-ray spectrometry of very short-lived nuclides," *Nuclear Instruments and Methods*, vol. 95, no. 1, pp. 13–18, 1971. xii, 10

[6] Oak Ridge National Laboratory, "In-Vessel Irradiation Experiment Facilities at HFIR," Tech. Rep. [Online]. Available: https://neutrons.ornl.gov/hfir/in-vessel-irradiation xii, 16

[7] G. Ilas, D. Chandler, B. Ade, E. Sunny, B. Betzler, and D. Pinkston, "Modeling and Simulations for the High Flux Isotope Reactor Cycle 400," Oak Ridge National Laboratory, Tech. Rep., 2015. xii, 17, 23

[8] J. N. Cooley, W. Bush, I. Tsvetkov, D. Hurt, N. Whiting, M. Burmester, and D. Langlands, "Model Safeguards Approach and Innovative Tecniques Implemented by the IAEA at Gas Centrifuge Enrichment Plants," in *Institute of Nuclear Materials Management 47th Annual Meeting*, 2006, pp. 1–8. 2

[9] K. Sylvester, J. Pilat, and T. Burr, "Evaluating International Safeguards Systems," in *Nuclear Safeguards, Security and Nonproliferation*, 2008, ch. 7, pp. 135–150. 2

[10] J. E. Stewart and G. W. Eccleston, "Passive/Active Neutron Coincidence counter," Los Alamos National Laboratory, Tech. Rep., 1993. 3

[11] T. E. Sampson and J. L. Parker, "Applications of gamma-ray spectrometry in the quantitative nondestructive assay of special nuclear materials," *Nuclear Instruments and Methods in Physics Research Section A: Accelerators, Spectrometers, Detectors and Associated Equipment*, vol. 299, no. 1-3, pp. 327–334, 1990. 3, 11

[12] ASTM, "Standard Test Method for Nondestructive Assay of Nuclear Material in Scrap and Waste by Passive-Active Neutron Counting Using a 252 Cf Shuffler," *ASTM International*, vol. C1316-08, pp. 1–22, 2001. 3

[13] M. Zendel, D. L. Donohue, E. Kuhn, S. Deron, and T. Biro, *Handbook of Nuclear Chemistry*, A. Vértes, S. Nagy, Z. Klencsár, R. G. Lovas, and F. Rösch, Eds. Boston, MA: Springer US, 2011, vol. 77, no. 1–2. 3

[14] H. Xiandeng and B. T. Jones, *Inductively Coupled Plasma/Optical Emission Spectrometry*, 2000. 3, 4

[15] K. J. Moody, I. D. Hutcheon, and P. M. Grant, *Nuclear Forensic Analysis*. Boca Raton, FL: Taylor & Francis Group, 2005. 3, 4

[16] R. Marrs, E. Norman, J. Burke, R. Macri, H. Shugart, E. Browne, and A. Smith, "Fission-product gamma-ray line pairs sensitive to fissile material and neutron energy," *Nuclear Instruments and Methods in Physics Research Section A: Accelerators, Spectrometers, Detectors and Associated Equipment*, vol. 592, no. 3, pp. 463–471, 2008. 4, 11, 12

[17] G. Knoll, *Radiation detection and measurement*, 2005. 6, 9, 10

[18] I. C. Gauld, G. Radulescu, G. Ilas, B. D. Murphy, M. L. Williams, and D. Wiarda, "Isotopic Depletion and Decay Methods and Analysis Capabilities in Scale," *Nuclear Technology*, vol. 174, pp. 169–195, 2011. 7, 20

[19] S. E. Skutnik and D. R. Davis, "Characterization of the non-uniqueness of used nuclear fuel burnup signatures through a Mesh-Adaptive Direct Search," *Nuclear Instruments and Methods in Physics Research, Section A: Accelerators, Spectrometers, Detectors and Associated Equipment*, vol. 817, pp. 7–18, 2016. 8

[20] J. Cheatham and J. Wagner, "Review and Ranking of NDA Techniques To Determine Plutonium Content in Spent Fuel," in *INMM 51st Annual Meeting, Baltimore, MD, USA*, 2010, pp. 1–9. 8

[21] T. Gozani, "Active Nondestructive Assay of Nuclear Materials," *Nureg*, vol. CR–0602, p. 417, 1981. 8

[22] E. J. Cohen, "Live time and pile-up correction for multichannel analyzer spectra," *Nuclear Instruments and Methods*, vol. 121, no. 1, pp. 25–32, 1974. 10

[23] M. Blaauw, R. F. Fleming, and R. Keyser, "Digital signal processing and zero-dead-time counting," *Journal of Radioanalytical and Nuclear Chemistry*, vol. 248, no. 2, pp. 309–313, 2001. 11, 69

[24] T. Sampson, "Plutonium Isotopic Composition by Gamma-Ray Spectroscopy," *Passive Nondestructive Assay of Nuclear Materials (PANDA)*, pp. 221–272, 1991. [Online]. Available: http://www.lanl.gov/orgs/n/n1/panda/ 11

[25] H. a. Smith, "The Measurement of Uranium Enrichment," *Nureg/Cr-5550*, vol. 195, pp. 195–220, 1991. 11

[26] T. R. England and B. F. Rider, "Evaluation and Compliation of Fission Product Yields," Los Alamos National Laboratory, Tech. Rep., 1994. 12

[27] Knolls Atomic Power Laboratory, *Nuclides and Isotopes: Chart of the Nuclides*, 16th ed. Lockheed Martin, 2002. 19

[28] A. Simonits, F. De Corte, and J. Hoste, "Single-comparator methods in reactor neutron activation analysis," *Journal of Radioanalytical Chemistry*, vol. 24, no. 1, pp. 31–46, 1975. 19

[29] M. Blaauw, "The Holistic Analysis of Gamma-Ray Spectra in Instrumental Neutron Activation Analysis," Ph.D. dissertation, Delft University of Technology, 1993. 19, 20, 21

[30] D. Şahin, V. Radulović, R. M. Lindstrom, and A. Trkov, "Reevaluation of neutron flux characterization parameters for NIST RT-2 facility," *Journal of Radioanalytical and Nuclear Chemistry*, vol. 300, no. 2, pp. 499–506, 2014. 19

[31] S. M. Bowman, "Scale 6: Comprehensive Nuclear Safety Analysis Code System," *Nuclear Technology*, vol. 174, no. 2, pp. 126–148, 2011. 20

[32] L. R. Greenwood and C. D. Johnson, "User Guide for the STAYSL PNNL Suite of Software Tools," no. February, 2013. 22

[33] Oak Ridge National Laboratory, "Scale : A Comprehensive Modeling and Simulation Suite for Nuclear Safety Analysis and Design," *Ornl/Tm-2005/39*, no. June, 2011. 22

[34] C. Heiles, "Least-Squares and Chi-Square for the Budding Aficionado: Art and Practice," University of California Berkeley, Tech. Rep., 2010. 27, 28

[35] ORTEC, "ICS: Integrated Cryocooling System," AMETEK: Advanced Measurement Technology, Tech. Rep., 2015. 30

[36] Canberra Industries, "Genie 2000 Spectroscopy Software Operations," Tech. Rep., 2006. 30

[37] ——, "Lynx Digital Signal Analyzer User's Manual," Tech. Rep., 2008. 31, 33

[38] Los Alamos National Laboratory, "PeakEasy Home Page," 2016. [Online]. Available: https://peakeasy.lanl.gov/ 32

[39] D. C. Glasgow, I. J. Park, S. M. Hayes, J. S. Shin, J. A. Carter, and J. M. Whitaker, "Fast, Sensitive, and Accurate Fissile Determination for Nuclear Nonproliferation Applications by Neutron Activation Analysis and Delayed Neutron Counting," in *Institute of Nuclear Materials Management Annual Meeting*, Orlando, 2004, pp. 1–10. 44, 62

[40] L. A. Currie, "Detection and quantification limits: Origins and historical overview," *Analytica Chimica Acta*, vol. 391, no. 2, pp. 127–134, 1999. 65

[41] ORNL, "SCALE: A Modular Code System for Performing Standardized Computer Analyses for Licensing Evaluations," vol. 3, no. January, 2009. 79

# Appendix

# Appendix A

# SCALE 238-Group Structure

Adopted from Scale6.1Manual Table M4.2.1 [41]

| Group | Lower Boundary (MeV) | Upper Boundary (MeV) |
|---|---|---|
| 1 | 1.00E-11 | 1.00E-10 |
| 2 | 1.00E-10 | 5.00E-10 |
| 3 | 5.00E-10 | 7.50E-10 |
| 4 | 7.50E-10 | 1.00E-09 |
| 5 | 1.00E-09 | 1.20E-09 |
| 6 | 1.20E-09 | 1.50E-09 |
| 7 | 1.50E-09 | 2.00E-09 |
| 8 | 2.00E-09 | 2.50E-09 |
| 9 | 2.50E-09 | 3.00E-09 |
| 10 | 3.00E-09 | 4.00E-09 |
| 11 | 4.00E-09 | 5.00E-09 |
| 12 | 5.00E-09 | 7.50E-09 |
| 13 | 7.50E-09 | 1.00E-08 |
| 14 | 1.00E-08 | 2.53E-08 |
| 15 | 2.53E-08 | 3.00E-08 |
| 16 | 3.00E-08 | 4.00E-08 |
| 17 | 4.00E-08 | 5.00E-08 |
| 18 | 5.00E-08 | 6.00E-08 |
| 19 | 6.00E-08 | 7.00E-08 |
| 20 | 7.00E-08 | 8.00E-08 |
| 21 | 8.00E-08 | 9.00E-08 |
| 22 | 9.00E-08 | 1.00E-07 |
| 23 | 1.00E-07 | 1.25E-07 |

| Group | Lower Boundary (MeV) | Upper Boundary (MeV) |
|---|---|---|
| 24 | 1.25E-07 | 1.50E-07 |
| 25 | 1.50E-07 | 1.75E-07 |
| 26 | 1.75E-07 | 2.00E-07 |
| 27 | 2.00E-07 | 2.25E-07 |
| 28 | 2.25E-07 | 2.50E-07 |
| 29 | 2.50E-07 | 2.75E-07 |
| 30 | 2.75E-07 | 3.00E-07 |
| 31 | 3.00E-07 | 3.25E-07 |
| 32 | 3.25E-07 | 3.50E-07 |
| 33 | 3.50E-07 | 3.75E-07 |
| 34 | 3.75E-07 | 4.00E-07 |
| 35 | 4.00E-07 | 4.50E-07 |
| 36 | 4.50E-07 | 5.00E-07 |
| 37 | 5.00E-07 | 5.50E-07 |
| 38 | 5.50E-07 | 6.00E-07 |
| 39 | 6.00E-07 | 6.25E-07 |
| 40 | 6.25E-07 | 6.50E-07 |
| 41 | 6.50E-07 | 7.00E-07 |
| 42 | 7.00E-07 | 7.50E-07 |
| 43 | 7.50E-07 | 8.00E-07 |
| 44 | 8.00E-07 | 8.50E-07 |
| 45 | 8.50E-07 | 9.00E-07 |
| 46 | 9.00E-07 | 9.25E-07 |
| 47 | 9.25E-07 | 9.50E-07 |
| 48 | 9.50E-07 | 9.75E-07 |
| 49 | 9.75E-07 | 1.00E-06 |
| 50 | 1.00E-06 | 1.01E-06 |
| 51 | 1.01E-06 | 1.02E-06 |
| 52 | 1.02E-06 | 1.03E-06 |
| 53 | 1.03E-06 | 1.04E-06 |
| 54 | 1.04E-06 | 1.05E-06 |
| 55 | 1.05E-06 | 1.06E-06 |
| 56 | 1.06E-06 | 1.07E-06 |
| 57 | 1.07E-06 | 1.08E-06 |
| 58 | 1.08E-06 | 1.09E-06 |
| 59 | 1.09E-06 | 1.10E-06 |
| 60 | 1.10E-06 | 1.11E-06 |
| 61 | 1.11E-06 | 1.12E-06 |
| 62 | 1.12E-06 | 1.13E-06 |

| Group | Lower Boundary (MeV) | Upper Boundary (MeV) |
|---|---|---|
| 63 | 1.13E-06 | 1.14E-06 |
| 64 | 1.14E-06 | 1.15E-06 |
| 65 | 1.15E-06 | 1.18E-06 |
| 66 | 1.18E-06 | 1.20E-06 |
| 67 | 1.20E-06 | 1.23E-06 |
| 68 | 1.23E-06 | 1.25E-06 |
| 69 | 1.25E-06 | 1.30E-06 |
| 70 | 1.30E-06 | 1.35E-06 |
| 71 | 1.35E-06 | 1.40E-06 |
| 72 | 1.40E-06 | 1.45E-06 |
| 73 | 1.45E-06 | 1.50E-06 |
| 74 | 1.50E-06 | 1.59E-06 |
| 75 | 1.59E-06 | 1.68E-06 |
| 76 | 1.68E-06 | 1.77E-06 |
| 77 | 1.77E-06 | 1.86E-06 |
| 78 | 1.86E-06 | 1.94E-06 |
| 79 | 1.94E-06 | 2.00E-06 |
| 80 | 2.00E-06 | 2.12E-06 |
| 81 | 2.12E-06 | 2.21E-06 |
| 82 | 2.21E-06 | 2.30E-06 |
| 83 | 2.30E-06 | 2.38E-06 |
| 84 | 2.38E-06 | 2.47E-06 |
| 85 | 2.47E-06 | 2.57E-06 |
| 86 | 2.57E-06 | 2.67E-06 |
| 87 | 2.67E-06 | 2.77E-06 |
| 88 | 2.77E-06 | 2.87E-06 |
| 89 | 2.87E-06 | 2.97E-06 |
| 90 | 2.97E-06 | 3.00E-06 |
| 91 | 3.00E-06 | 3.05E-06 |
| 92 | 3.05E-06 | 3.15E-06 |
| 93 | 3.15E-06 | 3.50E-06 |
| 94 | 3.50E-06 | 3.73E-06 |
| 95 | 3.73E-06 | 4.00E-06 |
| 96 | 4.00E-06 | 4.75E-06 |
| 97 | 4.75E-06 | 5.00E-06 |
| 98 | 5.00E-06 | 5.40E-06 |
| 99 | 5.40E-06 | 6.00E-06 |
| 100 | 6.00E-06 | 6.25E-06 |
| 101 | 6.25E-06 | 6.50E-06 |

| Group | Lower Boundary (MeV) | Upper Boundary (MeV) |
|---|---|---|
| 102 | 6.50E-06 | 6.75E-06 |
| 103 | 6.75E-06 | 7.00E-06 |
| 104 | 7.00E-06 | 7.15E-06 |
| 105 | 7.15E-06 | 8.10E-06 |
| 106 | 8.10E-06 | 9.10E-06 |
| 107 | 9.10E-06 | 1.00E-05 |
| 108 | 1.00E-05 | 1.15E-05 |
| 109 | 1.15E-05 | 1.19E-05 |
| 110 | 1.19E-05 | 1.29E-05 |
| 111 | 1.29E-05 | 1.38E-05 |
| 112 | 1.38E-05 | 1.44E-05 |
| 113 | 1.44E-05 | 1.51E-05 |
| 114 | 1.51E-05 | 1.60E-05 |
| 115 | 1.60E-05 | 1.70E-05 |
| 116 | 1.70E-05 | 1.85E-05 |
| 117 | 1.85E-05 | 1.90E-05 |
| 118 | 1.90E-05 | 2.00E-05 |
| 119 | 2.00E-05 | 2.10E-05 |
| 120 | 2.10E-05 | 2.25E-05 |
| 121 | 2.25E-05 | 2.50E-05 |
| 122 | 2.50E-05 | 2.75E-05 |
| 123 | 2.75E-05 | 3.00E-05 |
| 124 | 3.00E-05 | 3.13E-05 |
| 125 | 3.13E-05 | 3.18E-05 |
| 126 | 3.18E-05 | 3.33E-05 |
| 127 | 3.33E-05 | 3.38E-05 |
| 128 | 3.38E-05 | 3.46E-05 |
| 129 | 3.46E-05 | 3.55E-05 |
| 130 | 3.55E-05 | 3.70E-05 |
| 131 | 3.70E-05 | 3.80E-05 |
| 132 | 3.80E-05 | 3.91E-05 |
| 133 | 3.91E-05 | 3.96E-05 |
| 134 | 3.96E-05 | 4.10E-05 |
| 135 | 4.10E-05 | 4.24E-05 |
| 136 | 4.24E-05 | 4.40E-05 |
| 137 | 4.40E-05 | 4.52E-05 |
| 138 | 4.52E-05 | 4.70E-05 |
| 139 | 4.70E-05 | 4.83E-05 |
| 140 | 4.83E-05 | 4.92E-05 |

| Group | Lower Boundary (MeV) | Upper Boundary (MeV) |
|---|---|---|
| 141 | 4.92E-05 | 5.06E-05 |
| 142 | 5.06E-05 | 5.20E-05 |
| 143 | 5.20E-05 | 5.34E-05 |
| 144 | 5.34E-05 | 5.90E-05 |
| 145 | 5.90E-05 | 6.10E-05 |
| 146 | 6.10E-05 | 6.50E-05 |
| 147 | 6.50E-05 | 6.75E-05 |
| 148 | 6.75E-05 | 7.20E-05 |
| 149 | 7.20E-05 | 7.60E-05 |
| 150 | 7.60E-05 | 8.00E-05 |
| 151 | 8.00E-05 | 8.20E-05 |
| 152 | 8.20E-05 | 9.00E-05 |
| 153 | 9.00E-05 | 1.00E-04 |
| 154 | 1.00E-04 | 1.08E-04 |
| 155 | 1.08E-04 | 1.15E-04 |
| 156 | 1.15E-04 | 1.19E-04 |
| 157 | 1.19E-04 | 1.22E-04 |
| 158 | 1.22E-04 | 1.86E-04 |
| 159 | 1.86E-04 | 1.93E-04 |
| 160 | 1.93E-04 | 2.08E-04 |
| 161 | 2.08E-04 | 2.10E-04 |
| 162 | 2.10E-04 | 2.40E-04 |
| 163 | 2.40E-04 | 2.85E-04 |
| 164 | 2.85E-04 | 3.05E-04 |
| 165 | 3.05E-04 | 5.50E-04 |
| 166 | 5.50E-04 | 6.70E-04 |
| 167 | 6.70E-04 | 6.83E-04 |
| 168 | 6.83E-04 | 9.50E-04 |
| 169 | 9.50E-04 | 1.15E-03 |
| 170 | 1.15E-03 | 1.50E-03 |
| 171 | 1.50E-03 | 1.55E-03 |
| 172 | 1.55E-03 | 1.80E-03 |
| 173 | 1.80E-03 | 2.20E-03 |
| 174 | 2.20E-03 | 2.29E-03 |
| 175 | 2.29E-03 | 2.58E-03 |
| 176 | 2.58E-03 | 3.00E-03 |
| 177 | 3.00E-03 | 3.74E-03 |
| 178 | 3.74E-03 | 3.90E-03 |
| 179 | 3.90E-03 | 6.00E-03 |

| Group | Lower Boundary (MeV) | Upper Boundary (MeV) |
|---|---|---|
| 180 | 6.00E-03 | 8.03E-03 |
| 181 | 8.03E-03 | 9.50E-03 |
| 182 | 9.50E-03 | 1.30E-02 |
| 183 | 1.30E-02 | 1.70E-02 |
| 184 | 1.70E-02 | 2.50E-02 |
| 185 | 2.50E-02 | 3.00E-02 |
| 186 | 3.00E-02 | 4.50E-02 |
| 187 | 4.50E-02 | 5.00E-02 |
| 188 | 5.00E-02 | 5.20E-02 |
| 189 | 5.20E-02 | 6.00E-02 |
| 190 | 6.00E-02 | 7.30E-02 |
| 191 | 7.30E-02 | 7.50E-02 |
| 192 | 7.50E-02 | 8.20E-02 |
| 193 | 8.20E-02 | 8.50E-02 |
| 194 | 8.50E-02 | 1.00E-01 |
| 195 | 1.00E-01 | 1.28E-01 |
| 196 | 1.28E-01 | 1.50E-01 |
| 197 | 1.50E-01 | 2.00E-01 |
| 198 | 2.00E-01 | 2.70E-01 |
| 199 | 2.70E-01 | 3.30E-01 |
| 200 | 3.30E-01 | 4.00E-01 |
| 201 | 4.00E-01 | 4.20E-01 |
| 202 | 4.20E-01 | 4.40E-01 |
| 203 | 4.40E-01 | 4.70E-01 |
| 204 | 4.70E-01 | 5.00E-01 |
| 205 | 5.00E-01 | 5.50E-01 |
| 206 | 5.50E-01 | 5.73E-01 |
| 207 | 5.73E-01 | 6.00E-01 |
| 208 | 6.00E-01 | 6.70E-01 |
| 209 | 6.70E-01 | 6.79E-01 |
| 210 | 6.79E-01 | 7.50E-01 |
| 211 | 7.50E-01 | 8.20E-01 |
| 212 | 8.20E-01 | 8.61E-01 |
| 213 | 8.61E-01 | 8.75E-01 |
| 214 | 8.75E-01 | 9.00E-01 |
| 215 | 9.00E-01 | 9.20E-01 |
| 216 | 9.20E-01 | 1.01E+00 |
| 217 | 1.01E+00 | 1.10E+00 |
| 218 | 1.10E+00 | 1.20E+00 |

| Group | Lower Boundary (MeV) | Upper Boundary (MeV) |
|---|---|---|
| 219 | 1.20E+00 | 1.25E+00 |
| 220 | 1.25E+00 | 1.32E+00 |
| 221 | 1.32E+00 | 1.36E+00 |
| 222 | 1.36E+00 | 1.40E+00 |
| 223 | 1.40E+00 | 1.50E+00 |
| 224 | 1.50E+00 | 1.85E+00 |
| 225 | 1.85E+00 | 2.35E+00 |
| 226 | 2.35E+00 | 2.48E+00 |
| 227 | 2.48E+00 | 3.00E+00 |
| 228 | 3.00E+00 | 4.30E+00 |
| 229 | 4.30E+00 | 4.80E+00 |
| 230 | 4.80E+00 | 6.43E+00 |
| 231 | 6.43E+00 | 8.19E+00 |
| 232 | 8.19E+00 | 1.00E+01 |
| 233 | 1.00E+01 | 1.28E+01 |
| 234 | 1.28E+01 | 1.38E+01 |
| 235 | 1.38E+01 | 1.46E+01 |
| 236 | 1.46E+01 | 1.57E+01 |
| 237 | 1.57E+01 | 1.73E+01 |
| 238 | 1.73E+01 | 2.00E+01 |

# Appendix B

# Flux Characterizations

Group Structure from Appendix A

Neutron Flux Measured in $(n/cm^2s)$

| Group | PT-2 STAYSL-PNNL Input | PT-2 STAYSL-PNNL Output | PT-1 |
|---|---|---|---|
| 1 | 3.473E+09 | 2.600E+10 | 4.126E+10 |
| 2 | 4.457E+09 | 1.000E+10 | 5.342E+10 |
| 3 | 8.298E+09 | 1.300E+10 | 1.476E+11 |
| 4 | 1.004E+10 | 1.000E+10 | 1.288E+11 |
| 5 | 1.539E+10 | 1.900E+10 | 2.130E+11 |
| 6 | 2.767E+10 | 4.500E+10 | 3.213E+11 |
| 7 | 3.687E+10 | 4.600E+10 | 4.297E+11 |
| 8 | 5.683E+10 | 5.700E+10 | 7.234E+11 |
| 9 | 1.191E+11 | 1.900E+11 | 1.692E+12 |
| 10 | 1.747E+11 | 2.160E+11 | 1.895E+12 |
| 11 | 4.209E+11 | 9.210E+11 | 6.671E+12 |
| 12 | 7.397E+11 | 1.154E+12 | 8.550E+12 |
| 13 | 4.112E+12 | 1.346E+13 | 7.771E+13 |
| 14 | 4.973E+12 | 4.455E+12 | 2.691E+13 |
| 15 | 3.895E+12 | 5.798E+12 | 5.656E+13 |
| 16 | 4.926E+12 | 5.762E+12 | 5.053E+13 |
| 17 | 4.217E+12 | 4.132E+12 | 4.296E+13 |
| 18 | 3.436E+12 | 2.892E+12 | 3.506E+13 |
| 19 | 2.739E+12 | 2.016E+12 | 2.804E+13 |
| 20 | 2.159E+12 | 1.410E+12 | 2.199E+13 |
| 21 | 1.674E+12 | 9.818E+11 | 1.737E+13 |

| Group | PT-2 STAYSL-PNNL Input | PT-2 STAYSL-PNNL Output | PT-1 |
|---|---|---|---|
| 22 | 1.587E+12 | 1.953E+12 | 2.757E+13 |
| 23 | 1.265E+12 | 1.281E+12 | 1.464E+13 |
| 24 | 6.036E+11 | 5.195E+11 | 7.783E+12 |
| 25 | 2.919E+11 | 2.182E+11 | 4.492E+12 |
| 26 | 1.470E+11 | 9.690E+10 | 2.908E+12 |
| 27 | 7.073E+10 | 4.180E+10 | 2.203E+12 |
| 28 | 4.691E+10 | 2.510E+10 | 1.681E+12 |
| 29 | 3.955E+10 | 1.930E+10 | 1.510E+12 |
| 30 | 3.565E+10 | 1.600E+10 | 1.275E+12 |
| 31 | 2.886E+10 | 1.200E+10 | 1.104E+12 |
| 32 | 2.061E+10 | 7.900E+09 | 1.026E+12 |
| 33 | 2.053E+10 | 7.500E+09 | 9.092E+11 |
| 34 | 2.393E+10 | 1.590E+10 | 1.742E+12 |
| 35 | 2.025E+10 | 1.210E+10 | 1.550E+12 |
| 36 | 1.879E+10 | 1.030E+10 | 1.420E+12 |
| 37 | 1.859E+10 | 9.400E+09 | 1.262E+12 |
| 38 | 1.846E+10 | 4.400E+09 | 5.957E+11 |
| 39 | 1.727E+10 | 3.800E+09 | 5.369E+11 |
| 40 | 1.576E+10 | 6.900E+09 | 1.041E+12 |
| 41 | 1.272E+10 | 5.100E+09 | 9.546E+11 |
| 42 | 1.088E+10 | 4.000E+09 | 8.518E+11 |
| 43 | 1.088E+10 | 3.800E+09 | 8.334E+11 |
| 44 | 1.049E+10 | 3.500E+09 | 8.242E+11 |
| 45 | 1.000E+10 | 1.600E+09 | 3.547E+11 |
| 46 | 1.000E+10 | 1.500E+09 | 3.343E+11 |
| 47 | 1.000E+10 | 1.500E+09 | 3.594E+11 |
| 48 | 1.000E+10 | 1.400E+09 | 3.062E+11 |
| 49 | 1.000E+10 | 6.000E+08 | 1.247E+11 |
| 50 | 1.000E+10 | 5.000E+08 | 1.145E+11 |
| 51 | 1.000E+10 | 6.000E+08 | 1.288E+11 |
| 52 | 1.000E+10 | 5.000E+08 | 1.167E+11 |
| 53 | 1.000E+10 | 6.000E+08 | 1.466E+11 |
| 54 | 1.000E+10 | 5.000E+08 | 1.350E+11 |
| 55 | 1.000E+10 | 5.000E+08 | 1.329E+11 |
| 56 | 1.000E+10 | 5.000E+08 | 1.297E+11 |
| 57 | 1.000E+10 | 6.000E+08 | 1.307E+11 |
| 58 | 1.000E+10 | 5.000E+08 | 1.394E+11 |
| 59 | 1.000E+10 | 5.000E+08 | 1.461E+11 |
| 60 | 1.000E+10 | 5.000E+08 | 1.241E+11 |

| Group | PT-2 STAYSL-PNNL Input | PT-2 STAYSL-PNNL Output | PT-1 |
|---|---|---|---|
| 61 | 1.000E+10 | 5.000E+08 | 1.048E+11 |
| 62 | 1.000E+10 | 5.000E+08 | 1.100E+11 |
| 63 | 1.000E+10 | 5.000E+08 | 1.165E+11 |
| 64 | 1.000E+10 | 1.200E+09 | 2.794E+11 |
| 65 | 1.000E+10 | 1.200E+09 | 2.771E+11 |
| 66 | 1.000E+10 | 1.200E+09 | 2.629E+11 |
| 67 | 1.000E+10 | 1.100E+09 | 2.703E+11 |
| 68 | 1.000E+10 | 2.300E+09 | 4.733E+11 |
| 69 | 1.000E+10 | 2.100E+09 | 4.595E+11 |
| 70 | 1.000E+10 | 2.100E+09 | 4.816E+11 |
| 71 | 1.000E+10 | 2.000E+09 | 4.373E+11 |
| 72 | 1.000E+10 | 2.000E+09 | 4.289E+11 |
| 73 | 1.000E+10 | 3.400E+09 | 7.202E+11 |
| 74 | 1.000E+10 | 3.200E+09 | 6.975E+11 |
| 75 | 1.000E+10 | 3.000E+09 | 6.453E+11 |
| 76 | 1.000E+10 | 2.900E+09 | 6.411E+11 |
| 77 | 1.000E+10 | 2.400E+09 | 5.129E+11 |
| 78 | 1.000E+10 | 1.700E+09 | 3.335E+11 |
| 79 | 1.000E+10 | 3.400E+09 | 7.097E+11 |
| 80 | 1.000E+10 | 2.400E+09 | 4.838E+11 |
| 81 | 1.000E+10 | 2.300E+09 | 5.230E+11 |
| 82 | 1.000E+10 | 2.000E+09 | 4.253E+11 |
| 83 | 1.000E+10 | 2.100E+09 | 4.475E+11 |
| 84 | 1.000E+10 | 2.300E+09 | 4.945E+11 |
| 85 | 1.000E+10 | 2.200E+09 | 4.646E+11 |
| 86 | 1.000E+10 | 2.100E+09 | 4.231E+11 |
| 87 | 1.000E+10 | 2.000E+09 | 4.360E+11 |
| 88 | 1.000E+10 | 2.000E+09 | 4.070E+11 |
| 89 | 1.000E+10 | 5.000E+08 | 1.454E+11 |
| 90 | 1.000E+10 | 1.000E+09 | 1.971E+11 |
| 91 | 1.000E+10 | 1.800E+09 | 3.959E+11 |
| 92 | 1.000E+10 | 6.300E+09 | 1.301E+12 |
| 93 | 1.000E+10 | 3.800E+09 | 7.633E+11 |
| 94 | 1.000E+10 | 4.200E+09 | 8.249E+11 |
| 95 | 1.000E+10 | 1.670E+10 | 2.091E+12 |
| 96 | 1.000E+10 | 1.167E+10 | 5.882E+11 |
| 97 | 1.000E+10 | 8.030E+09 | 8.885E+11 |
| 98 | 1.000E+10 | 6.690E+09 | 1.221E+12 |
| 99 | 1.000E+10 | 2.350E+09 | 4.718E+11 |

| Group | PT-2 STAYSL-PNNL Input | PT-2 STAYSL-PNNL Output | PT-1 |
|---|---|---|---|
| 100 | 1.000E+10 | 2.240E+09 | 4.757E+11 |
| 101 | 1.000E+10 | 2.160E+09 | 4.191E+11 |
| 102 | 1.000E+10 | 2.070E+09 | 4.215E+11 |
| 103 | 1.000E+10 | 1.200E+09 | 2.622E+11 |
| 104 | 1.000E+10 | 7.310E+09 | 1.374E+12 |
| 105 | 1.000E+10 | 6.760E+09 | 1.320E+12 |
| 106 | 1.000E+10 | 5.440E+09 | 1.132E+12 |
| 107 | 1.000E+10 | 8.120E+09 | 1.479E+12 |
| 108 | 1.000E+10 | 1.940E+09 | 3.879E+11 |
| 109 | 1.000E+10 | 4.610E+09 | 9.107E+11 |
| 110 | 1.000E+10 | 3.640E+09 | 7.059E+11 |
| 111 | 1.000E+10 | 2.620E+09 | 5.546E+11 |
| 112 | 1.000E+10 | 2.690E+09 | 5.076E+11 |
| 113 | 1.000E+10 | 3.290E+09 | 5.931E+11 |
| 114 | 1.000E+10 | 3.450E+09 | 7.031E+11 |
| 115 | 1.000E+10 | 4.820E+09 | 9.270E+11 |
| 116 | 1.000E+10 | 1.500E+09 | 2.994E+11 |
| 117 | 1.000E+10 | 2.910E+09 | 5.543E+11 |
| 118 | 1.000E+10 | 2.760E+09 | 4.496E+11 |
| 119 | 1.000E+10 | 3.920E+09 | 7.652E+11 |
| 120 | 1.000E+10 | 6.030E+09 | 1.137E+12 |
| 121 | 1.000E+10 | 5.410E+09 | 1.021E+12 |
| 122 | 1.000E+10 | 4.930E+09 | 9.444E+11 |
| 123 | 1.000E+10 | 2.300E+09 | 4.100E+11 |
| 124 | 1.000E+10 | 9.000E+08 | 1.673E+11 |
| 125 | 1.000E+10 | 2.610E+09 | 5.576E+11 |
| 126 | 1.000E+10 | 8.400E+08 | 1.772E+11 |
| 127 | 1.000E+10 | 1.400E+09 | 2.925E+11 |
| 128 | 1.000E+10 | 1.450E+09 | 2.620E+11 |
| 129 | 1.000E+10 | 2.330E+09 | 4.786E+11 |
| 130 | 1.000E+10 | 1.510E+09 | 2.733E+11 |
| 131 | 1.000E+10 | 1.610E+09 | 2.917E+11 |
| 132 | 1.000E+10 | 7.100E+08 | 1.330E+11 |
| 133 | 1.000E+10 | 1.960E+09 | 3.684E+11 |
| 134 | 1.000E+10 | 1.900E+09 | 3.492E+11 |
| 135 | 1.000E+10 | 2.090E+09 | 3.727E+11 |
| 136 | 1.000E+10 | 1.510E+09 | 2.912E+11 |
| 137 | 1.000E+10 | 2.210E+09 | 4.432E+11 |
| 138 | 1.000E+10 | 1.540E+09 | 2.935E+11 |

| Group | PT-2 STAYSL-PNNL Input | PT-2 STAYSL-PNNL Output | PT-1 |
|---|---|---|---|
| 139 | 1.000E+10 | 1.040E+09 | 1.976E+11 |
| 140 | 1.000E+10 | 1.580E+09 | 2.850E+11 |
| 141 | 1.000E+10 | 1.540E+09 | 2.616E+11 |
| 142 | 1.000E+10 | 1.500E+09 | 2.635E+11 |
| 143 | 1.000E+10 | 5.650E+09 | 1.030E+12 |
| 144 | 1.000E+10 | 1.980E+09 | 3.535E+11 |
| 145 | 1.000E+10 | 3.610E+09 | 6.333E+11 |
| 146 | 1.000E+10 | 2.130E+09 | 3.643E+11 |
| 147 | 1.000E+10 | 3.660E+09 | 6.925E+11 |
| 148 | 1.000E+10 | 3.070E+09 | 5.857E+11 |
| 149 | 1.000E+10 | 2.950E+09 | 5.296E+11 |
| 150 | 1.000E+10 | 1.400E+09 | 2.115E+11 |
| 151 | 1.000E+10 | 5.260E+09 | 9.936E+11 |
| 152 | 1.000E+10 | 6.090E+09 | 1.071E+12 |
| 153 | 1.000E+10 | 4.530E+09 | 7.428E+11 |
| 154 | 1.000E+10 | 3.730E+09 | 6.708E+11 |
| 155 | 1.000E+10 | 2.030E+09 | 3.612E+11 |
| 156 | 1.000E+10 | 1.410E+09 | 2.382E+11 |
| 157 | 1.000E+10 | 7.804E+10 | 4.131E+12 |
| 158 | 1.000E+10 | 1.940E+09 | 3.186E+11 |
| 159 | 1.000E+10 | 4.240E+09 | 6.875E+11 |
| 160 | 1.000E+10 | 6.800E+08 | 1.145E+11 |
| 161 | 1.000E+10 | 9.070E+09 | 1.240E+12 |
| 162 | 1.000E+10 | 9.800E+09 | 1.697E+12 |
| 163 | 1.000E+10 | 3.850E+09 | 7.748E+11 |
| 164 | 1.000E+10 | 6.378E+10 | 5.333E+12 |
| 165 | 1.000E+10 | 1.119E+10 | 1.852E+12 |
| 166 | 1.000E+10 | 1.080E+09 | 1.756E+11 |
| 167 | 1.000E+10 | 1.867E+10 | 3.057E+12 |
| 168 | 1.000E+10 | 1.078E+10 | 1.717E+12 |
| 169 | 1.000E+10 | 1.496E+10 | 2.340E+12 |
| 170 | 1.000E+10 | 1.840E+09 | 2.948E+11 |
| 171 | 1.000E+10 | 8.410E+09 | 1.366E+12 |
| 172 | 1.000E+10 | 1.128E+10 | 1.926E+12 |
| 173 | 1.000E+10 | 2.250E+09 | 3.604E+11 |
| 174 | 1.000E+10 | 6.690E+09 | 1.048E+12 |
| 175 | 1.000E+10 | 8.480E+09 | 1.320E+12 |
| 176 | 1.000E+10 | 1.237E+10 | 1.892E+12 |
| 177 | 1.000E+10 | 2.350E+09 | 3.730E+11 |

| Group | PT-2 STAYSL-PNNL Input | PT-2 STAYSL-PNNL Output | PT-1 |
|---|---|---|---|
| 178 | 1.000E+10 | 2.410E+10 | 3.566E+12 |
| 179 | 1.000E+10 | 1.679E+10 | 2.372E+12 |
| 180 | 1.000E+10 | 9.470E+09 | 1.278E+12 |
| 181 | 1.000E+10 | 1.903E+10 | 2.512E+12 |
| 182 | 1.000E+10 | 1.501E+10 | 2.184E+12 |
| 183 | 1.000E+10 | 2.154E+10 | 3.140E+12 |
| 184 | 1.000E+10 | 1.026E+10 | 1.477E+12 |
| 185 | 1.000E+10 | 2.271E+10 | 3.159E+12 |
| 186 | 1.000E+10 | 5.930E+09 | 9.251E+11 |
| 187 | 1.000E+10 | 2.200E+09 | 3.356E+11 |
| 188 | 1.000E+10 | 8.030E+09 | 1.231E+12 |
| 189 | 1.000E+10 | 1.101E+10 | 1.795E+12 |
| 190 | 1.000E+10 | 1.520E+09 | 2.215E+11 |
| 191 | 1.000E+10 | 5.010E+09 | 8.806E+11 |
| 192 | 1.000E+10 | 2.010E+09 | 2.975E+11 |
| 193 | 1.000E+10 | 9.140E+09 | 1.443E+12 |
| 194 | 1.000E+10 | 1.396E+10 | 2.428E+12 |
| 195 | 1.000E+10 | 8.780E+09 | 1.536E+12 |
| 196 | 1.000E+10 | 1.608E+10 | 3.003E+12 |
| 197 | 1.000E+10 | 1.677E+10 | 3.415E+12 |
| 198 | 1.000E+10 | 1.124E+10 | 2.605E+12 |
| 199 | 1.000E+10 | 1.078E+10 | 2.475E+12 |
| 200 | 1.000E+10 | 2.740E+09 | 6.009E+11 |
| 201 | 1.000E+10 | 2.610E+09 | 4.554E+11 |
| 202 | 1.000E+10 | 3.700E+09 | 7.896E+11 |
| 203 | 1.000E+10 | 3.410E+09 | 7.653E+11 |
| 204 | 1.000E+10 | 5.410E+09 | 1.232E+12 |
| 205 | 1.000E+10 | 2.300E+09 | 4.605E+11 |
| 206 | 1.000E+10 | 2.580E+09 | 5.066E+11 |
| 207 | 1.000E+10 | 6.190E+09 | 1.034E+12 |
| 208 | 1.000E+10 | 7.500E+08 | 1.695E+11 |
| 209 | 1.000E+10 | 5.580E+09 | 1.301E+12 |
| 210 | 1.000E+10 | 5.010E+09 | 1.205E+12 |
| 211 | 1.000E+10 | 2.740E+09 | 5.642E+11 |
| 212 | 1.000E+10 | 9.000E+08 | 2.210E+11 |
| 213 | 1.000E+10 | 1.580E+09 | 3.753E+11 |
| 214 | 1.000E+10 | 1.240E+09 | 2.518E+11 |
| 215 | 1.000E+10 | 5.240E+09 | 1.156E+12 |
| 216 | 1.000E+10 | 4.790E+09 | 9.664E+11 |

| Group | PT-2 STAYSL-PNNL Input | PT-2 STAYSL-PNNL Output | PT-1 |
|---|---|---|---|
| 217 | 1.000E+10 | 4.900E+09 | 1.177E+12 |
| 218 | 1.000E+10 | 2.290E+09 | 5.073E+11 |
| 219 | 1.000E+10 | 2.940E+09 | 7.843E+11 |
| 220 | 1.000E+10 | 1.640E+09 | 4.225E+11 |
| 221 | 1.000E+10 | 1.790E+09 | 4.187E+11 |
| 222 | 1.000E+10 | 3.900E+09 | 1.032E+12 |
| 223 | 1.000E+10 | 1.213E+10 | 3.063E+12 |
| 224 | 1.000E+10 | 1.511E+10 | 2.349E+12 |
| 225 | 1.000E+10 | 3.030E+09 | 3.384E+11 |
| 226 | 1.000E+10 | 1.348E+10 | 7.775E+11 |
| 227 | 1.000E+10 | 3.777E+10 | 1.416E+12 |
| 228 | 1.000E+10 | 7.902E+09 | 3.760E+11 |
| 229 | 1.000E+10 | 2.768E+10 | 6.686E+11 |
| 230 | 1.000E+10 | 1.457E+10 | 2.151E+11 |
| 231 | 1.000E+10 | 9.526E+09 | 4.199E+11 |
| 232 | 1.000E+10 | 7.242E+09 | 4.345E+11 |
| 233 | 1.000E+10 | 3.414E+09 | 3.565E+11 |
| 234 | 1.000E+10 | 2.446E+09 | 4.036E+11 |
| 235 | 1.000E+10 | 3.428E+09 | 3.982E+11 |
| 236 | 1.000E+10 | 4.484E+09 | 3.861E+11 |
| 237 | 1.000E+10 | 6.545E+09 | 3.960E+11 |
| 238 | 1.000E+10 | 1.265E+08 | 3.581E+09 |

# Vita

Justin Richard Knowles was born in 1990 to Charles and Julie Knowles in Boise, Idaho. He has two younger siblings, Logan and Sierra. Justin attended Capital High School and the Treasure Valley Mathematics and Science Center magnet school in Boise. He graduated high school in 2009 and moved to West Lafayette, Indiana where he attended Purdue University and earned his Bachelor of Science in Nuclear Engineering. While attending Purdue, Justin was very active in the American Nuclear Society and was president of the university's student section in his Junior year. During his undergraduate summers, Justin interned at the Idaho National Laboratory in several different areas, including the Advanced Test Reactor, Materials and Fuels Complex, and the National and Homeland Security Division. After graduating from Purdue in 2013, Justin accepted a fellowship from the Bredesen Center for Interdisciplinary Research and Graduate Education at the University of Tennessee to study Energy Science and Engineering. The fellowship provided Justin the opportunity to conduct research at the Oak Ridge National Laboratory while earning his PhD. Justin's doctoral research focused on analyzing short-lived fission products for nuclear forensics and safeguards measurements at the High Flux Isotope Reactor Neutron Activation Analysis Laboratory. While pursuing his PhD, Justin remained active in the American Nuclear Society and was awarded their Distinguished Service Award for demonstrating, through a detailed analysis, the mismanagement of crediting nuclear energy in the Environmental Protection Agency's initial draft of the Clean Power Plan. Justin completed his PhD in 2016 and intends to pursue a career

focused on nuclear modeling, safeguards, and forensics. He has recently accepted a job as a postdoctoral research associate at Oak Ridge National Laboratory.